

Growing tissues: A simulation study

Inaugural-Dissertation

zur

Erlangung des Doktorgrades

der Mathematisch-Naturwissenschaftlichen Fakultät

der Universität zu Köln

vorgelegt von

Nils Podewitz

aus *Buchholz in der Nordheide*

Jülich

2015

Berichterstatter: Prof. Dr. Gerhard Gompper
(Gutachter) Prof. Dr. Johannes Berg

Tag der mündlichen Prüfung: 20. April 2015

Dedicated to my parents Kersten & Regina Podewitz

Zusammenfassung

Zelluläre Gewebe repräsentieren einen interessanten Materialtyp: aktive Materie. Der Grundbaustein eines jeden Gewebes, Zellen, teilen sich und sterben, konsumieren und dissipieren Energie und üben Kräfte auf ihre Umgebung aus. Damit stellen sie ein Nichtgleichgewichtssystem dar. Wachsende Gewebe sind Bestandteil vieler biologischer Prozesse. Das Verständnis der grundlegenden Phänomene wachsender Gewebe ist somit nicht nur von einem physikalischen Standpunkt aus interessant.

In dieser Dissertation beschäftigen wir uns mit der Mechanik wachsender Gewebe im Kontext der Theorie des homeostatischen Drucks. Der homeostatische Druck ist definiert als der Druck, der auf ein Gewebe, das in einer biochemisch konstanten Umgebung wächst, ausgeübt werden muss, um ein Gleichgewicht zwischen Zellteilungen und Zelltod zu erhalten. Experimentelle Beobachtungen zeigen jedoch, dass Gewebewachstum von Oberflächeneffekten dominiert ist. Eine erhöhte Zellteilungsrate an der Oberfläche kann dabei einen im Mittel absterbenden Kern ausgleichen. Somit ist der homeostatische Druck als Größe stets weit entfernt von Oberflächen zu verstehen. Wir studieren Wachstum mit einem *negativen* homeostatischen Druck. Das heißt ohne Oberflächeneffekte ist eine mechanische Spannung notwendig, um einen stabilen stationären Zustand zu gewährleisten. Wir verwenden eine mesoskopische, teilchenbasierte Simulationstechnik, in der Zellen durch zwei Punktteilchen dargestellt werden. Diese wechselwirken wie weiche klebrige Kugeln. Eine abstoßende Kraft zwischen den beiden Teilchen einer Zelle modelliert das Wachstum. Beim Überschreiten eines kritischen Abstandes werden zwei neue Teilchen eingefügt. Der aktive Teil wird von dissipative particle dynamics ähnlichen Wechselwirkungen und einer konstanten Zelltodrate komplettiert.

Mit diesem Ansatz untersuchen wir die Abhängigkeit des homeostatischen Drucks von verschiedenen Modellparametern. Des Weiteren messen wir die Wachstumsraten im Inneren von Gewebespheroiden unter mechanischem Stress und vergleichen die Ergebnisse mit *in vitro* Experimenten von Gewebespheroiden unter Druck. Eine Anpassung der Simulationen an die experimentellen Daten resultiert in einer Abschätzung für den homeostatischen

Druck dieser Zelllinie von -1 bis -2 kPa. Des Weiteren zeigen wir einen neuen Gewebezustand: Membranen unter Spannung. Gewebe mit einem negativen homeostatischen Druck bilden dabei eine dünne Schicht, die unter einer charakteristischen Spannung steht. Diese Spannung wird durch Zellteilungen an der Oberfläche und Zelltod im Inneren aufrechterhalten.

Ferner studieren wir die Grenzflächendynamik von zwei konkurrierenden Geweben mit einem unterschiedlichen homeostatischen Druck. Diese Differenz verursacht im Kontext der Theorie des homeostatischen Drucks die Übernahme des Gewebes mit dem höheren homeostatischen Druck. Ausgehend von einem theoretischen Standpunkt lösen wir die Dynamik des eindimensionalen Problems für den Spezialfall von verschwindender Diffusion. Diese Lösung beschreibt eine sich mit konstanter Geschwindigkeit bewegende Grenzfläche. Wir verwenden das gleiche Simulationsmodell wie zuvor, um die Grenzflächendynamik in zwei Dimensionen zu studieren und mit der analytischen Lösung zu vergleichen. Die Abhängigkeit der Grenzflächengeschwindigkeit von der Differenz der homeostatischen Drücke der beiden Gewebe, sowie die erhaltenen Vorhersagen für das Stressprofil stimmen sehr gut mit den Simulationen überein. Des Weiteren untersuchen wir das Skalenverhalten der Grenzflächenbreite w , welche zu Beginn durch $w \sim t^\beta$ beschrieben werden kann und für späte Zeiten t abhängig von der Systembreite L saturiert $w_{sat} \sim L^\alpha$. Wir erhalten einen Wachstumsexponenten $\beta \approx 0.4$ und einen Rauigkeitsexponenten $\alpha \approx 0.25$. Während der Wachstumsexponent ungefähr in die Kardar–Parisi–Zhang Universalitätsklasse passt, ist der gemessene Rauigkeitsexponent deutlich kleiner.

Abschließend beschäftigen wir uns mit der Ausrichtung der Teilungsachsen in expandierenden einlagigen Zellschichten. Wir erweitern dazu die Simulationen um einen bereits etablierten Motilitätsmechanismus und vergleichen die Ergebnisse mit experimentellen Daten von Madin–Darby canine kidney Zellschichten, die in schmale Mikrokanäle eindringen. Die Analyse der experimentellen Daten ergibt eine starke Korrelation zwischen Divisionsachse und Flussrichtung. Die stärkste Korrelation weist die Divisionsachse jedoch mit der Hauptachse des Verformungsgeschwindigkeitstensors auf, welche mit der Hauptrichtung des lokalen Stresses zusammenhängt. Dies unterstützt die These, dass Zelldivisionen nicht von der lokalen Geschwindigkeit, sondern vom lokalen Stress ausgerichtet werden. Abgesehen von Effekten in der Nähe von Grenzflächen und einem unerwarteten Fluss von Zellen senkrecht zur Hauptmigrationsrichtung reproduzieren die Simulationen die beobachteten Größen erstaunlich gut.

Abstract

Tissues represent an interesting type of matter: active matter. The basic elements of tissues, the cells, divide or die, consume energy on the scale of their constituents, exert forces onto their surrounding and dissipate energy, which results in non-equilibrium systems. Tissue growth is involved in many biological processes and understanding its generic phenomena is, thus, not only important from a physical point of view.

In this thesis, we are interested in the mechanics of tissue growth in the context of the homeostatic pressure theory. The homeostatic pressure is defined as the pressure that has to be exerted onto a tissue, growing in a biochemically constant environment, in order to balance cell division and cell death. However, experimental observations show that tissue growth is dominated by surface effects in the sense that high division rates at the surface can compensate for an on average dying core. Thus, the homeostatic pressure is better defined as a bulk property. We study the growth with a *negative* homeostatic pressure, which means that without the surface growth effect such a tissue has to be kept under tension to ensure a stable steady state. A mesoscale simulation technique is used, where individual cells are represented by two point particles, interacting like soft sticky spheres. Growth is modeled by a force that repels the particles of one cell until new particles are introduced, when the cell reaches a certain size. Additionally, dissipative particle dynamics like interactions and a constant rate of cell death concludes the active part.

This approach is used to explore the dependence of the homeostatic pressure on different model parameters. Additionally, we measure the bulk growth rates of tissue spheroids under different mechanical stresses and compare our results to the data of in vitro experiments of tissue spheroids under pressure. We fit the simulations to this experimental data and extract a homeostatic pressure of the order of -1 to -2 kPa. Furthermore, we find a new tissue state: a tensile membrane. In this state, the tissue forms a relatively thin sheet, where a characteristic tension develops for tissues with a negative homeostatic pressure. It is sustained by growth at the surface and death in the bulk.

In addition, we study the interface dynamics of two competing tissues with a homeostatic

pressure difference. In the theory of homeostatic pressure, this difference leads to a take-over of the tissue with the higher homeostatic pressure. Starting from a theoretical point of view, we solve the dynamics for the one dimensional problem without diffusion and find the interface to propagate at a constant velocity. We use the same simulation technique as above to study the interface dynamics in two dimensions and compare our results to the analytical solution. The dependence of the interface velocity on the homeostatic pressure difference between the tissues as well as the predicted stress profiles match well with the simulations. Furthermore, we analyze the scaling behavior of the interface width w , which develops initially as a power law $w \sim t^\beta$ and saturates depending on the system size L for later times $w_{sat} \sim L^\alpha$. We find a growth exponent $\beta \approx 0.4$ and a roughness exponent $\alpha \approx 0.25$. While the growth exponent roughly fits into the Kardar–Parisi–Zhang universality class, the measured roughness exponent is substantially smaller.

At last, we study divisional alignment in expanding monolayered cell sheets. We extend the simulations with a previously established motility mechanism and compare the results to the experimental data of Madin-Darby canine kidney cell sheets that invade narrow microchannels. In the experiments, we find a strong correlation between the division orientation and the emergent flow. However, cell division correlates best with the main axis of the strain rate tensor, which is related to the main axis of the stress tensor. This supports the notion that divisions are aligned by the local stress as opposed to the local velocity. Apart from boundary phenomena and a surprising flow of cells perpendicular to the main migration direction, the simulations are able to reproduce the experimentally observed quantities very well.

Contents

1	Introduction and state of the art	1
1.1	From condensed matter physics to tissue growth	1
1.2	Cancer	2
1.3	Mechanics in tissue growth	3
1.4	Continuum mechanics of tissues	6
1.4.1	Tissue growth, homeostatic pressure and competition	6
1.4.2	Non-uniform growth	9
1.5	Discrete tissue models	12
2	Theory and methods	17
2.1	Simulations	17
2.1.1	Model	17
2.1.2	Modelling monolayered tissues	20
2.1.3	Solving the equations of motion	22
2.1.4	Performance	24
2.1.5	Boundary conditions	26
2.1.6	Reduced units	27
2.1.7	Constant pressure ensemble	28
2.1.8	Gas particle method	29
2.1.9	Stress measurements	29
2.1.10	Density	31
2.1.11	Cell division	32
2.1.12	Tissue competition set-up	32
2.2	Theory	35
2.2.1	Tissue growth of spheroids	35
2.2.2	Characterizing flow in tissue spheroids	37
2.2.3	Simple tissue competition	38

2.2.4	Quantifying order	40
2.2.5	Interfacial tension	42
2.2.6	Velocity gradient, strain rate and stress tensor	42
3	Results	47
3.1	Negative homeostatic pressure	47
3.1.1	Homeostatic pressure dependence on model parameters	47
3.1.2	Spheroids	52
3.1.3	Bulk growth rate dependence on pressure	54
3.1.4	Negative homeostatic pressure in real tissues	56
3.1.5	Tensile membranes	61
3.2	Interface dynamics of competing tissues	67
3.2.1	Tissue competition without diffusion in 1d	67
3.2.2	Interface position and width	72
3.2.3	Interface properties in theory and simulations	75
3.2.4	Interface tension	78
3.2.5	Scaling behavior	80
3.3	Division axes alignment in motile tissues	83
3.3.1	Experimental and simulation Set-ups	83
3.3.2	Rescaling simulations	84
3.3.3	Resting cell sheets	86
3.3.4	Invading cell sheets	92
3.3.5	Cell division orientation dependence on local properties	95
3.3.6	Stress measurements in simulations	98
3.3.7	Parameter variation	99
4	Conclusions	101
4.1	Negative homeostatic pressure	101
4.2	Interface dynamics of competing tissues	104
4.3	Division axes alignment in motile tissues	105
	Bibliography	107
	List of Figures	121

List of Tables 125

Acknowledgments 127

Appendix 129

Erklärung der Selbstständigkeit 131

Lebenslauf 132

Nomenclature

α	roughness exponent
\bar{S}^b	residual bulk order
β	growth exponent
χ^2	sum of squared residuals
δk_s	surface growth rate increment
Δt	integration time step
$\Delta\sigma$	homeostatic stress difference
γ_s	surface/interface tension
γ_{bg}	background friction coefficient
\hat{l}	length rescaling factor
\hat{P}	pressure rescaling factor
\hat{t}	time rescaling factor
κ	growth rate coefficient
λ	thickness of surface growth region
φ	cell number fraction
ρ	density
ρ_b	bulk density
σ_H	homeostatic stress
$\sigma_{\alpha\beta}$	stress tensor
\mathbf{d}	cell division axis
\mathbf{F}	force

\mathbf{f}	force density
\mathbf{r}_i	position of particle i
\mathbf{v}_i	velocity of particle i
λ	main axis of the strain rate tensor
B	growth force strength
B_c	critical growth force strength
$E_{\alpha\beta}$	strain rate tensor
f_0	repulsive cell-cell potential coefficient
f_1	adhesion strength
f_c	critical adhesion strength
K	compressibility
k	growth rate
k_a	apoptosis (death) rate
k_b	bulk growth rate
k_d	division rate
L	system size
m	motility force strength
N	number of cells
P	pressure
p	dipole strength
P^i	imposed pressure
P_H/P_H^b	homeostatic pressure/bulk homeostatic pressure
r	radial distance
R_{ss}	steady state radius
s	distance to surface/front/interface
S_a^b	order parameter between \mathbf{a} and \mathbf{b}
t	time

V	volume
v_0	interface velocity
v_f	front velocity
w	interface width
w_{sat}	saturation interface width
$x/y/z$	Cartesian distance

List of abbreviations

MD	molecular dynamics
DPD	dissipative particle dynamics
PBC	periodic boundary condition
BBC	bounce-back boundary condition
RBC	reflective boundary condition
SD	standard deviation
SEM	standard error of mean
KPZ	Kardar–Parisi–Zhang
MBE	molecular beam epitaxy
MDCK	Madin-Darby canine kidney
PEG-DMA	poly(ethylene glycol)-dimethacrylate
PDMS	polydimethylsiloxane
PIV	particle image velocimetry

1 Introduction and state of the art

1.1 From condensed matter physics to tissue growth

The study of matter in general and material properties in particular is as old as mankind itself. With the advent of modern science great progress has been made. Nowadays, many macroscopic material properties can be understood and explained on an atomistic level. This is the field of condensed matter. In many cases the interactions holding the microscopic constituents together are very strong as, for example, in crystals. Other materials, however, exhibit weaker or *soft* interactions, i.e. on the order of the thermal energy. In this *soft matter* fluctuations and entropy play an important role. From gels in food like yogurt, gelatin or pudding to complex liquids like milk or blood, soft matter systems are ubiquitous to daily life. Classical subfields of soft matter include membranes, polymer solutions, colloidal solutions, foams, gels, granular materials and liquid crystals.

Cellular tissues are also characterized as soft materials. Contrary to ordinary materials, however, tissues constantly consume energy on the scale of their constituents. Cells die, divide, migrate and contract, thus, converting chemical fuels to stresses and material growth. They are, hence, considered a part of *active matter*. However, tissues are not just active in the sense of creating stresses internally but they are also *self generating*. Divisions constantly produce new material that, in turn, can replicate again, while cell death in this sense destroys material. It is this peculiarity of self generation and destruction that renders the physics of tissues so interesting from a material science point of view. Furthermore, understanding the physics of tissues and their properties is important for many biological processes like morphogenesis (the development of the shape of an organism), wound-healing or diseases.

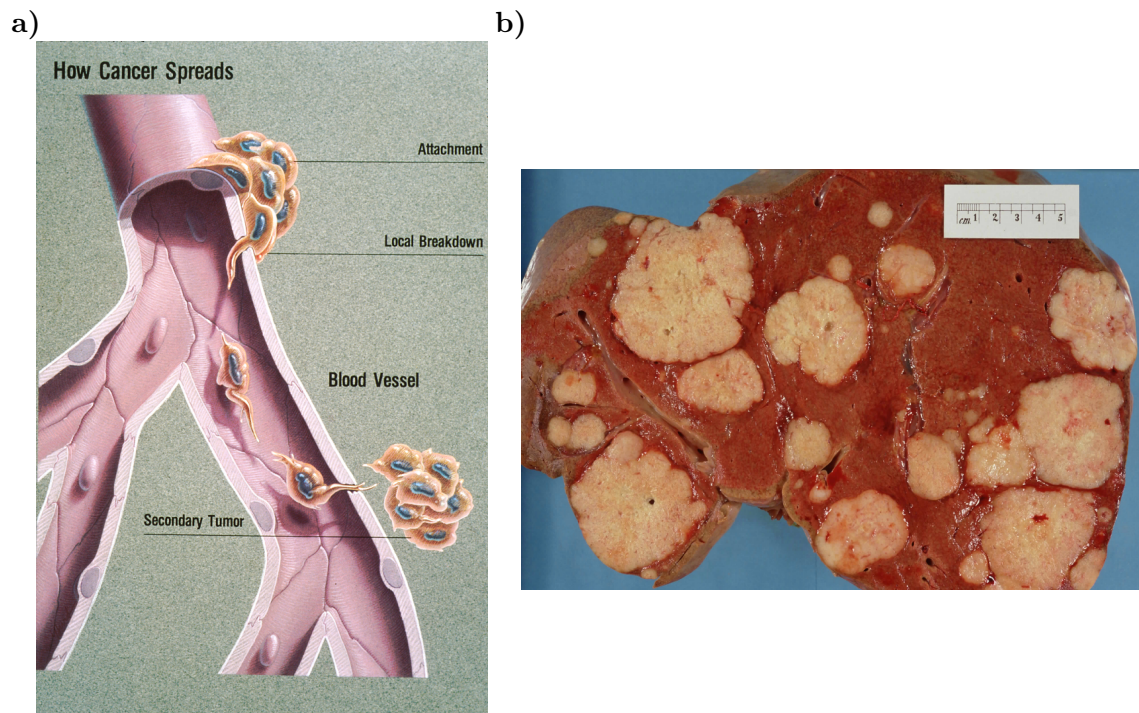


Figure 1.1: Tumors and metastatic spreading. a) “How cancer spreads” by Jane Hurd (Illustrator) [Public domain], via Wikimedia Commons [Hurd, 2015]. Primary tumor invades blood vessel and releases single malignant cells into the blood stream. These can penetrate into the healthy tissue and give rise to a second tumor at another site. b) “Cross section of a human liver, taken at autopsy examination, showing multiple large pale tumor deposits. The tumor is an adenocarcinoma derived from a primary lesion in the body of the pancreas.” By Haymanj [Public domain], via Wikimedia Commons [Haymanj, 2015].

1.2 Cancer

One of the most devastating diseases haunting modern civilization is known as cancer. With an estimated 14.1 million new cases and 8.2 million deaths in the year 2012 alone [IAR, 2014] it is found among the top ten causes of death worldwide. The predictions even suggest an increase in new cancer cases to 23.6 million people in the year 2030 [Bray et al., 2012]. Thus, a deeper knowledge and understanding of the development of cancer would greatly benefit all of mankind.

Since the beginning of cancer research, a vast amount of different causes have been discovered. Ranging from virus infections [Rous, 1910, 1911, Shope, 1933], over environ-

mental or physical influences [Findlay, 1928, Muller, 1928] to chemicals [Kennaway & Hieger, 1930, Yamagiwa & Ichikawa, 1918], all of these causes result in an aberrant cell behavior that disrupts the carefully orchestrated interplay of a multicellular organism. For such an organism it is vitally important to regulate the growth and death of its cells. Many different mechanisms are known that initiate or inhibit cell division or trigger apoptosis (programmed cell death). Cancer cells, however, lack the ability to properly respond to such signals and instead proliferate uncontrollably [Preston-Martin et al., 1990]. Thus, even a single mutated cell can give rise to a macroscopic tumor that, due to its increasing volume, pushes aside the healthy tissue around its position. A single tumor, though, is rarely deadly. Most of the cancer related deaths are caused by organ failure due to the metastatic spreading of the primary tumor [Weinberg, 2007]. This process occurs when the tumor is able to penetrate into the blood vessels of the host body. Single cells can detach, travel to distant locations, and form new tumors called metastases (see figure 1.1). Therefore, it seems obvious that a deeper understanding of tissue growth in general and the competition between different tissues in particular is of interest for cancer research.

1.3 Mechanics in tissue growth

From a physics point of view, a tumor has to deform its surrounding in order to grow. Such a deformation, in turn, results in a force exerted back onto the growing tumor. Thus, the question arise whether mechanical stresses, or mechanics in general, affect tissue growth.

Already in 1981, it was suggested that mechanical stresses could regulate and guide tissue growth [Ingber et al., 1981], inspired by an analysis of rat liver carcinomas (a type of cancer). A correlation was found between the attachment of those cells to a basal membrane and their organization, thus, linking a mechanical stimulus (the attachment to the basal membrane) to the tissue organization.

Since then, a lot of different examples have been found, where mechanics directly influence tissue growth. For example, a direct correlation has been discovered between stress and proliferation patterns [Nelson et al., 2005]. Using microfabrication techniques, small structures were created on which cell sheets were grown. Depending on the stress patterns created by the cells, different proliferation patterns emerged, where cell division is enhanced in regions of high tension. Furthermore, it has been shown that a variation in the cell-cell adhesion leads to a change in stress gradient, which in turn modifies the cell proliferation rate. Such a mechanical feedback could be used to stabilize and regulate

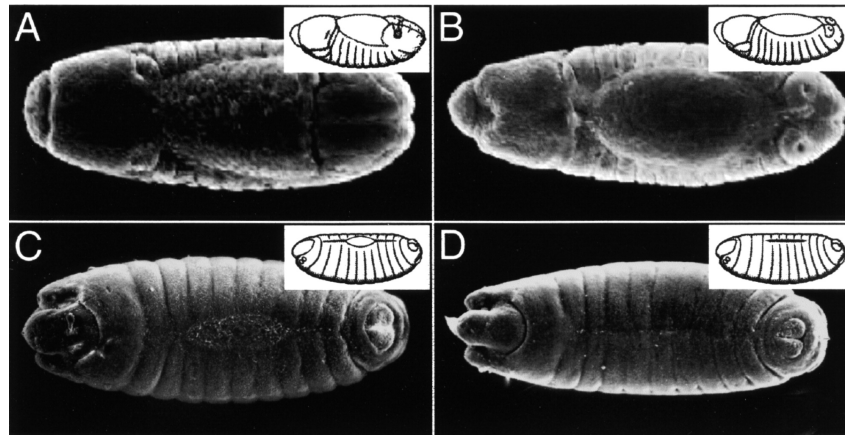


Figure 1.2: Dorsal closure in *Drosophila*. Illustration of the four stages of dorsal closure in *Drosophila* larvae. Pictures represent electron micrographs, while a lateral view icon resides at the top right of each picture. Note the contraction of the amnioserosa that is the central part in the electron micrographs. Taken from [Jacinto et al., 2002].

tissue growth. For example, during the development of *Drosophila* wing discs uniform growth is observed despite the present gradients in growth factors and the stochastic nature of cell divisions [Milán et al., 1996]. According to Shraiman [2005], this could be explained as follows. Consider a small patch of tissue, where one cell is growing slower than the rest. Since the surrounding is expanding, tension is built up, which enhances cell growth locally. If, on the other hand, a cell is growing faster than its surrounding, the compressional stress reduces cell growth, thus, stabilizing a uniform growth rate.

A direct impact of mechanical stresses on the morphogenesis (that is the development of the shape of an organism) was observed, for example, during the dorsal closure of *Drosophila* larvae [Kiehart et al., 2000]. Dorsal closure refers to a step in the larvae development, where an eye-shaped gap in the epithelium (that is a protective layer of cells differentiating inside from outside) on the back side of the fruit fly embryo is sealed (see figure 1.2). The cells inside the gap, called amnioserosa, constrict apically (i.e. at the top), which generates a force, driving the epithelial sheets together until the gap is closed. Apical constriction has been shown to drive other morphogenetic processes as well, like gastrulation, a fundamental step in embryo development, or the formation of the neural tube, a precursor to the central nervous system [Sawyer et al., 2010].

Another example of how mechanics can be involved in tissue growth is the villification

of the gut. Its surface consists of many small finger-like protrusions, called villi. Although the reason for their existence is not finally ascertained, one intuitive explanation would be the maximization of absorptive area. The formation of these villi (villification) can be understood mechanically [Hannezo et al., 2011, Shyer et al., 2013]. If a cell sheet is attached to an elastic substrate and starts to grow, the resulting compressive stresses trigger a buckling instability that leads to a structure formation similar to the aforementioned villi.

In all the above examples the mechanics were dominated by the forces due to tissue growth. However, other forces can contribute as well, for example motility forces. Many cells either have the ability to perform directed motions or can transform into a different type to gain this ability. One such transformation is called epithelial-mesenchymal transition (EMT). Epithelial cells constitute one of the four basic animal tissue types and line the cavities and surfaces of many structures in the body. During the EMT, they lower their cell-cell adhesion and lose their polarity due to the loss of contact to the basal membrane. Polarity, in this context, refers to the basal-apical orientation, where the cell differs in structure and composition at the basal membrane as compared to the opposite (apical) position. After the EMT, they become mesenchymal-like cells with migratory and invasive properties. This transition was observed in many developmental processes but also in wound-healing [Kalluri & Weinberg, 2009] and in tumor progression [Thiery, 2002].

Since most cells, especially epithelia, retain a constant mechanical contact to their neighbors through junctions (see e.g. [Alberts, 2008]), they do not move independently of each other. Instead, complex collective phenomena are observed in migrating cell sheets. For example, large scale, swirl-like flow patterns were found at low densities and a large reduction in motility with increasing cell density, resembling a glass-like arrest [Angelini et al., 2010, 2011]. Furthermore, finger-like protrusions were discovered in migrating cell sheets, stemming from border instabilities of initially flat interfaces [Poujade et al., 2007]. In order to better understand the processes involved in migration, several experimental techniques have been proposed to measure the spatio-temporal evolution of traction forces. For example, fluorescent particles were embedded in a polyacrylamide gel [Dembo & Wang, 1999]. Another method utilized micropillar arrays made of polydimethylsiloxane (PDMS) [du Roure et al., 2005]. Both methods derive the forces from the displacement of the underlying substrate. However, the first explicit map of the physical forces during migration was measured by Trepap et al. [2009]. They found expanding cell sheets to be under a global state of *tension* with increasing modulus in the bulk. Such a state cannot arise from directed cell motion only at the border, contrary to wide belief [Gov, 2007, Poujade

et al., 2007, Vaughan & Trinkaus, 1966]. Instead, all cells have to pull on average towards the boundary, even several hundred cell diameters away from it. It is highly unlikely that chemical signals sent by the cells at the border diffuse fast enough to the inner cells, to cause such large scale correlations. Thus, a simple flocking-type mechanism was suggested [Basan et al., 2013] that offers an explanation for the experimentally observed long range alignment of motility forces. In the proposed mechanism cells tend to align their motility forces with the direction of their velocity. It was able to reproduce the global state of tension, the swirl-like flow patterns, the large reduction in motility with increasing cell density and the finger-like protrusions due to border instabilities.

1.4 Continuum mechanics of tissues

Now, the question arises how tissue development can be described from a physical point of view. As already mentioned at the beginning, tissues represent a type of matter that is different from classical solids or liquids: they are active. Classical laws for continuum mechanics like elasticity [Landau & Lifshitz, 1986] or hydrodynamics [Landau & Lifshitz, 1987] can be extended to account for the active processes. One way to introduce growth into continuum mechanics is the addition of a source term to the continuity equation

$$\partial_t \rho + \nabla \cdot (\rho \mathbf{v}) = k \rho. \quad (1.1)$$

Here, \mathbf{v} is the velocity profile, ρ the cell density, and $k = k_d - k_a$ the effective growth rate i.e. the difference in division rate k_d and apoptosis rate k_a .

Such an approach has been successful to model the growth of tissue spheroids [Byrne & Chaplain, 1995]. Concentration fields of nutrients and growth inhibitors were added, which coupled the growth rate in equation (1.1) to the local concentrations of these quantities. By applying this approach to the growth of tumors, it has been shown how stable solutions corresponding to a non-zero tumor size depend on the nutrient consumption and growth inhibitor concentration.

1.4.1 Tissue growth, homeostatic pressure and competition

Rather recently, Basan et al. [2009] proposed a new idea of tissue competition driven by *homeostatic pressure*. The concept is best described by the following simple *gedankenexperiment*. Consider a tissue inside a box as depicted in figure 1.3. The walls are permeable

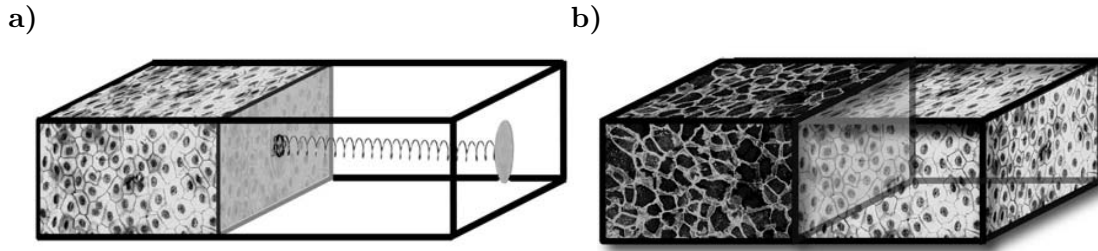


Figure 1.3: Sketch of tissue growth in a confined volume. **a)** Tissue on the left is confined by the movable piston that is connected to a spring and thus exerts a defined pressure onto the system. **b)** Same as in **a)** but instead of a spring a second tissue is put into the right chamber, which is then competing against the tissue on the left for volume. Taken from [Basan et al., 2009].

to nutrients, growth factors, and everything else a tissue needs to proliferate to ensure a constant biochemical state. Instead of an incompressible box, one wall is replaced by a movable piston connected to a spring. The cells are dividing with a rate k_d and dying with a rate $k_a < k_d$, thus, filling the compartment. Once the box is filled by the tissue, it starts to press against the piston, which then exerts a certain pressure back onto the tissue. With increasing pressure, the death (or apoptosis) rate goes up, while the division rate goes down until a steady state with $k_d = k_a$ is reached. This steady state is stable since any perturbation drives the system back to its steady or *homeostatic* state. The pressure and density in this state are constant (although different) for each tissue and, thus, called *homeostatic pressure* P_H and *homeostatic density* ρ_H . They are fundamental material properties of tissues. Around the homeostatic state, the growth rate k can be expanded in terms of the pressure difference $P_H - P$ between an external pressure P and the homeostatic pressure P_H of the tissue

$$k = \kappa(P_H - P) + \mathcal{O}[(P_H - P)^2]. \quad (1.2)$$

or in terms of the difference between the homeostatic density ρ_H and the actual density ρ

$$k = \chi(\rho_H - \rho) + \mathcal{O}[(\rho_H - \rho)^2]. \quad (1.3)$$

For small differences $P_H - P$ (or $\rho_H - \rho$), the higher order terms can be neglected, resulting in a linear approximation. This linear approximation has been successfully used to couple

growth rates to the mechanics in the analytical description of tissue competition.

Consider now the same gedankenexperiment with a second tissue instead of a spring (see figure 1.3). Both tissues grow until they have filled their half of the box. Let us assume that tissue A has a homeostatic pressure P_H^A and B a higher homeostatic pressure $P_H^B > P_H^A$. Since the wall separating the tissues is movable, the different pressures inside the box are equalized. This, on the other hand, means that a pressure is exerted onto tissue A that is higher than its homeostatic pressure. In the context of the homeostatic pressure theory, the growth rate of tissue A is shifted to an on average apoptotic rate, thus, leading to the recession of A, while B takes over the compartment. Interestingly, the winner of such a competition is determined solely by their homeostatic pressures and is independent of the actual division rates. In the extreme case of the competition between a fast and a slow growing tissue, the slow growing tissue would still win as long as it has the higher homeostatic pressure.

Recently, a continuum description of tissue competition that accounts for cell flow fields and stress distributions on large scales has been developed [Ranft et al., 2014]. Assuming incompressible tissues, the cell fraction φ of A-type cells follows a generalized Fisher-Kolmogorov equation

$$\partial_t \varphi + \mathbf{v} \cdot \nabla \varphi = D \nabla^2 \varphi + \varphi(1 - \varphi)(k^A - k^B), \quad (1.4)$$

where \mathbf{v} is the velocity field, D is the diffusion coefficient and $k^{A/B}$ are the stress dependent growth rates of the two tissues. Again, the coupling of the stress to the growth rates was achieved through the linear expansion around the homeostatic state. This yields traveling wave solutions similar to those of the original Fisher-Kolmogorov equation. In the later case, however, traveling waves can only propagate with a diffusion constant $D > 0$. Therefore, one could expect that neglecting diffusion ($D = 0$) does not result in a moving interface.

Another interesting aspect of tissue competition concerns the form and development of the interface between the two tissues. It can be considered as a growing surface and, thus, the standard methods of surface growth physics can be applied (see e.g. [Barabási & Stanley, 1995]). One of its major tools is the classification of the scaling behavior. Let us consider a growing surface of width $w(L, t)$ that is a function of the system size L and the time t . Its typical time evolution separates into two regions: an initial power law increase

with time

$$w(L, t) \sim t^\beta \tag{1.5}$$

and a saturation regime with a width $w_{sat}(L)$ that depends on L

$$w_{sat}(L) \sim L^\alpha. \tag{1.6}$$

The exponent β is called *growth exponent*, while α is called *roughness exponent*. These two exponents are commonly used to classify the growth process. An experimental study of in vitro and in vivo cell line and tumor growth [Brú et al., 2003] showed scaling exponents consistent with the molecular beam epitaxy (MBE) universality class ($\alpha_{MBE}^{2d} = 3/2$, $\beta_{MBE}^{2d} = 3/8$). However, a numerical study [Block et al., 2007] of the mechanism that was proposed to cause the MBE-like scaling resulted in exponents that describe a Kardar–Parisi–Zhang (KPZ)-like scaling ($\alpha_{KPZ}^{2d} = 1/2$, $\beta_{KPZ}^{2d} = 1/3$). For growing bacterial colonies another roughness exponent was suggested of $\alpha = 0.78$ [Vicsek et al., 1990] that falls into neither of the two above classes.

1.4.2 Non-uniform growth

The homeostatic pressure gedankenexperiment assumed a spatial and temporal uniform growth rate k , which would result in exponential growth for unconfined tissues. However, experiments of tissue spheroids grown at constant biochemical conditions [Montel et al., 2011] have revealed a differing, non-exponential behavior (see figure 1.4a). A closer analysis showed that cell divisions do not occur uniformly over the spheroid but are favored near the surface (see figure 1.4b). This *surface growth effect* is even enhanced if a pressure is applied, hinting for a mechanical explanation as opposed to other causes, like limited nutrient availability. An intuitive, purely mechanistic explanation could be as follows. In order for a cell to grow, it has to enlarge its volume, thus, creating a strain dipole. The energy required to insert such a strain dipole in the bulk of the material should be higher than near the surface, where part of the necessary strain field is cut away.

To describe the experimental findings, a simple two rate growth model was proposed

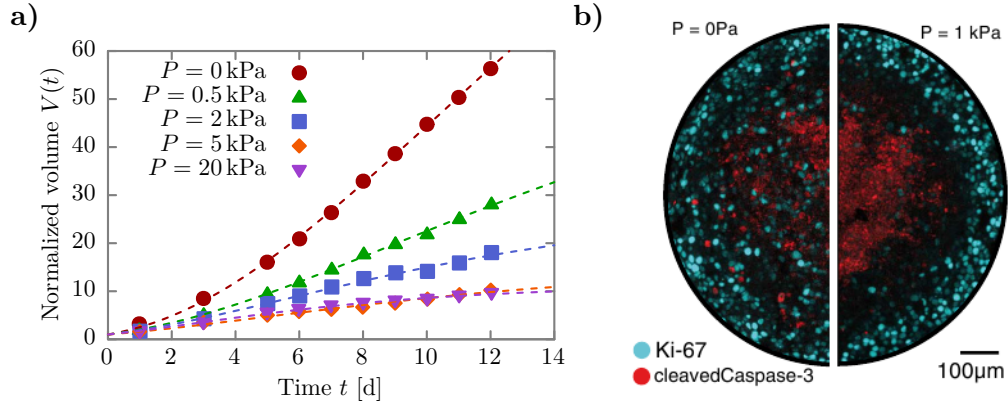


Figure 1.4: Growth of tissue spheroids under pressure. a) Experimental data of the normalized volume V of a tissue spheroid over time t for different external pressures. Dashed lines represent fits of equation (1.10). Note that the initial exponential growth is succeeded by a linear regime. Redrawn from [Montel et al., 2011]. b) Cryosections of tissue spheroids with and without external pressure. “Cryosections and immunofluorescence of the spheroids are used to label the cell divisions [antibody against Ki-67 in cyan] and apoptosis [antibody against cleaved Caspase-3 in red]. (Left) Half section of a spheroid grown in a normal medium for 4 d. (Right) Half section of a spheroid grown with a stress of 1 kPa for 4 d.” Taken from [Montel et al., 2011].

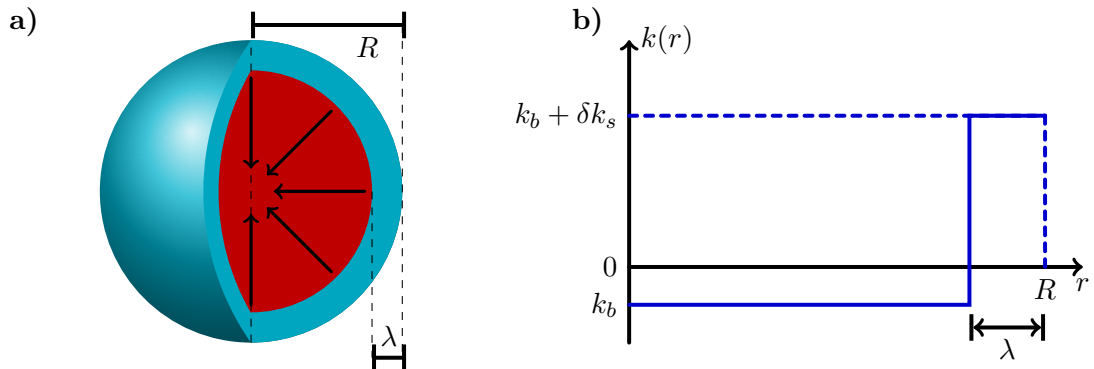


Figure 1.5: Sketch of the two rate growth model. a) Sketch of a tissue spheroid of size R . The red region shows the apoptotic core, while the proliferating rim is colored in cyan. Black arrows denote the radial flow of cells from the surface to the core. b) Growth rate k as a function of radial distance r for the two rate growth model.

(see figure 1.5)

$$k(r) = \begin{cases} k_b & \text{for } r \leq R - \lambda \\ k_b + \delta k_s & \text{for } r > R - \lambda \end{cases} \quad (1.7)$$

with a bulk growth rate k_b and a surface growth increment δk_s in a small region of thickness λ for a tissue spheroid of size R [Montel et al., 2011]. The change in volume $\partial_t V(t)$ for such a system with a constant density ρ reads

$$\partial_t V(t) = \int_V k(\mathbf{r}) \, d\mathbf{r} \quad (1.8)$$

and results in

$$\partial_t V(t) = k_b V + (36\pi)^{1/3} V^{2/3}. \quad (1.9)$$

This differential equation is solved for $V \geq 0$ by

$$V(t) = \left[\left(1 + \frac{(36\pi)^{1/3} \delta k_s \lambda}{k_b} \right) \exp\left(\frac{k_b}{3} t\right) - \frac{(36\pi)^{1/3} \delta k_s \lambda}{k_b} \right]^3 \quad (1.10)$$

with $V(0) = 1$. A fit of this equation to experimental data revealed a good agreement as shown in [Montel et al., 2011] and figure 1.4b and allows the extraction of k_b and δk_s .

A stable steady state solution of equation (1.9) requires $k_b < 0$ and $k_b + \delta k_s > 0$, referring to surface growth and bulk death. This has been observed experimentally in several different cell lines [Delarue et al., 2013, 2014]. In order to maintain its integrity, the apoptotic core in such a spheroid has to be balanced by a flux of cells from the proliferating surface. This flux has recently been measured in experiments of growing tissue spheroids [Delarue et al., 2013]. Fluorescently labeled core-shell nanoparticles were incorporated into the outermost layer of cells of growing tissue spheroids and their distribution over time was followed. The measured flows were consistent with the analytical calculations for the two-rate growth model.

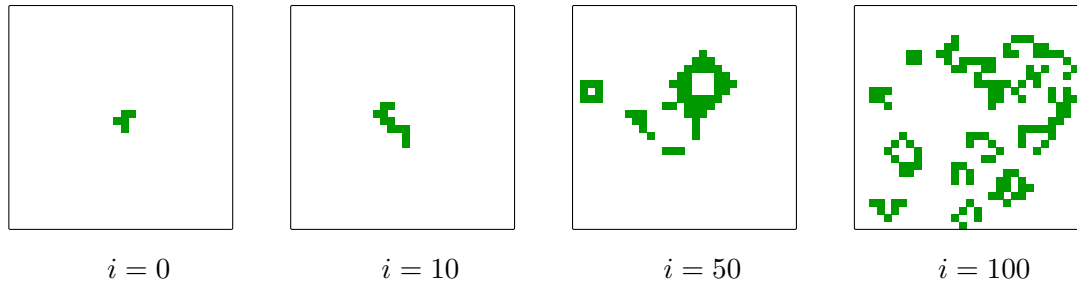


Figure 1.6: Conway's game of life. Evolution of a simple initial configuration. The number of iterations i is written below each snapshot. Note the complex patterns emerging after several iterations.

1.5 Discrete tissue models

A large amount of discrete, cell-based models have been proposed. In general, they can be divided into two main categories, lattice and off-lattice models. Lattice-based models are, for example, those of cellular automata. A cellular automaton consists of a regular grid of cells that can be in a number of different states. A set of rules govern the interactions between neighboring cells and thus determine the dynamics. Probably the most famous example of a cellular automaton is Conway's Game of Life [Gardner, 1970]. Each grid point therein can either contain a living cell or be empty and only three simple rules governing death, birth and survival of each cell. A cell is born, when an empty field has exactly three neighbors. A living cell dies of over- or underpopulation when it has more than three or less than two neighbors and survives if it has exactly two or three neighbors. These simple rules already gives rise to complex dynamic patterns (see figure 1.6). Although this model was not intend to study tissue growth, a similar approach has been successfully used to study blood vessel networks [Peirce et al., 2004]. Starting with an initial in vivo blood vessel network, their cellular automaton was able to predict the emergent patterning responses to external stimuli that is mechanical stress and the delivery of growth factors.

Cellular automata have also been used in hybrid approaches, for example to model early tumor growth and invasion [Patel et al., 2001]. In this model, each automaton element corresponds to a volume element of the size of one cell and is occupied by either a normal cell, a tumor cell, a micro-vessel or empty. Two important components are added, nutrients (glucose) and hydrogen ions. The later is observed to be produced by tumor cells, which alters the microenvironment and is harmful to the healthy tissue. The

production, however, can be compensated by a vascular network (small blood vessels) that transports the ions away. Modeling the concentration fields of glucose and hydrogen ions by diffusion-reaction partial differential equations, thus, combining the discrete and continuum approaches, they were able to show that already small excess hydrogen ion production of tumor cells lead to a sufficient alteration of the microenvironment to promote tumor invasion. Furthermore, an optimal vascular density was found for each hydrogen ion production excess that significantly reduces tumor growth.

Apart from studying such detailed biological processes, cellular automata have also been utilized to understand basic phenomena in tissue growth. Starting from an irregular lattice, each grid point can contain at most one cell. Each cell is able to migrate and divide. Division can, however, only occur if a free lattice site is available within a certain radius. Then, all cells along the line that connects the mother cell with the nearest free grid point are shifted so that the two daughter cells reside next to each other [Block et al., 2007, Radszuweit et al., 2009]. This model was used to determine the universality class of growing colonies.

Originating from the field of computational fluid dynamics, Lattice-Boltzmann methods have also been adopted to study tissues. In contrast to the cellular automata described above, this method considers the advection of density distributions on a lattice. Its dynamics are described by a streaming step, where the distributions move according to a discrete velocity, and a collision step, where the interactions are governed. In a way this can be considered as particles moving through time and space and is, thus, different from the examples above. This method has been used to study the time evolution of multicellular systems [Artur et al., 2011] and it has been able to successfully reproduce the fusion process of tissue spheroids.

Abandoning the discretization of space and velocity leads to off-lattice models, where cells are represented by a set of point particles. The simplest case of one point particle per cell was, for example, used by Drasdo et al. [1995]. Defining a radius that changes over time as cell size and introducing new particles to model proliferation, the dynamics were simulated by Monte-Carlo steps. In each step, a cell can randomly perform one of several possible actions, such as migration, growth, rotation, and deformation. Defining ΔE as the change in energy due to the chosen action, the standard Metropolis algorithm always accepts this change for $\Delta E < 0$ and only with a probability $\exp(-\Delta E)$ otherwise. This approach was applicable to model parts of the wound healing process of skin cuts and the growth of sarcoma (a type of tumor deriving from the connective tissue).

Instead of a Monte Carlo-type simulation, it is also possible to integrate Newton's equations of motion to determine the cell movement by defining appropriate interaction potentials. This approach was used to model multicellular tumor spheroids [Schaller & Meyer-Hermann, 2005]. Each cell is represented by a point particle with a set of parameters that include cell position, radius, different states according to the cell cycle, and cell-type specific coupling constants for the elastic and adhesive interactions. The unperturbed cell shape is assumed to be a sphere that deforms due to the interactions with the neighboring cells. The nearest neighbors are determined by a Delaunay triangulation and due to its connection to the Voronoi diagram, the contact area between neighbors can easily be calculated as well. With this model, the nutrient uptake of glucose and oxygen and its connection to necrosis was analyzed. Necrosis refers to the death of a cell due to cell injury, which is nearly always detrimental and has to be differentiated from the programmed cell death called apoptosis. The utilized Delaunay triangulation that determines the nearest neighbors is, however, computationally rather expensive. Defining instead short ranged forces and considering only cell-cell interactions within a certain radius of a cell can be much faster. On the other hand, the forces and their range has to be chosen carefully as next-nearest neighbor interactions can cause problems (see e.g. [Pathmanathan et al., 2009]). Furthermore, the random cell motions have to be included in this approach as compared to Monte Carlo simulations, where they are included by design. This can be achieved by assuming the over-damped limit and solving the Langevin equation [Dallon & Othmer, 2004, Galle et al., 2005].

In order to incorporate a more detailed picture of individual cells, a subcellular element model was proposed [Sandersius & Newman, 2008], where each cell is divided into a number of elastically coupled volume elements. The interactions are governed by a potential with short range repulsion and long range adhesion (with respect to the interaction range), which leads in connection with the assumption of the over-damped limit to a viscoelastic behavior. This model was able to capture the intermediate-frequency rheology of living cells in a semi-quantitative manner.

All these models, however, need the definition of coarse grained interaction potentials. The construction of such potentials, divide into two major approaches. First, one starts with a set of measurable cell characteristics, like cell stiffness, growth rate, Young modulus, Poisson ratio, etc., and model the physical interactions with force fields that take these parameters as input [Hoehme & Drasdo, 2010]. In order to incorporate proliferation, cells double their volume by stochastic increments and subsequently deform into dumbbells until

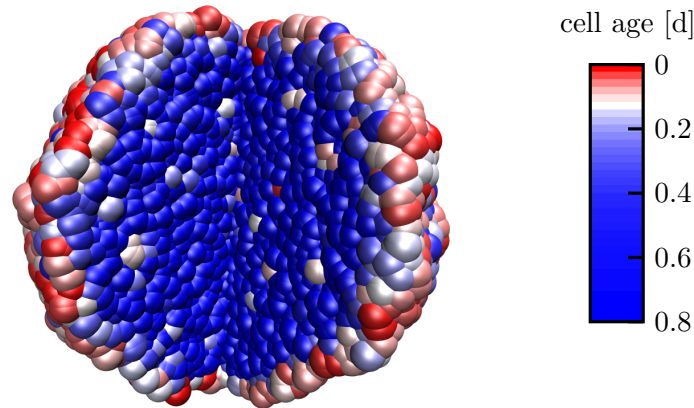


Figure 1.7: Simulation snapshot of a growing tissue spheroid. A quarter section is cut out of the spheroid simulated with the model of [Basan et al. \[2011\]](#). The cells are color coded according to their age. Red corresponds to cells that have recently divided, while blue cells have not divided for a long time. Note the high cell division rate near the surface.

they split into two daughter cells. An extended version of this model led to the discovery of an integral mechanism to the regeneration process of the liver, the hepatocyte-sinosoid alignment (HSA) [[Hoehme et al., 2010](#)]. The liver is a highly structured organ, which does not function properly without its microstructures. It consists mainly of hepatocytes, a special type of cell, which are responsible for protein synthesis, storage, transformation of carbohydrates and detoxification, the main functions of the liver. These cells are connected to small blood vessels, called sinusoids. If a small volume of hepatocytes die due to necrosis, the adjacent healthy hepatocytes start to proliferate and migrate towards the necrotic zone. The aforementioned simulations were used to model this process and the results were compared to the experimental data of a regenerating mouse liver. A thorough analysis revealed that only the inclusion of the alignment of daughter hepatocytes in the direction of the nearest sinusoid into the simulation model could account for all experimental observations. However, the rather large set of parameters in such a model can make it difficult to study generic phenomena.

The other, more minimalistic approach incorporates only a few basic and well known cell-cell interactions. [Basan et al. \[2011\]](#), for example, have modeled cells by simple soft sticky spheres. In order to include proliferation, cells were represented by two point particles that repel each other with a growth force that depends on the particle-particle

distance. Compared to other models, this approach has the advantage that an inherent feedback of stress onto growth is included due to the finite growth force. The emergence of interesting phenomena can, in such a model, be traced back to the initial few assumptions on cell behavior. Even more, switching off specific cell-cell interactions might lead to a deeper understanding of the studied phenomenon. It has been shown with this model that tissues behave like viscoelastic fluids due to cell turnover. Disabling cell death leads to a rheological behavior of a plastic material with a finite yield stress [Ranft et al., 2010]. Furthermore, the feedback of the stress onto growth leads to a surface growth effect similar to the one observed in the experiments mentioned in section 1.4.2 (see figure 1.7).

To summarize, there is not one ultimate cell/tissue model but rather, depending on the phenomena of interest, a different approach might be suited best. In this thesis, we followed the approach of Basan et al. [2011].

2 Theory and methods

2.1 Simulations

2.1.1 Model

The main interest of this work lies in the study of generic aspects of tissue growth on the scale of tissues. As outlined above, there exist a lot of different discrete models. We chose to utilize the same approach as in [Basan et al., 2011, Montel et al., 2011, 2012] since it has already been proven to model tissue growth in the context of the homeostatic pressure theory very well. Furthermore, its minimalistic approach is best suited for the study of generic phenomena, which we are interested in. In this model, each cell is represented by two point particles. It is, however, important to note that a simulation cell is a highly simplified representation of a real cell. Thus, identifying one simulation cell with a real cell is overinterpreting the model. It is, in principle, possible to get a more detailed picture at the cellular level by using more than two particles to represent one cell. This, on the other hand, would require additional constraints, connecting all the particles that build one cell. Furthermore, one could also interpret the two particles in the current model as a small patch of tissue with a preferred growth direction, thus, representing a local average over several real cells.

In this model, the particles of a cell interact via short ranged potentials with each other and other particles within range R_{pp} . The resulting force on particle i

$$\mathbf{F}_i = \underbrace{\mathbf{F}_{ik}^g + \mathbf{F}_{ik}^d + \mathbf{F}_{ik}^r}_{\text{intracellular forces}} + \underbrace{\sum_{j \neq \{i,k\}} (\mathbf{F}_{ij}^v + \mathbf{F}_{ij}^a + \mathbf{F}_{ij}^d + \mathbf{F}_{ij}^r)}_{\text{intercellular forces}} + \mathbf{F}_i^b \quad (2.1)$$

splits up into an intra- and an intercellular part and the background friction \mathbf{F}_i^b . In this context, i and k form a cell, while the sum over j refers to interactions between particles

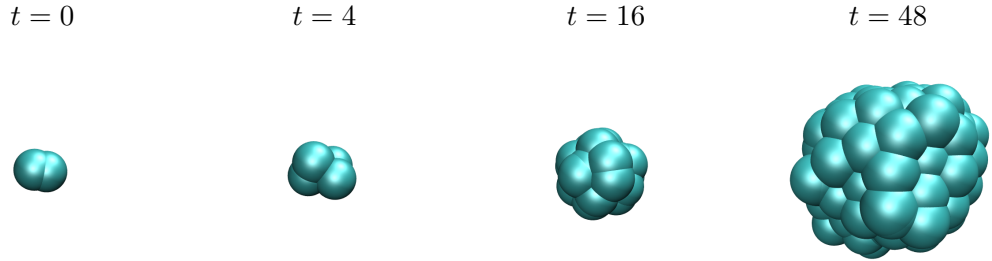


Figure 2.1: Simulation snapshots of a growing spheroid. Note that at $t = 0$ the two shown particles form one cell. Upon division two new particles are introduced so that at $t = 4$ there are two cells. Redrawn from [Ranft et al., 2010].

of different cells. Growth is modeled by the force

$$\mathbf{F}_{ik}^g = \frac{B}{(r_{ik} + r_0)^2} \hat{\mathbf{r}}_{ik}, \quad (2.2)$$

with the distance between the two particles i and j of one cell $r_{ij} = |\mathbf{r}_j - \mathbf{r}_i|$, the cellular expansion pressure constant r_0 , the growth coefficient B and the unit vector $\hat{\mathbf{r}}_{ij} = \mathbf{r}_{ij}/r_{ij}$. The volume exclusion force

$$\mathbf{F}_{ij}^v = f_0 \left(\frac{R_{pp}^5}{r_{ij}^5} - 1 \right) \hat{\mathbf{r}}_{ij} \quad (2.3)$$

ensures impenetrability of the cells, where f_0 is the repulsive cell-cell potential coefficient and R_{pp} the range of pair potentials. The later defines the cut-off for all pair interactions. As cells like to stick to each other, adhesion is represented by a simple constant force

$$\mathbf{F}_{ij}^a = -f_1 \hat{\mathbf{r}}_{ij} \quad (2.4)$$

acting along the connection of i and j with the adhesion strength f_1 .

Cell division and apoptosis

Cell death is implemented as a constant rate k_a at which cells disappear. In order for a cell to divide, it has to reach a certain critical size r_{ct} (i.e. $|\mathbf{r}_i - \mathbf{r}_j| \geq r_{ct}$) upon which two new particles are placed near the existing ones. These four particles then constitute the

two new cells (see figure 2.1).

Energy dissipation and noise

Living cells are subjected to a lot of different fluctuations and are able to dissipate energy. To account for these effects we use a dissipative particle dynamics (DPD) type thermostat, which was originally introduced to simulate microscopic hydrodynamic phenomena [Hoogerbrugge & Koelman, 1992]. It consists of two parts, a random force

$$\mathbf{F}_{ij}^r = \sigma \omega^R(r_{ij}) \xi_{ij} \hat{\mathbf{r}}_{ij} \quad (2.5)$$

and a dissipative force

$$\mathbf{F}_{ij}^d = -\gamma \omega^D(r_{ij}) (\mathbf{v}_{ij} \cdot \hat{\mathbf{r}}_{ij}) \hat{\mathbf{r}}_{ij}, \quad (2.6)$$

where σ is the strength of the random force, γ is the strength of the dissipative force, $\xi_{ij} = \xi_{ji}$ is a symmetric Gaussian random variable with zero mean and unit variance, $\mathbf{v}_{ij} = \mathbf{v}_j - \mathbf{v}_i$ is the relative velocity, and $\omega^{R/D}(r_{ij})$ are weight functions. The parameters of both forces are not independent but, instead, are coupled through a fluctuation-dissipation relation [Español & Warren, 1995]. This coupling leads to

$$\omega^D(r_{ij}) = [\omega^R(r_{ij})]^2 \quad (2.7)$$

and

$$\sigma^2 = 2\gamma k_B T. \quad (2.8)$$

Here, T has to be understood as an effective temperature, characterizing the magnitude of fluctuations and not as an ambient temperature. It represents the random noise due to the stochastic nature of many related biological processes. For example, the cytoskeleton that determines cell shape is a dynamic structure, which exhibits a constant turnover of material (parts of it are constantly created or removed). Another example would be the variation of adhesion molecules at the surface of cells, which is also random in nature. The parameters for intra- and intercellular dissipation and random fluctuations can be chosen independently. In principle, this noise is active and, thus, does not necessarily satisfy the

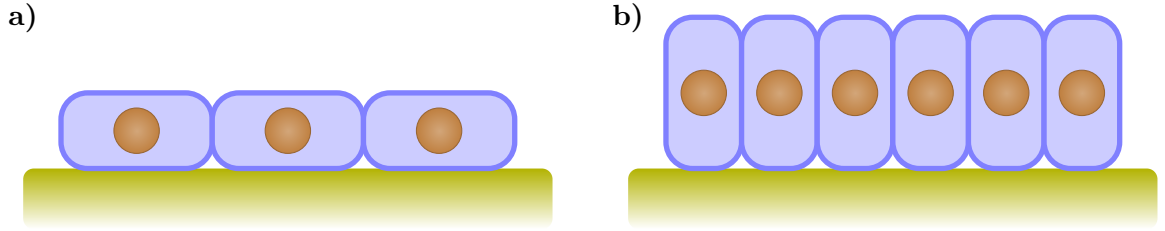


Figure 2.2: Sketch of low and high cell density in a cell sheet. a) Low cell density, where cells are flat and spread over a large area. b) High cell density, where cells become columnar and, thus, reduce their basal area, while retaining their volume.

fluctuation-dissipation relation. As a minimal model, however, we consider an effective temperature as the simplest form of noise.

We define a standard parameter set as in [Montel et al., 2011, 2012]. All quantities denoted with a * are in terms of this standard parameter set (for example the growth force strength $B^* = B/B^{std}$). See table A.1 for a comprehensive list of all parameters.

2.1.2 Modelling monolayered tissues

In order to adapt the above introduced simulation model to describe monolayered tissues (e.g. epithelia) some considerations have to be made. More important than in 3d, one has to differentiate between cell compressibility and cell deformability in 2d. While a high compressibility mostly implies a high deformability, the reverse is not true. For example, during the apical constriction of epithelial cells (i.e. a constriction at the top), their volume was measured to be conserved by basal lengthening [Gelbart et al., 2012]. That means, cells are highly deformable while not being compressible. In consequence, the cells in monolayered sheets are able to stretch into the third dimension, when compressed (see figure 2.2). To account for this effect, the volume exclusion force \mathbf{F}_{ij}^v is altered

$$\mathbf{F}_{ij}^v = f_0 \left(\frac{1}{|\mathbf{r}_{ij}|} - 1 \right) \hat{\mathbf{r}}_{ij}, \quad (2.9)$$

thus, increasing the compressibility. It is, however, noteworthy that the depicted high density regime can have other biological consequences, which we do not consider in the model. For example, the larger contact area between the cells in a high density regime can lead to the cessation of proliferation due to contact inhibition (see e.g. [Alberts, 2008]).

Another important difference between 3d cell aggregates and 2d cell sheets lies in the

typical environment of cells. The natural environment of a cell in 3d is another cell and, thus, background friction should not dominate the dynamics. Furthermore, the forces have to be balanced within the tissue. In contrast, cell sheets have to adhere to a substrate with which they heavily interact, leading to a considerable background friction. Therefore, the background friction coefficient is increased to $\gamma_{bg} = 10$.

To achieve a greater diversity in cell sizes, cell division does not occur instantly as soon as the threshold distance r_{ct} is reached. Instead, a rate k_{div} is defined at which cells of a size exceeding r_{ct} divide. Furthermore, the distance threshold is reduced to $r_{ct} = 0.4$. See table A.2 for a comprehensive list of all model parameters and their standard values.

So far, the outlined model does only incorporate passive cell motion, caused by the interaction between different cells. However, many cell types possess machineries for directed motion. Even more, an aggregation of such motile cells demonstrates interesting collective behavior, which can only arise due to some kind of cell-velocity coupling. One such coupling is called the Vicsek model [Vicsek et al., 1995]. Therein, cells align their motility direction with the local average velocity of their neighbors. While this does make sense for higher organisms like birds, we are not aware of any known mechanism that would enable cells to measure and average over the velocities of its neighbors. A biologically more plausible coupling mechanism was proposed, where cells tend to align their motility direction with their own velocity and, thus, depends on the local mechanical interactions [Basan et al., 2013]. It was able to reproduce the experimentally observed phenomena mentioned in the introduction.

The model defines three distinct cell states. Starting from a non-motile (i.e. passive) state, cells turn motile with a rate k_{mot} , upon which a random motility direction \mathbf{e}_i^m is chosen. If this direction is aligned with the local velocity \mathbf{v}_i of the cell, it changes back into a non-motile state by a rate k^+ . However, if \mathbf{e}_i^m is not aligned with \mathbf{v}_i , it turns non-motile with a higher rate $k^- > k^+$ (see figure 2.3). An aligned state is defined through the following relation

$$\mathbf{e}_i^m \cdot \mathbf{v}_i \geq 0. \quad (2.10)$$

Motile cells are propelled with a constant force $\mathbf{F}_i^m = m\mathbf{e}_i^m$ that is added in the cell force calculation until they revert back to a non-motile state. Since the used dissipative particle dynamics-like thermostat introduces high fluctuations in the instantaneous cell velocity \mathbf{v}^i ,

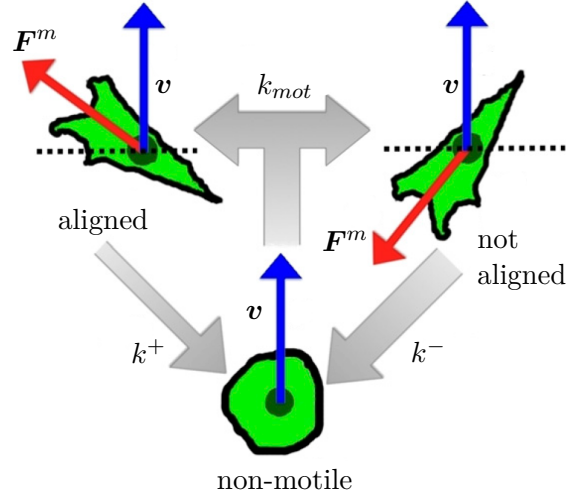


Figure 2.3: Sketch of the motility model. Cells are either non-motile, motile and aligned or motile and not aligned and change their state with the rates k_{mot} , k^+ and k^- . The differentiation between aligned and unaligned motile cells is characterized by the relation between the motility force \mathbf{F}^m and the local cell velocity \mathbf{v} . Taken from [Basan et al., 2013].

\mathbf{v} refers to an averaged, effective cell velocity \mathbf{v}^m that is calculated as follows:

$$\mathbf{v}^m(t) = \int_0^t \frac{\mathbf{v}^i(t') - \mathbf{v}^m(t')}{\tau_{rel}} dt'. \quad (2.11)$$

Thus, the effective velocity relaxes exponentially back to the instantaneous velocity with a relaxation time constant τ_{rel} .

2.1.3 Solving the equations of motion

Having defined all particle interactions, we can now calculate the forces in a system of N particles for any given configuration $\{(\mathbf{r}_1, \mathbf{v}_1), (\mathbf{r}_2, \mathbf{v}_2), \dots, (\mathbf{r}_N, \mathbf{v}_N)\}$, where \mathbf{r}_i and \mathbf{v}_i refer to the position and velocity of particle i . The movement of each particle is governed by Newtons second law of motion

$$\mathbf{F} = m\mathbf{a} = m\ddot{\mathbf{r}}. \quad (2.12)$$

Thus, we have to solve N coupled differential equations. Since already the three-body problem has no closed analytical solution, we have to revert to a numerical approach. This is done extensively, for example, in molecular dynamics (MD) simulations, where molecular systems are described on an atomistic scale. Each atom is represented by a point particle that interacts with certain predefined potentials and its movement is governed by the numerical integration of Newton's equation of motion. A commonly used algorithm for this kind of numerical integration is called velocity verlet. Its advantage over simpler methods like, for example, the Euler method is its higher accuracy in the velocity without additional computational effort and a better stability. The velocity verlet algorithm works as follows. To calculate the positions \mathbf{r}_i and velocities \mathbf{v}_i at the next time step $t + \Delta t$, one first computes the half step velocity at $t + 1/2\Delta t$

$$\mathbf{v}_i(t + 1/2\Delta t) = \mathbf{v}_i(t) + \frac{1}{2m}\mathbf{F}_i(t)\Delta t. \quad (2.13)$$

Then, the positions \mathbf{r}_i at $t + \Delta t$ are updated

$$\mathbf{r}_i(t + \Delta t) = \mathbf{r}_i(t) + \mathbf{v}_i(t + 1/2\Delta t)\Delta t. \quad (2.14)$$

Afterwards, the new forces $\mathbf{F}_i(t + \Delta t)$ are derived from the new positions $\mathbf{r}_i(t + \Delta t)$. To conclude one integration step, the velocity for the full time step is now calculated

$$\mathbf{v}_i(t + \Delta t) = \mathbf{v}_i(t + 1/2\Delta t) + \frac{1}{2m}\mathbf{F}_i(t + \Delta t)\Delta t. \quad (2.15)$$

However, in dissipative particle dynamics (DPD) simulations, the dissipative forces depend on the velocity and, thus, after an integration step, the velocities $\mathbf{v}_i(t + \Delta t)$ are not consistent with the forces $\mathbf{F}_i(t + \Delta t)$. To correct for this inconsistency, a self-consistent version of the velocity verlet algorithm has been developed (see e.g. [Nikunen et al., 2003, Pagonabarraga et al., 1998]). This self-consistent version starts similarly to the original velocity-verlet by the determination of a half step velocity

$$\mathbf{v}_i(t + 1/2\Delta t) = \mathbf{v}_i(t) + \frac{1}{2m}(\mathbf{F}_i^c\Delta t + \mathbf{F}_i^d\Delta t + \mathbf{F}_i^r\sqrt{\Delta t}). \quad (2.16)$$

Here, \mathbf{F}_i^c is the sum of all forces on particle i , except the dissipative force \mathbf{F}_i^d and the

random force \mathbf{F}_i^r . Next, the positions at $t + \Delta t$ are updated as before

$$\mathbf{r}_i(t + \Delta t) = \mathbf{r}_i(t) + \mathbf{v}_i(t + 1/2\Delta t)\Delta t. \quad (2.17)$$

Now, the new forces \mathbf{F}_i^c , \mathbf{F}_i^d and \mathbf{F}_i^r at $t + \Delta t$ are determined by the positions $\mathbf{r}_i(t + \Delta t)$ and the velocities $\mathbf{v}_i(t + 1/2\Delta t)$. Afterwards, the full step velocities are calculated as before

$$\begin{aligned} \mathbf{v}_i(t + \Delta t) = & \mathbf{v}_i(t + 1/2\Delta t) \\ & + \frac{1}{2m}(\mathbf{F}_i^c(t + \Delta t)\Delta t + \mathbf{F}_i^d(t + \Delta t)\Delta t + \mathbf{F}_i^r(t + \Delta t)\sqrt{\Delta t}). \end{aligned} \quad (2.18)$$

To obtain consistency, the dissipative forces \mathbf{F}_i^d are reevaluated with the full step velocities and the velocities change to

$$\mathbf{v}_i(t + \Delta t) = \mathbf{v}_i(t + \Delta t) + \frac{1}{2m}\mathbf{F}_i^d\Delta t. \quad (2.19)$$

The last two steps of recalculation of the dissipative forces and correcting the velocities can be repeated several times until the desired accuracy of consistency is achieved. We use this self-consistent version of the velocity verlet algorithm with no additional refinement steps.

2.1.4 Performance

The above algorithm spends most of the time in the force calculations since for a N particle system N^2 interactions have to be evaluated. However, all the involved forces have a rather short range, which makes most of the calculations superfluous. This problem is circumvented by the implementation of an efficient neighbor list through a boxing method [Allen, 1987] and a verlet list [Verlet, 1967].

Boxing algorithm

The boxing algorithm works as follows. First, the simulation box is divided into smaller boxes of size R_{pp} , the particle-particle interaction range. Then, all particles are sorted into these boxes. Due to the choice of their size, we now know that particles in one box can only interact with those in directly adjacent boxes, which drastically reduces the number of distance calculations between particles that do not interact. The sorting of particles

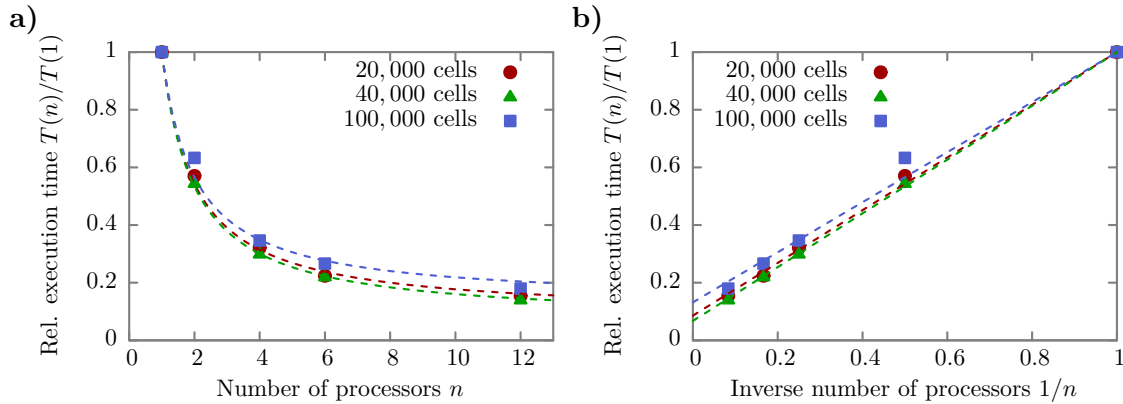


Figure 2.4: Parallelization scalability. **a)** The relative execution time $T(n)/T(1)$ of a model system running for a fixed number of integration steps as a function of the number of processors n . Dashed lines correspond to a fit of Amdahl's law. **b)** Same as in **a)** but as a function of the inverse number of processors $1/n$. Dashed lines correspond to same fits as in **a)**.

into the small boxes is an operation that is linear in the number of particles N , thus, leading to an overall performance gain.

Verlet list

Another approach to efficient particle interaction calculations uses a book-keeping method. Every n integration steps, the distance between all particles is calculated. All particle indices that are within a certain distance R_v of a particle are saved as its neighbors in a list. This list is then used to calculate the particle interactions. Choosing a distance $R_v = R_{pp} + \delta$ that is larger than the interaction range R_{pp} , the neighbor or verlet list (named after Loupe Verlet) has to be updated only every n integration steps, where $n > 1$ has to be suitably chosen. It is also possible to keep track of all particle displacements since the last verlet list calculation and only update the list, when the two largest displacements exceed δ . To maximize performance, we used the boxing algorithm in the creation of the verlet list, thus, combining the advantages of both methods. Furthermore, we keep track of all particle displacements and only reevaluate the verlet list, when the above mentioned criterion is met.

	20,000 cells	40,000 cells	100,000 cells
B	0.09 ± 0.01	0.07 ± 0.01	0.13 ± 0.02
S	11.1 ± 1.2	14.3 ± 2.1	7.7 ± 1.2

Table 2.1: Fitting results of Amdahl’s law. The serial fraction coefficient B describes the fraction of the simulation code that cannot run in parallel, while S refers to the according maximum speedup. Extracted from a fit of equation (2.20) as seen in figure 2.4.

Parallelization

To further speed up the computation times and to make it feasible to simulate systems of the order of 100,000 particles, we made use of the broad availability of multi-core computing machines. The simulation code was parallelized, facilitating the well known OpenMP application programming interface that supports multi-platform shared memory multiprocessing programming. To verify the scalability of the simulation code, we measured the execution time of a tissue spheroid in steady state for a fixed set of integration steps with 20,000, 40,000, and 100,000 cells (i.e. twice as many particles), depending on the number of processors used. According to Amdahl’s law, the execution time $T(n)$ as a function of the number of parallel processes n follows

$$T(n) = T(1) \left[B + \frac{1}{n}(1 - B) \right], \quad (2.20)$$

where B refers to the serial fraction of the code. As seen in figure 2.4, this fits quite well the simulation code timing and yields a theoretical speedup $S = 1/B$ of roughly 10 (see table 2.1).

2.1.5 Boundary conditions

We implemented several different boundary conditions to study a broad range of phenomena. The most basic and well defined ones are the bounce-back boundary condition (BBC), the reflective boundary condition (RBC), and the periodic boundary condition (PBC). The later simply maps the coordinates of all particles back into the so called unit cell (see figure 2.5a), which is useful to study bulk phenomena. BBCs and RBCs, on the other hand, describe hard walls with no slip and infinite slip, respectively. In this context, no slip (BBC) refers to zero velocity at the wall, which is ensured by changing the velocity according to $\mathbf{v}' = -\mathbf{v}$ (see figure 2.5b). For the infinite slip (RBC), the component of the

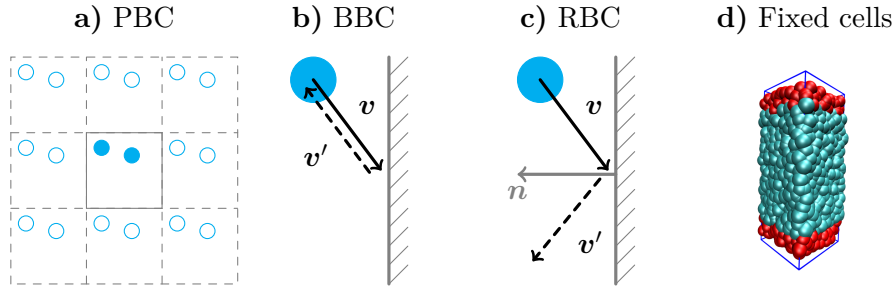


Figure 2.5: Sketch of different boundary conditions used in the simulations. **a)** Periodic boundaries. Solid lines and closed circles represent the unit cell. Dashed lines and open circles represent the periodic images of the unit cell. **b)** Bounce-back boundaries reflect particles back on its incidental trajectory. **c)** Reflective boundaries change only the velocity component perpendicular to the wall. **d)** Simulation snapshot of fixed cells boundaries. Red particles are fixed with a harmonic potential and not allowed to divide nor die. Normal cells are shown in cyan and the simulation box in blue.

velocity parallel to the normal of the wall \mathbf{n} is changed according to $\mathbf{v}' = \mathbf{v} - 2(\mathbf{n} \cdot \mathbf{v})\mathbf{n}$ (see figure 2.5c). Instead of the aforementioned types, it is also possible to use open boundaries, which puts no spatial constraints on the particle movement. We can independently choose a boundary condition for each spatial dimension.

Apart from the aforementioned, we implemented another type of boundaries, which we call *fixed cells*. Instead of hard walls, we put a layer of cells at each end of a box in one direction (see figure 2.5d) and employ periodic boundaries in the other two spatial directions. The particles of the two layers are each subjected to a strong harmonic potential, effectively freezing them at their current position. Furthermore, these cells are neither allowed to divide nor die but otherwise interact in the same way as normal cells. A tissue seeded at the bottom of such a set-up, adheres to the layer of fixed cells, and starts to grow until it completely fills the compartment. The fixed cells create boundaries that resemble the bulk of a tissue very similar to the periodic boundaries. However, in contrast to PBCs, one can sum over the forces acting on the fixed cells and therefrom determine the stress state in the bulk.

2.1.6 Reduced units

In physics in general, problems can often be simplified and parameterized by dedimensionalization. This is especially useful in computer simulations because the results of such dimensionless simulation runs can be scaled to a whole class of systems described by the

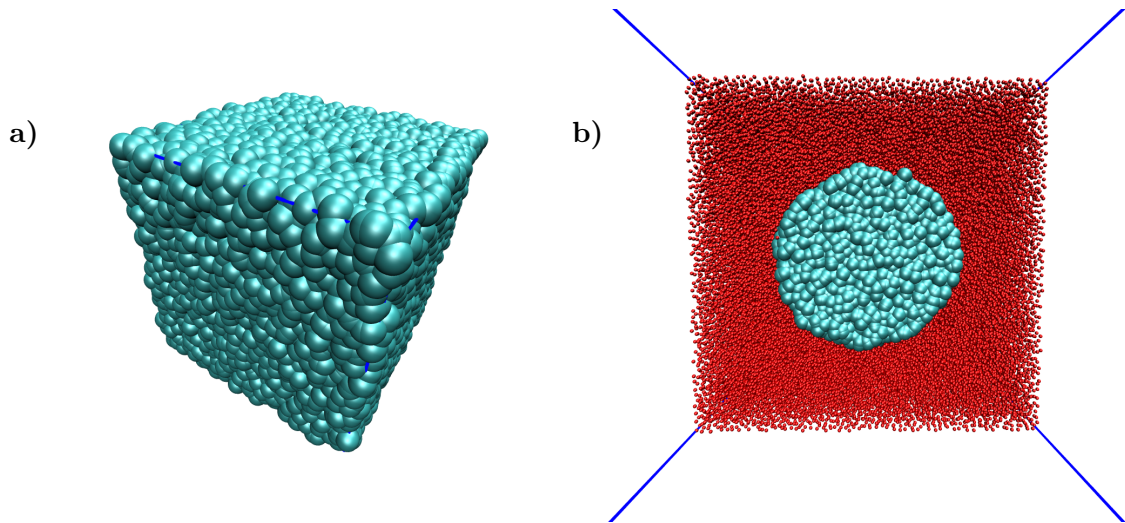


Figure 2.6: Simulation snapshots of different methods to impose stress. **a)** Snapshot of a tissue in a box with full periodic boundaries. The box size is dynamically rescaled to ensure a constant pressure. **b)** Snapshot of a cut through a tissue spheroid (cyan) embedded in a gas of smaller particles (red) that only interact via volume exclusion. The simulation box consists of hard walls in all directions.

same model. Furthermore, the simulations then calculate numerical values on the order of unity, which is always desirable due to the finite accuracy of computers.

However, there is another problem involved. The feasibility of computer simulations often depend on the contraction of time and length scales [Padding & Louis, 2006]. The time scale of diffusion of a colloid in water, to use the example of Padding & Louis, is several orders of magnitude larger than the typical time of the movement of individual water molecules. Considering all involved processes span up to 15 orders of magnitude. Thus, a coarse-graining or compaction of time (and length) is necessary. This, on the other hand, means that not all involved quantities can be compared simultaneously with a physical system of interest. However, carefully choosing characteristic scales to relate simulations to experiments still leads to a meaningful comparison. Unless explicit units are given, the simulation results presented in this thesis are in terms of simulation units.

2.1.7 Constant pressure ensemble

In order to study the bulk behavior of tissue growth under constant pressure, we implemented a method we call *constant pressure ensemble* as outlined in [Allen, 1987]. This

method imposes a defined pressure P^i on a system with full periodic boundaries by rescaling the volume of the simulation box by a factor

$$\chi = 1 - \beta_T \frac{\Delta t}{t_P} (P^i - P), \quad (2.21)$$

where β_T is the isothermal compressibility, t_P is the relaxation time the system needs to adapt to the imposed pressure P^i , Δt is the simulation time step and P is the current pressure inside the simulation box. In this context, we define this pressure as $P = -1/3 \text{Tr} \sigma_{\alpha\beta}$. Furthermore, the center of mass positions of all cells are rescaled by $\sqrt[3]{\chi}$. As there is in principle no constraint on P^i , it is possible to simulate systems under tension ($P^i < 0$) as well as compression. A snapshot of such a simulation is shown in figure 2.6a.

2.1.8 Gas particle method

Another possibility of exerting pressure on growing tissues in our simulation closely resembles an established experimental method [Montel et al., 2011]. This method utilizes the fact that a big polymer (in their case Dextran) is not able to penetrate either the cells itself nor a growing tissue spheroid as a whole. Therefore, the Dextran creates a density gradient, which results in an osmotic pressure exerted onto the first few cell layers of the tissue spheroid. This method can be mimicked in our simulations. Simple particles assume the role of Dextran that only interact through a volume exclusion force. This force is similar to the above defined, only differing in the choice of the prefactor f_0 . We chose $f_0^{gas} = 0.1$. The actual simulation consists of a large simulation box with hard walls, into which we put a tissue spheroid surrounded by gas particles. The pressure exerted by these particles onto the spheroid is determined by their number, their size and the accessible volume. Since the gas particles are reflected by the hard walls upon encounter, the momentum transfer $\sum_i \Delta p_i$ during a small time interval Δt can be measured and therefrom the exerted pressure $P = \sum_i \Delta p_i / \Delta t$ is calculated. A simulation snapshot of a tissue spheroid with gas particles is shown in figure 2.6b.

2.1.9 Stress measurements

Stress measurement in MD is a topic of controversial debate. There are several proposed methods, which make different assumptions. At this point, we refer the interested reader

to [Admal & Tadmor, 2010] for a comprehensive review and rigorous derivation of stress measurements in MD simulations.

An acknowledged way of obtaining the pressure uses the momentum transfer on hard walls, which is only applicable in systems with either BBCs or RBCs and requires a constant interaction of the simulated particles with the walls. Thus, only extensional systems produce a measurable quantity. To circumvent this shortcoming, we implemented the aforementioned fixed cells boundaries, which can also measure tensional stresses. The net force acting on the fixed cells must be compensated by their harmonic potentials, keeping them in place. The sum over all the forces of the harmonic potentials then equal the overall principal tension or compression exerted by the tissue.

However, all these methods only measure at the boundary. In order to get a detailed description of the full stress tensor in the bulk, we implemented a method very similar to the one proposed by Tsai [1979]. The stress $\sigma_{\alpha\beta}^P$ at any point P in our simulation box is calculated by measuring the forces and the momentum transfer during a short time Δt through three perpendicular but otherwise arbitrary planes that intersect in P :

$$\sigma_{\alpha\beta}^P = -\frac{1}{A} \left[\sum_i \frac{m_i v_{\beta}^i}{\Delta t} + \sum_{i,j} F_{\beta}^{ij} \right], \quad (2.22)$$

where \sum_i sums over all particles i that pass through the plane with area A , $\sum_{i,j}$ sums over all pair interactions that act through A , m_i is the mass of particle i , v_{β}^i is the β th component of the velocity of particle i and F_{β}^{ij} is the β th component of the force acting on i due to j through A with the convention that F is negative for attractive forces and positive for repulsive forces. Now consider a small volume $\delta V = \delta l^3$. The average $\sigma_{\alpha\beta}^{\delta V}$ over all planes x - y , x - z and y - z with area $\delta A = \delta l^2$ that lie within δV then reads

$$\sigma_{\alpha\beta}^{\delta V} = -\frac{1}{\delta V} \left[\sum_i \frac{m_i v_{\beta}^i \Delta r_{\alpha}^i}{\Delta t} + \sum_{i,j} r_{\alpha}^{ij} F_{\beta}^{ij} \right], \quad (2.23)$$

with $r_{\alpha}^{ij} = r_{\alpha}^j - r_{\alpha}^i$ the α th component of the distance between i and j that lies within the volume δV , Δr_{α}^i the α th component of the part of the distance i moved during Δt that lies within δV .

In the case of homogeneous bulk simulations with full periodic boundaries, equation (2.23)

simplifies to the Virial stress

$$\sigma_{\alpha\beta} = -\frac{1}{V} \left[\sum_i m_i v_\beta^i v_\alpha^i + \sum_{i,j} r_\alpha^{ij} F_\beta^{ij} \right], \quad (2.24)$$

by setting $\delta V = V$, where $V = L_x L_y L_z$ is the simulation box volume.

Stress measurements in motility simulations

In principle, the local stress in simulations of monolayered motile tissues can be measured with the method outlined above. However, force balance requires

$$\nabla \cdot (\boldsymbol{\sigma} \cdot \mathbf{e}_\alpha) + f_\alpha^{ext} = 0, \quad (2.25)$$

where $\boldsymbol{\sigma}$ is the full stress tensor and f_α^{ext} is the force density in α direction per unit volume and mass acting on the system (the substrate/motility force). In the case of two dimensions, integration over x and averaging over y yields

$$\int_{x_0}^x \partial_{x'} \sigma_{xx}(x') dx' + \int_{x_0}^x \partial_y \sigma_{yx}(x') dx' + \int_{x_0}^x f_x^{ext}(x') dx' = 0 \quad (2.26)$$

$$\sigma_{xx}(x) - \sigma_{xx}(x_0) + \int_{x_0}^x \partial_y \sigma_{yx}(x') dx' + \int_{x_0}^x f_x^{ext}(x') dx' = 0 \quad (2.27)$$

$$\langle \sigma_{xx}(x) \rangle_y = - \int_{x_0}^x \langle f_x^{ext}(x') \rangle_y dx' + \langle \sigma_{xx}(x_0) \rangle_y. \quad (2.28)$$

We assumed that $\langle \int_{x_0}^x \partial_y \sigma_{yx}(x') dx' \rangle_y = 0$ since all the motility related simulations presented in this thesis are symmetric along y . Thus, the stress in x direction can be easily determined by the integration of the motility and background forces.

2.1.10 Density

In the following, we define the density ρ as the number density, calculated from the cell positions \mathbf{x}_i . Hence, for any arbitrary volume V , the density reads

$$\rho = \frac{\int_V \delta(\mathbf{x} - \mathbf{x}_i) d\mathbf{x}}{\int_V d\mathbf{x}}. \quad (2.29)$$

In the simulations, the cell position refers to the center of mass of the particles constituting a cell.

2.1.11 Cell division

We define the division axis \mathbf{d} of a proliferating cell via the positions of its two daughters \mathbf{x}_1 and \mathbf{x}_2 through

$$\mathbf{d} = \frac{\mathbf{x}_1 - \mathbf{x}_2}{|\mathbf{x}_1 - \mathbf{x}_2|}. \quad (2.30)$$

and the position \mathbf{x}_d as

$$\mathbf{x}_d = \frac{\mathbf{x}_1 + \mathbf{x}_2}{2}. \quad (2.31)$$

The division rate k_d , thus, becomes the number of divisions n_d occurring during the time Δt over the total number of cells N :

$$k_d = \frac{n_d}{N\Delta t}. \quad (2.32)$$

Considering the number of cells N instead of the density ρ , the continuity equation then reads

$$\partial_t N + \nabla \cdot (N\mathbf{v}) = (k_d - k_a)N \quad (2.33)$$

$$\Rightarrow \frac{\partial_t N}{N} = k_d - k_a - \frac{\nabla \cdot (N\mathbf{v})}{N}. \quad (2.34)$$

2.1.12 Tissue competition set-up

Fixed boundaries

In order to study the interface dynamics of competing tissues, we utilize the same simulation method introduced in section 2.1.1 with a slightly different parameter set. Two tissues are placed in a rectangular box with BBCs in x and PBCs in y direction (see figure 2.7). Furthermore, we confine the cell movement to two dimensions. Both tissues share basically the same parameter set, defined in table A.1, with a few alterations. The adhesion force is reduced to $f_1 = 5$, while the background friction is increased to $\gamma_{bg} = 10$. To get different bulk homeostatic pressures, the growth force strength B is varied. We define the

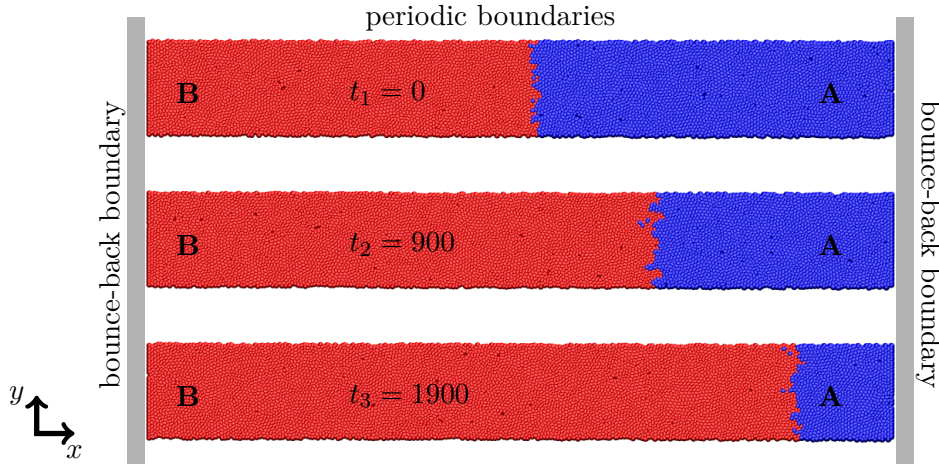


Figure 2.7: Fixed boundaries tissue competition simulation set-up. Three Snapshots at different time t_i of a simulation with $L_y = 20$ and $L_x = 160$. At $x = 0$ and $x = L_x$ BBCs are used, while at $y = 0$ and $y = L_y$ PBCs are used.

standard values for the tissues A and B as $B_A = 50$ and $B_B = 60$. Since the division rate increases with higher B , the intracell friction coefficient was also changed to $\gamma_c = 2B$ so that different growth forces still result in roughly the same division rate for unconstrained growth.

Treadmilling

We mentioned in the introduction that we want to study, among other things, the scaling behavior of the interface of competing tissues. This requires long simulation runs, to ensure that the saturated interface width regime has been reached. However, since one tissue is constantly pushing the other aside, the finite size of the simulation box also implies a maximum simulation time length. Especially for larger system sizes, the fixed boundaries approach is simply not feasible.

To evade this problem, we designed a set-up with a comoving simulation box, we call *treadmilling*. In such a set-up, the tissues close to the interface have to feel essentially as in bulk and reasonably far away from the interface, they have to reach their homeostatic pressure. Again, two tissues with different homeostatic pressure are put into the same simulation box as before. All cells, entering a small region near both hard walls, are taken out of the simulation (see figure 2.8). While the tissue with the higher P_H continuously

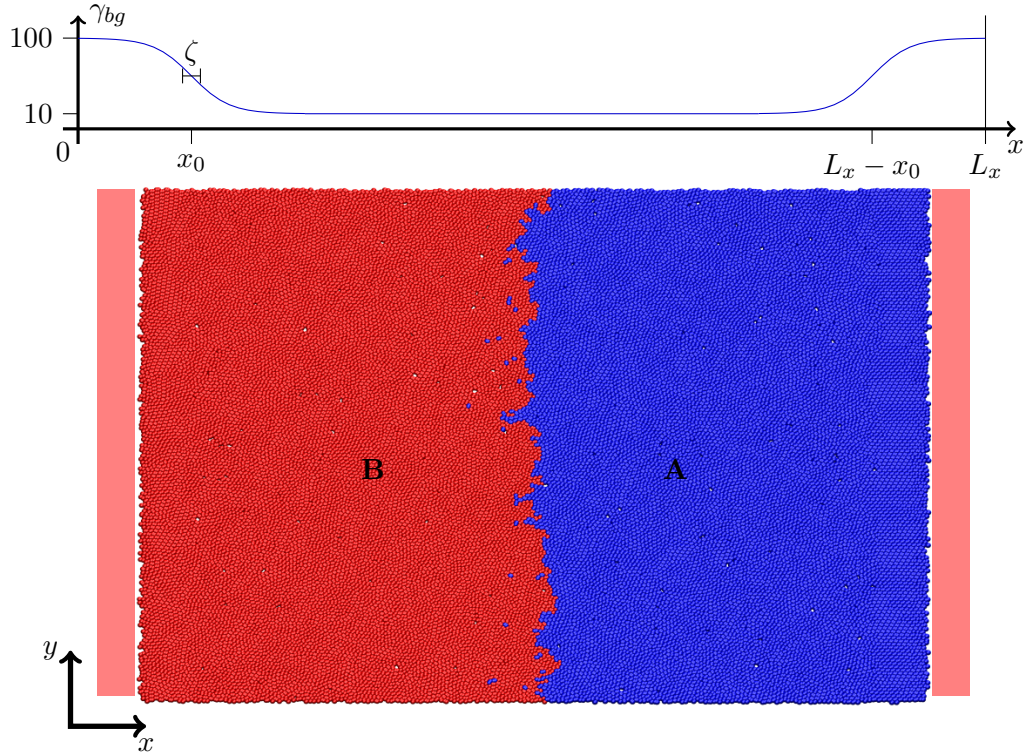


Figure 2.8: Treadmilling simulation set-up. Snapshot of a simulation with $L_y = 100$ and $L_x = 140$. The background friction γ_{bg} is varied according to the x position as shown in the upper plot. All cells that move into the zones colored lightly red are taken out of the simulation.

pushes the other aside, the interface is kept at $L_x/2$ by displacing all cells every 1000 integration steps by $\Delta x = L_x/2 - x_{int}$ with the interface position x_{int} as defined in section 3.2.2. Thus, cells of tissue B are constantly removed at $x = 0$ and the additional free space at $x = L_x$ is quickly filled by tissue A. In order to decrease flux contributions, we increase the background friction near both death zones continuously from $\gamma_{bg} = 10$ to $\gamma_{bg} = 100$, depending on the x position:

$$\gamma_{bg}(x) = \frac{A}{1 + \exp\left(\frac{x-x_0}{\zeta}\right)} + B. \quad (2.35)$$

The coefficients A and B are determined by the requirement that $\gamma_{bg}(x \gg x_0) = 10$ and $\gamma_{bg}(x \ll x_0) = 100$ for $x_0 = 5$ and vice versa for $x_0 = L_x - 5$. We chose $\zeta = 2$ (see

figure 2.8).

Thus, for all L_y a steady state is reached eventually since this simulation set-up can run indefinitely. Furthermore, a fixed and rather small box size L_x can be chosen that covers a large range of different L_y . The equivalence of the treadmilling and the fixed boundaries set-up is demonstrated in section 3.2.3.

2.2 Theory

2.2.1 Tissue growth of spheroids

It was already mentioned in the introduction that the growth rate k of in vitro experiments of growing tissue spheroids was found to obey a simple two rate model

$$k(r) = \begin{cases} k_b & \text{for } r \leq R - \lambda \\ k_b + \delta k_s & \text{for } r > R - \lambda \end{cases} \quad (2.36)$$

with a bulk growth rate k_b and a surface growth increment δk_s in a small region of thickness λ for a tissue spheroid of size R . For a constant density ρ , the change in spheroid volume $\partial_t V(t)$ reads

$$\partial_t V(t) = \int_V k(\mathbf{r}) d\mathbf{r}. \quad (2.37)$$

Steady state size in 1d

Restricting equation (2.37) to one dimension yields

$$\partial_t V(t) = \int_S k(z) dz \quad (2.38)$$

$$= \int_0^{R-\lambda} k_b dz + \int_{R-\lambda}^R (k_b + \delta k_s) dz \quad (2.39)$$

$$= Rk_b + \delta k_s \lambda. \quad (2.40)$$

A stable steady state ($\partial_t V = 0$) with a size

$$R_{ss}^{\lambda d} = -\frac{\lambda \delta k_s}{k_b}. \quad (2.41)$$

only arise for $k_b < 0$ and $k_b + \delta k_s > 0$.

Steady state size in 3d

For a radially symmetric spheroid in three dimensions the change in volume is described by

$$\partial_t V = 4\pi \int_0^{R-\lambda} k_b r^2 dr + 4\pi \int_{R-\lambda}^R (k_b + \delta k_s) r^2 dr \quad (2.42)$$

$$= 4\pi k_b \int_0^R r^2 dr + 4\pi \delta k_s \int_{R-\lambda}^R r^2 dr \quad (2.43)$$

$$= \frac{4}{3}\pi R^3 k_b + \frac{4}{3}\pi \delta k_s (3R^2 \lambda - 3R\lambda^2 + \lambda^3). \quad (2.44)$$

For a small surface growth region thickness $\lambda \ll R$, this simplifies to

$$\partial_t V = \frac{4}{3}\pi R^3 k_b + 4\pi R^2 \lambda \delta k_s. \quad (2.45)$$

Again, a stable steady state ($\partial_t V = 0$) can only arise if $k_b < 0$ and $k_b + \delta k_s > 0$. The associated steady state size R_{ss} is given by

$$R_{ss} = -\frac{3\lambda \delta k_s}{k_b}. \quad (2.46)$$

An unstable steady state exists for $k_b > 0$ and $k_b + \delta k_s < 0$ but any perturbation would either result in infinite growth or complete death.

Without an external pressure, equation (1.2), the expansion of the growth rate in terms of the pressure difference up to linear order, and equation (2.46) relate the steady state size R_{ss} to the homeostatic pressure P_H via

$$R_{ss} = -\frac{3\lambda \delta k_s}{\kappa P_H}, \quad (2.47)$$

which shows a directly inverse dependence of the steady state radius on the homeostatic pressure.

2.2.2 Characterizing flow in tissue spheroids

In the context of the two rate model, stable steady state solutions require a negative bulk growth rate ($k_b < 0$) and a positive surface growth rate ($k_b + \delta k_s > 0$). Thus, a flux of cells has to balance the surface excess and the apoptotic core to maintain a stable spheroid. The velocity field \mathbf{v} resulting from the anisotropic net growth rate has to obey

$$\nabla \cdot \mathbf{v} = k \quad (2.48)$$

and follows from equation (1.1) under the assumption of a constant cell density ρ . It can be understood as a generalized incompressibility condition.

Velocity profile in 1d

Using the same definition of k as before, equation (2.48) yields in one dimension

$$v(z) = \begin{cases} k_b z & \text{for } z \leq R - \lambda \\ (k_b + \delta k_s)z - \delta k_s(R - \lambda) & \text{for } z > R - \lambda. \end{cases} \quad (2.49)$$

The integration constants were determined by the boundary condition $v(z = 0) = 0$ and the constraint of continuity of v at $z = R - \lambda$. The velocity $v(z = R)$ describes the expansion velocity.

Velocity profile in 3d

Due to spherical symmetry in the case of three dimensions, equation (2.48) simplifies to

$$\partial_r(r^2 v(r)) = r^2 k(r). \quad (2.50)$$

Integrating over r results in

$$v(r) = \frac{1}{r^2} \int_0^r r'^2 k(r') dr' + \frac{A}{r^2}. \quad (2.51)$$

The boundary condition $v(0) = 0$ requires $A = 0$. Using again the same two rate growth model then yields

$$v(r) = \begin{cases} r^{-2} \int_0^r r'^2 k_b \, dr' & \text{for } r \leq R - \lambda \\ r^{-2} \left(\int_0^{R-\lambda} r'^2 k_b \, dr' + \int_{R-\lambda}^r r'^2 (k_b + \delta k_s) \, dr' \right) & \text{for } R - \lambda < r \leq R \end{cases} \quad (2.52)$$

$$= \begin{cases} \frac{1}{3} k_b r & \text{for } r \leq R - \lambda \\ \frac{1}{3} (k_b + \delta k_s) r - \frac{1}{3} \delta k_s \frac{(R-\lambda)^3}{r^2} & \text{for } R - \lambda < r \leq R. \end{cases} \quad (2.53)$$

Thus, a similar linear regime is seen in the bulk for 3d compared to 1d but with a different slope. Near the surface, however, the 3d velocity profile has an additional term that scales with $1/r^2$. Measuring this velocity profile allows for an independent estimate of k_b and δk_s .

2.2.3 Simple tissue competition

In the case of two incompressible tissues A and B in a finite sized compartment with the same homeostatic density ρ_H and negligible elastic and viscous forces, the resulting dynamics can be expressed by simple number balance. Due to the finite size and incom-

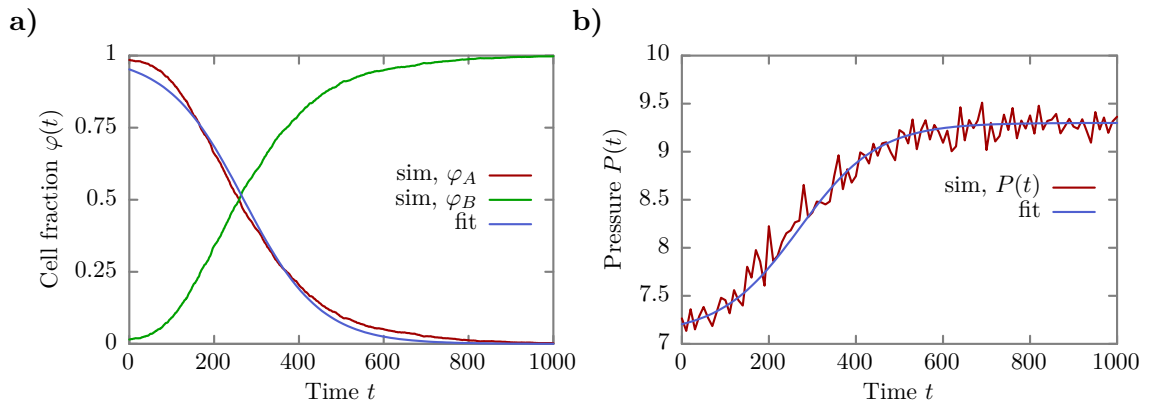


Figure 2.9: Tissue competition. Simulation results of two competing tissues in a box using the simulation method introduced in section 2.1.1. Here, the background friction is set to zero. **a)** Time evolution of the cell fractions $\varphi_{A/B}$ and a fit of equation (2.60). Note that although viscous forces are not negligible in the used simulations, the behavior is still captured very well. **b)** Time evolution of the pressure $P(t)$ inside the box and a fit of equation (2.61). Note again the good agreement.

compressibility, the maximum number of cells N_{tot} is fixed over time and, thus, the growth rates $k^{A/B}$ of the tissues A and B are coupled through

$$\partial_t N_{tot} = 0 = k^A N_A + k^B N_B, \quad (2.54)$$

where N_A is the number of cells of type A (and N_B of type B). Considering only small differences $P_H^{A/B} - P$ in equation (1.2), the pressure dependent growth rates are described by

$$k^{A/B} = \kappa^{A/B} (P_H^{A/B} - P). \quad (2.55)$$

Thus, equation (2.54) can be solved for the pressure P :

$$P = \frac{\kappa^A P_H^A N_A + \kappa^B P_H^B N_B}{\kappa^A N_A + \kappa^B N_B}. \quad (2.56)$$

Assuming equal growth rate coefficients $\kappa^A = \kappa^B = \kappa$, the change in number of tissue A yields

$$k^A N_A = N_A \kappa \left(P_H^A - \frac{P_H^A N_A + P_H^B N_B}{N_A + N_B} \right) \quad (2.57)$$

$$= \kappa \frac{N_A N_B}{N_A + N_B} \Delta P_H, \quad (2.58)$$

which only depends on the homeostatic pressure difference $\Delta P_H = P_H^A - P_H^B$. Defining $\varphi_A = N_A / (N_A + N_B)$ as the fraction of cells of type A, this results in a logistic growth

$$\partial_t \varphi_A = \varphi_A k^A = \kappa \Delta P \varphi_A (1 - \varphi_A). \quad (2.59)$$

The time evolution of the cell fraction is, thus, described by

$$\varphi_A(t) = \frac{1}{1 + \exp[\kappa \Delta P (t - t_0)]} \quad (2.60)$$

and the time evolution of the pressure by

$$P(t) = P_H^A \varphi_A(t) + P_H^B (1 - \varphi(t)). \quad (2.61)$$

However, these results assume a homogeneous stress distribution and negligible background friction, which is unrealistic for real tissues.

2.2.4 Quantifying order

Throughout this thesis but especially in section 3.3 we want to quantify the alignment of different axes, for example the cell division axis and the x axis. In the field of liquid crystals, the order tensor

$$Q_{\alpha\beta} = \frac{1}{N} \sum_{i=1}^N \left(\frac{3}{2} u_{\alpha}^i u_{\beta}^i - \frac{1}{2} \delta_{\alpha\beta} \right) \quad (2.62)$$

is commonly used to characterize the order of N unit vectors \mathbf{u} . This symmetric 3x3 matrix is then diagonalized and the eigenvector \mathbf{n} to its greatest eigenvalue S is called principal director, while the order parameter

$$S = \mathbf{n}^T \mathbf{Q} \mathbf{n} \quad (2.63)$$

characterizes the order along this axis. In general, the order along any arbitrary unit axis $\mathbf{a} = (a_x, a_y, a_z)$ ($|\mathbf{a}| = 1$) is defined as

$$S_a^u = \mathbf{a}^T \mathbf{Q} \mathbf{a}. \quad (2.64)$$

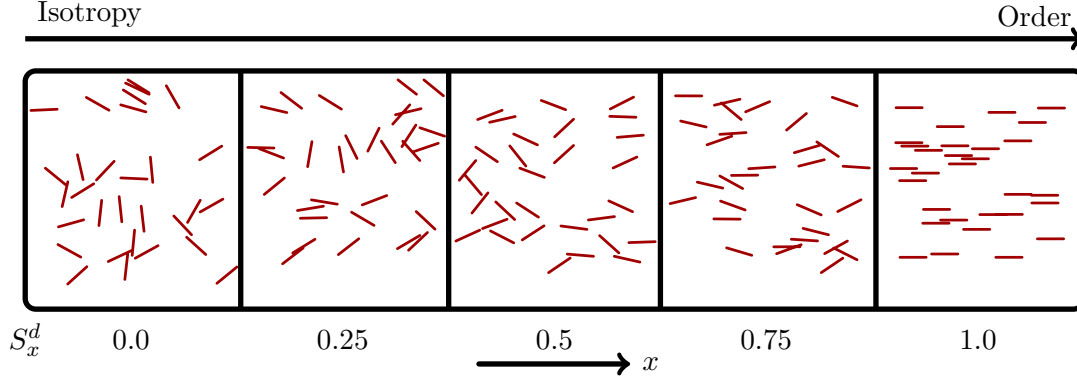


Figure 2.10: Visualization of the order parameter in 2d. Visualization of the order parameter S_x^d in 2d. Each box contains 30 rods that result in the order parameter written below. Redrawn from [Marel et al., 2014].

Using the definition of \mathbf{Q} , this simplifies to

$$S_a^u = (a_x, a_y, a_z) \begin{pmatrix} Q_{xx} & Q_{xy} & Q_{xz} \\ Q_{yx} & Q_{yy} & Q_{yz} \\ Q_{zx} & Q_{zy} & Q_{zz} \end{pmatrix} \begin{pmatrix} a_x \\ a_y \\ a_z \end{pmatrix} \quad (2.65)$$

$$= a_x^2 Q_{xx} + a_x a_y Q_{xy} + a_x a_z Q_{xz} + a_y a_x Q_{yx} + a_y^2 Q_{yy} + a_y a_z Q_{yz} + a_z a_x Q_{zx} + a_z a_y Q_{zy} + a_z^2 Q_{zz} \quad (2.66)$$

$$= \frac{3}{2N} \sum_{i=1}^N \left(a_x^2 u_x^i{}^2 + a_y^2 u_y^i{}^2 + a_z^2 u_z^i{}^2 + 2a_x a_y u_x^i u_y^i + 2a_x a_z u_x^i u_z^i + 2a_y a_z u_y^i u_z^i \right) - \frac{1}{2} (a_x^2 + a_y^2 + a_z^2) \quad (2.67)$$

$$= \frac{3}{2} \langle (a_x u_x^i + a_y u_y^i + a_z u_z^i)^2 \rangle - \frac{1}{2} \quad (2.68)$$

$$= \frac{3}{2} \langle (\mathbf{a} \cdot \mathbf{u}^i)^2 \rangle - \frac{1}{2} = \frac{3}{2} \langle \cos^2 \theta^i \rangle - \frac{1}{2}, \quad (2.69)$$

where θ^i denotes the angle between \mathbf{a} and \mathbf{u}^i and the sum $1/N \sum_i$ was substituted by $\langle \rangle$. Thus, $S_a^u = 1$ refers to a state of perfect alignment, while for $S_a^u = -1/2$ all \mathbf{u}^i lie in the plane with the normal \mathbf{a} . $S_a^u = 0$ corresponds to perfect isotropy.

In two dimensions, however, the definition of \mathbf{Q} is slightly different

$$Q_{\alpha\beta} = \frac{1}{N} \sum_{i=1}^N (2u_{\alpha}^i u_{\beta}^i - \delta_{\alpha\beta}). \quad (2.70)$$

Thus in a 2d system, the order parameter varies between 1 (perfect alignment) and -1 (perfectly perpendicular alignment), while 0 still corresponds to an isotropic state (see figure 2.10).

2.2.5 Interfacial tension

A surface or interface tension γ_s is defined mechanically through a force acting along an interface. Defining P_{\perp} as the pressure perpendicular to this interface and P_{\parallel} as the pressure parallel to this interface, γ_s is determined by (see e.g. [Navascues, 1979])

$$\gamma_s = \int_{-\infty}^{\infty} (P_{\perp}(x) - P_{\parallel}(x)) dx, \quad (2.71)$$

where x refers to the coordinate perpendicular to the interface.

2.2.6 Velocity gradient, strain rate and stress tensor

The velocity gradient tensor \mathbf{L} is defined for a velocity field \mathbf{v} as

$$L_{\alpha\beta} = \partial_{\alpha} v_{\beta} \quad (2.72)$$

and, thus, the velocity gradient $\partial_{\mathbf{a}} v_{\mathbf{a}}$ along any arbitrary axis \mathbf{a} reads

$$\partial_{\mathbf{a}} v_{\mathbf{a}} = \mathbf{a}^{\top} \mathbf{L} \mathbf{a}. \quad (2.73)$$

It can be decomposed into a symmetric part \mathbf{E} and an antisymmetric part \mathbf{W}

$$\mathbf{L} = \underbrace{\frac{1}{2} (\mathbf{L} + \mathbf{L}^{\top})}_{\mathbf{E}} + \underbrace{\frac{1}{2} (\mathbf{L} - \mathbf{L}^{\top})}_{\mathbf{W}}. \quad (2.74)$$

The symmetric part

$$E_{\alpha\beta} = \frac{1}{2} \left(\frac{\partial v_\alpha}{\partial \beta} + \frac{\partial v_\beta}{\partial \alpha} \right) \quad (2.75)$$

is called strain rate tensor and describes the rate of change of the deformation of a material. The antisymmetric part \mathbf{W} is called spin tensor as it is directly connected to the rotation of the velocity field.

In fluids (and most often in complex fluids as well), the stress tensor is directly proportional to the strain rate tensor (see e.g. [Landau & Lifshitz, 1987]). Considering only two dimensions, its diagonalization yields two eigenvalues λ_1 and λ_2 , where $\lambda_1 \geq \lambda_2$ by convention. We call the eigenvector corresponding to the largest eigenvalue $\boldsymbol{\lambda}$. By definition of $E_{\alpha\beta}$, the sum of both eigenvalues equals the divergence of \mathbf{v} . We define the difference $p = \lambda_1 - \lambda_2$ as the dipole strength, due to the similarity of a growing cell to a force dipole. It quantifies the asymmetry of flow gradients and gives an idea of the asymmetry of stress.

Similarly to the definition of p , one can also evaluate the difference in velocity gradients along any two perpendicular but otherwise arbitrary axes \mathbf{a}_\parallel and \mathbf{a}_\perp using equation (2.73):

$$\partial_\parallel v_\parallel - \partial_\perp v_\perp = \mathbf{a}_\parallel^\top \mathbf{L} \mathbf{a}_\parallel - \mathbf{a}_\perp^\top \mathbf{L} \mathbf{a}_\perp = \mathbf{a}_\parallel^\top \mathbf{E} \mathbf{a}_\parallel - \mathbf{a}_\perp^\top \mathbf{E} \mathbf{a}_\perp. \quad (2.76)$$

To illustrate its meaning, let us consider a shear-free incompressible Newtonian fluid in 2d. Its steady state velocity field under a constant stretch rate $\dot{\epsilon} > 0$ can be written as

$$\mathbf{v}(x, y) = \begin{pmatrix} -\dot{\epsilon}x \\ \dot{\epsilon}y \end{pmatrix} \quad (2.77)$$

and is depicted in figure 2.11. Choosing $\mathbf{a}_\parallel = \mathbf{e}_x$ and $\mathbf{a}_\perp = \mathbf{e}_y$, it follows that

$$\partial_\parallel v_\parallel - \partial_\perp v_\perp = \partial_x v_x - \partial_y v_y = -2\dot{\epsilon}. \quad (2.78)$$

The later shows a connection between the stretch rate and the difference in derivatives. Naively speaking, it quantifies the asymmetry in the stretch rates along x and along y .

The velocity gradient reflects the change in velocity with space. It is defined as a continuum quantity through the partial derivatives of a velocity field \mathbf{v} . Since the simulations yield only a finite set of points $\{\mathbf{x}_i\}$ with velocities $\{\mathbf{v}_i\}$, the velocity gradient

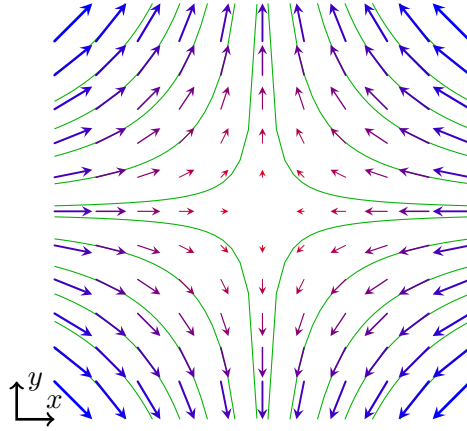


Figure 2.11: Velocity field of steady state planar elongational flow. The velocity field of a steady state planar elongational flow. Modulus of the velocity is color coded (high velocity shown in blue, low velocity in red). Streamlines are displayed in green.

has to be discretized. In order to incorporate as much information into the velocity gradient calculation as possible in simulations as well as in the comparison with experiments, an unconventional way of gradient determination was devised. Being restricted to two dimensions, the individual components of the velocity vector

$$\mathbf{v}(x, y) = \begin{pmatrix} v_x(x, y) \\ v_y(x, y) \end{pmatrix} \quad (2.79)$$

can be seen as surfaces in \mathbb{R}^3 . In analogy to fitting a tangent to a function in 2d to determine the local gradient, a plane is fitted to v_x and v_y , respectively, from which the gradient $\partial_\alpha v_\beta$ can be extracted.

For a given set of points $\{x_i, y_i, z_i\}_{i=1}^N$, A , B and C are determined so that the plane

$$z = Ax + By + C \quad (2.80)$$

minimizes

$$E(A, B, C) = \sum_{i=1}^N [(Ax_i + By_i + C) - z_i]^2. \quad (2.81)$$

Being a nonnegative, hyperparaboloid function, its minimum satisfies

$$\begin{pmatrix} 0 \\ 0 \\ 0 \end{pmatrix} = \nabla E(A, B, C) = 2 \sum_{i=1}^N [(Ax_i + By_i + C) - z_i] \begin{pmatrix} x_i \\ y_i \\ 1 \end{pmatrix}. \quad (2.82)$$

Note that the gradient is taken with respect to (A, B, C) and not (x, y, z) . The resulting system of three linear equations in A , B and C becomes

$$\begin{pmatrix} \sum_{i=1}^N x_i^2 & \sum_{i=1}^N x_i y_i & \sum_{i=1}^N x_i \\ \sum_{i=1}^N x_i y_i & \sum_{i=1}^N y_i^2 & \sum_{i=1}^N y_i \\ \sum_{i=1}^N x_i & \sum_{i=1}^N y_i & N \end{pmatrix} + \begin{pmatrix} A \\ B \\ C \end{pmatrix} = \begin{pmatrix} \sum_{i=1}^N x_i z_i \\ \sum_{i=1}^N y_i z_i \\ \sum_{i=1}^N z_i \end{pmatrix}. \quad (2.83)$$

To solve this system, a LU decomposition approach was chosen that is already implemented in the GNU Scientific Library [Galassi, 2009]. However, there is a large number of algorithms readily available in the standard literature for linear algebra that could be used instead.

Identifying z with v_x , the resulting A then corresponds to $\partial_x v_x$, while B corresponds to $\partial_y v_x$. Repeating the same method for v_y yields all partial derivatives and, therefore, the full velocity gradient tensor. The primary advantage of this approach lies in the freedom of choice of the set of points. For example, one can define a ring with the inner radius r_1 of the order of one cell size and the outer radius r_2 of the order of three cell sizes. Thus, the velocity gradient of the nearest neighbors can be calculated without considering the movement of the cell itself.

3 Results

3.1 Negative homeostatic pressure

In the original framework of homeostatic pressure theory as outlined in section 1.4.1, a uniform growth rate was assumed. However, experiments have shown that growth of tissues are highly dominated by surface effects (see section 1.4.2), which means the homeostatic pressure of a tissue in bulk differs considerably from the one measured with a finite surface to volume ratio. We will, thus, refer to this homeostatic pressure in the bulk simply as the *homeostatic pressure* in the remainder of this thesis. It has not been measured experimentally yet but the first attempts of extrapolation suggested that it might actually be negative [Montel et al., 2012].

In this section, we explore the possibility and the consequences of tissue growth with a negative homeostatic pressure. Starting from a theoretical point of view, we use our simulation model to directly evaluate the homeostatic pressure. Its dependence on different model parameters and its connection to the steady state size is elucidated. Subsequently, we analyze the growth behavior of tissues under mechanical stress and compare our results to the experimental data of several different cell lines. Finally, we estimate the homeostatic pressure of these cell lines by a linear extrapolation and a direct fit to the simulation data. Furthermore, we compare the results of 3d and quasi 1d systems and identify an interesting new state: tensile membranes. Most of the results presented here have already been published in [Podewitz et al., 2015].

3.1.1 Homeostatic pressure dependence on model parameters

The concept of a negative homeostatic pressure is best understood by a simple *gedankenexperiment*, similar to the one given in the introduction. Consider the growth of a tissue inside a box with sticky walls and a movable (and sticky) piston, connected to a spring (see figure 3.1). Cells are seeded at the bottom and start to grow until the compartment

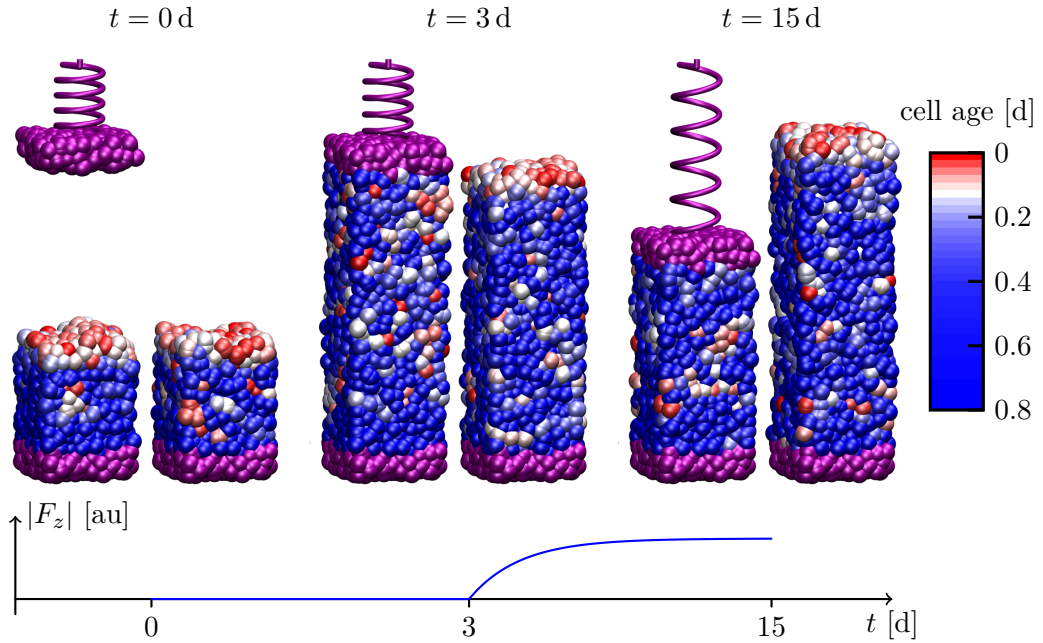


Figure 3.1: Visualization of a negative homeostatic pressure. Snapshots of cell growth in a box with a sticky surface at the bottom and with (left) and without (right) sticky piston at the top. Both layers (purple) consist of cells fixed by a strong harmonic potential. These cells cannot divide nor die but otherwise behave like normal cells. The piston is movable and only fixed by a weak harmonic potential depicted by the spring. Cells are color coded according to their age (red corresponds to recently divided cells, while blue cells did not divide for a certain amount of time). The force exerted by the spring is sketched below. Note that initially both set-ups show cell divisions to take place mostly near the free surface. This free surface is lost in the left set-up, when the tissue attaches to the sticky piston. Redrawn from [Podewitz et al., 2015].

is filled. Upon reaching the piston, however, the free surface is lost due to the adhesion between the cells and the piston, leaving only the on average apoptotic bulk. The overall number of cells decrease and due to the adhesion, the piston is pulled down, stretching the spring. The resulting tension increases the division rate in the bulk until a new stable steady state under tension is reached. Without the piston, another steady state emerges, where the apoptotic core is balanced by a continuous influx of cells from the proliferating surface.

Intuitively, one could think that this steady state under tension is unstable as a cut would release the tension. However, performing a virtual laser cut in the same system as above shows another behavior. The cut leads to a certain recoil but also creates a new free

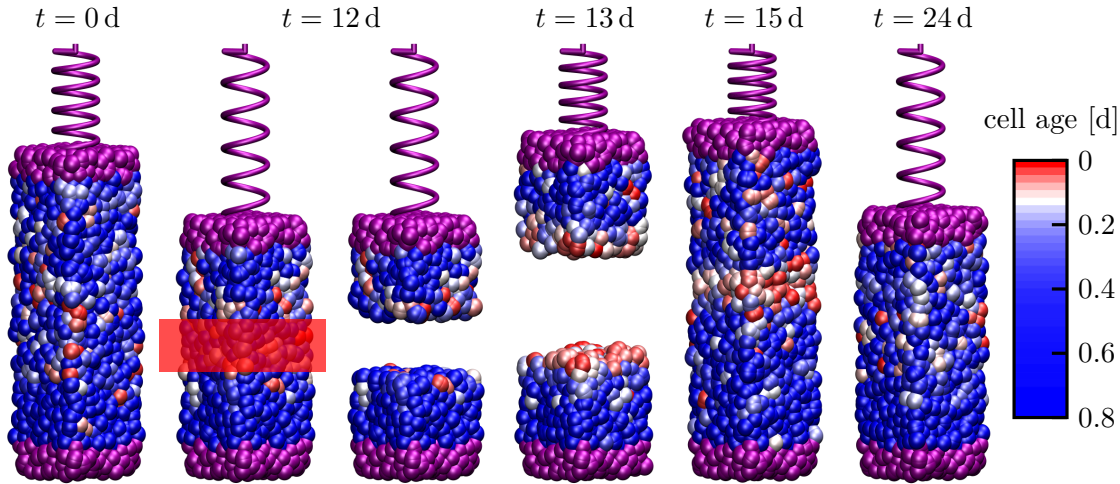


Figure 3.2: Virtual 3d laser cut experiment. Snapshots of cell growth in a box with a sticky surface at the bottom and a sticky piston at the top. Both layers (purple) consist of cells fixed by a strong harmonic potential. These cells cannot divide nor die but otherwise behave like normal cells. The piston is movable and only fixed by a weak harmonic potential depicted by the spring. Cells are color coded according to their age (red corresponds to recently divided cells, while blue cells did not divide for a certain amount of time). The tissue grows, fills the compartment and pulls down the piston, until a steady state under tension is reached. Upon laser exposure (visualized by the red box), cells are taken out of the simulation and the piston relaxes back to its equilibrium position. The free surface increases the growth rate of the tissue until the wound is closed and the same steady state under tension emerges again. Redrawn from [Podewitz et al., 2015].

surface. At this surface, the division rate increases and the tissue starts to grow until the wound is closed. Eventually the same steady state under tension is established as before (see figure 3.2).

To study the dependence of the homeostatic pressure on different model parameters, we used PBCs and measured the stress directly via the virial (see section 2.1.9). We varied the growth force strength B^* , the adhesion strength f_1^* , the compressibility K^* and the apoptosis rate k_a^* , around their standard parameter values. We chose these quantities since they have straight forward analoga in real tissues and can, in principle, be measured experimentally [Gavrieli, 1992, Gonzalez-Rodriguez et al., 2013, Lekka et al., 1999, Minc et al., 2009].

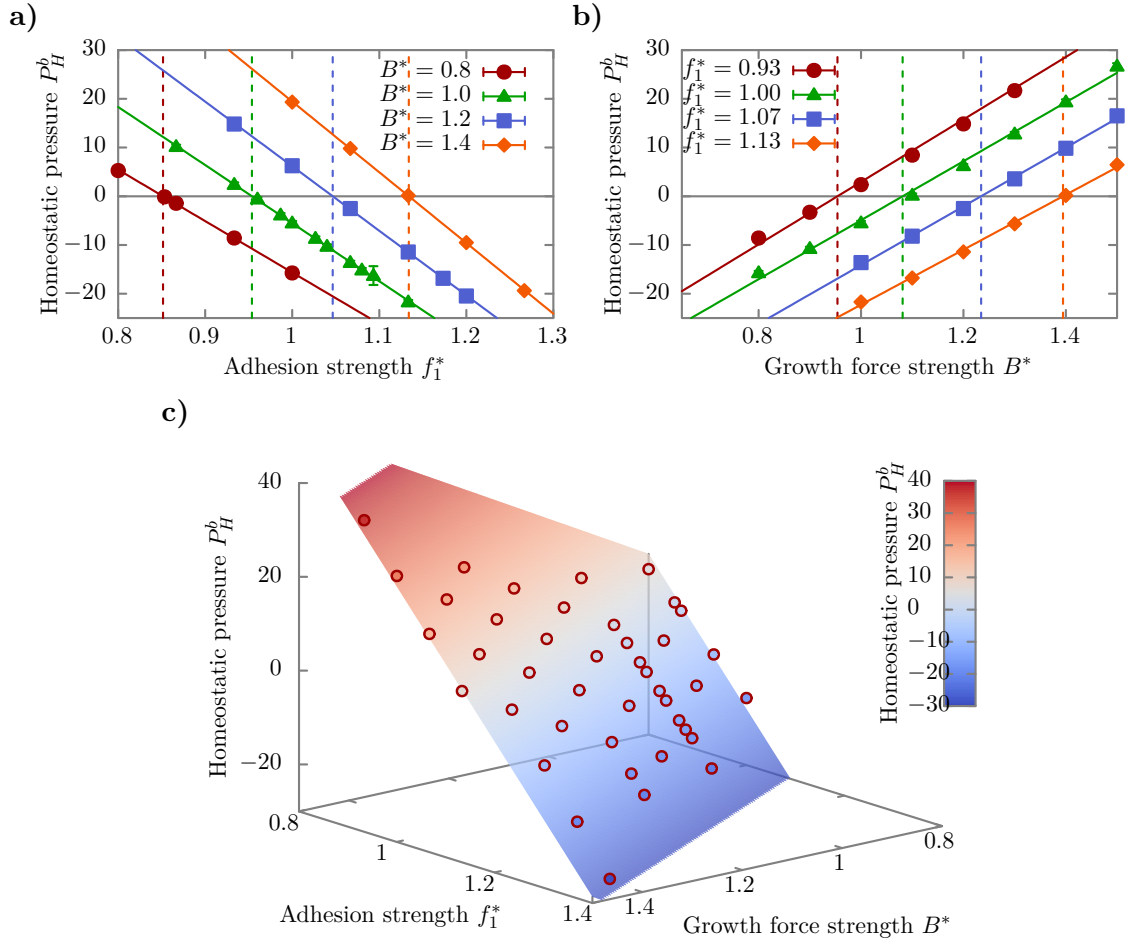


Figure 3.3: Homeostatic pressure dependence on growth force and adhesion strength. **a)** Homeostatic pressure P_H^b as a function of adhesion strength f_1^* for different growth forces B^* . Solid lines represent linear fits and dashed lines correspond to critical adhesion strength f_c^* , where P_H^b changes sign. Redrawn from [Podewitz et al., 2015]. **b)** Homeostatic pressure P_H^b as a function of growth force B^* for different adhesion strengths f_1^* . Solid lines represent linear fits and dashed lines correspond to critical growth force B_c^* , where P_H^b changes sign. **c)** 3d plot of the data of **a)** and **b)**. All points (red circles) are color coded inside according to their P_H^b . The plane is a fit of $P_H^b(f_1^*, B^*) = a_0 + a_1 B^* + a_2 f_1^*$ and also color coded in the same way. All error bars are SD.

Adhesion and Growth force

We observe that the homeostatic pressure is linear in the adhesion strength as well as the growth force strength (see figure 3.3a,b). Expanding P_H^b in B^* and f_1^* around 1 up to terms of linear order yields

$$P_H^b(B^*, f_1^*) = a_0 + a_1(B^* - 1) + a_2(f_1^* - 1). \quad (3.1)$$

A fit of this function to the simulation data shows a good agreement (see figure 3.3c) and results in the coefficients $a_0 = -5.89$, $a_1 = 60.65$ and $a_2 = -132.74$ with a reduced sum of squared residuals $\chi_{red}^2 = 1.8$ (for details on the plane fitting procedure see section 2.2.6).

Apoptosis rate

Surprisingly, the homeostatic pressure is mostly independent of the apoptosis rate over a wide range as shown in figure 3.4a. The only significant changes in P_H^b occur for very high apoptosis rates and only for those growth forces with a mostly positive P_H^b . While we would expect an overall decrease in the homeostatic pressure with increasing k_a^* , all curves seem to share a plateau or local minimum that roughly resides between 0.1 and 1. This indicates the more complex dependence of the homeostatic pressure on the apoptosis rate.

Compressibility

In the simulations, compressibility is equivalent to $1/f_0^*$, the inverse volume exclusion prefactor, if the ratio f_1^*/f_0^* with the adhesion strength f_1^* is kept constant. Thus, the equilibrium length stays the same, while the potential shape changes. The tissue gets less compressible for a steeper potential and more compressible for a more shallow potential. Hence, defining $K^* = 1/f_0^*$ gives a measure for the compressibility. Note, however, that K^* is not the real compressibility of our tissue. We observe that the homeostatic pressure increases with the compressibility (see figure 3.4b), meaning a softer tissue has a *higher* bulk homeostatic pressure. As a consequence, in the competition of two tissues that are identical except for their compressibility, the softer one would win against the more rigid one.

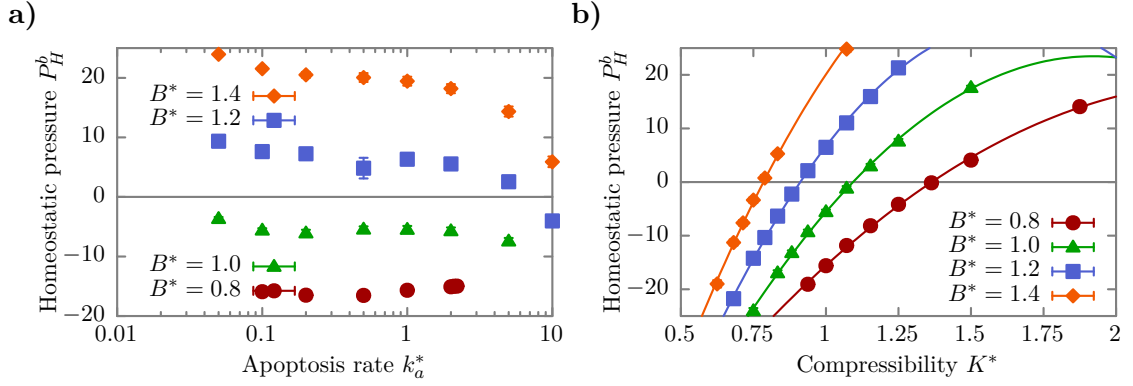


Figure 3.4: Homeostatic pressure dependence on different model parameters.

a) Homeostatic pressure P_H^b as a function of apoptosis rate k_a for different growth forces B^* . b) Homeostatic pressure P_H^b as a function of compressibility K^* for different growth forces B^* . Solid lines represent fits of $P_H^b(K^*) = a_0(K^* - K_0^*)^2 + a_1$. All error bars are SD. Redrawn from [Podewitz et al., 2015].

3.1.2 Spheroids

Figure 3.3 shows that for every given B^* there exists a critical value f_c^* (and B_c^* for any given f_1^*), which marks the transition between $P_H^b > 0$ and $P_H^b < 0$. Recalling the growth rate dependence k_b on the pressure P

$$k_b(P) = \kappa(P_H^b - P), \quad (3.2)$$

at $P = 0$, a negative homeostatic pressure requires a negative bulk growth rate, which, in turn, is necessary for a stable steady state, according to

$$\partial_t V = \frac{4}{3}\pi R^3 k_b + 4\pi R^2 \lambda \delta k_s. \quad (3.3)$$

On the other hand, a positive homeostatic pressure requires a positive bulk growth rate (at $P = 0$) and, therefore, f_c^* and B_c^* characterize the transition between steady state and infinite growth.

In the following, we want to check the dependence of the steady state size on the homeostatic pressure P_H^b and the adhesion strength f_1^* . Plugging equation (3.1), the linear

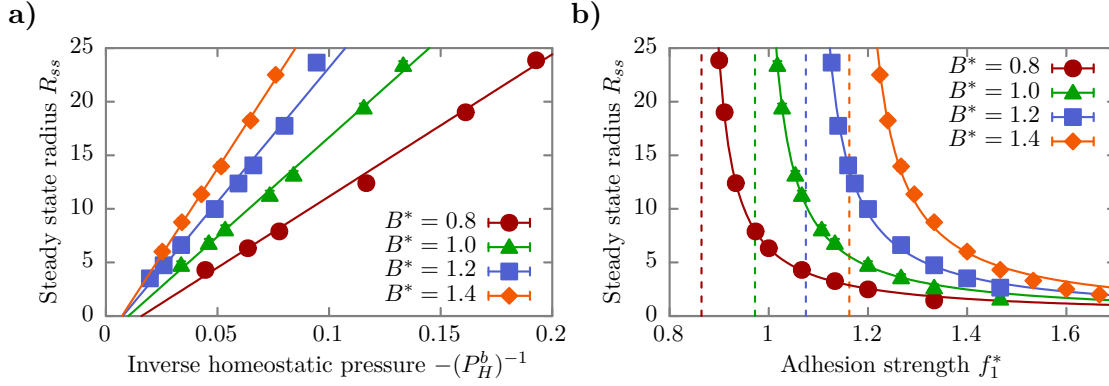


Figure 3.5: Steady state radius as a function of adhesion strength and inverse homeostatic pressure. a) Steady state radius R_{ss} as a function of the negative inverse homeostatic pressure $-1/P_H^b$ for different growth forces B^* . Solid lines represent linear fits. b) Steady state radius R_{ss} as a function of the adhesion strength f_1^* for different growth force strengths B^* . The solid lines represent fits of $R_{ss} = \alpha/(f_1^* - f_c^*)$, while the dashed lines correspond to the different critical adhesion strengths f_c^* , where R_{ss} diverges. All error bars represent the interface width ζ . Redrawn from [Podewitz et al., 2015].

expansion of P_H^b in B^* and f_1^* , into equation (2.47) (the steady state size R_{ss}), we get

$$R_{ss} = \frac{1}{a_0 + a_1(B^* - 1) + a_2(f_1^* - 1)} = \frac{a}{f_1^* - f_c^*}. \quad (3.4)$$

Thus, the steady state size should be inversely proportional to the adhesion strength for a given B^* . Indeed, the measurement of the steady state sizes R_{ss} for the same parameter range used above shows the expected $(P_H^b)^{-1}$ and $(f_1^* - f_c^*)^{-1}$ behavior (see figure 3.5a,b).

To measure the steady state size, we performed simulations of growing tissue spheroids with open boundaries (see figure 3.6a). The shown simulation snapshot also indicates the strong surface fluctuations, which makes the precise definition of a radius complicated. Averaging the density over time scales longer than these fluctuation times, however, results in a reproducible profile as shown in figure 3.6b. We observe a constant density in the bulk and a continuous drop at the front. We define the steady state radius R_{ss} as the

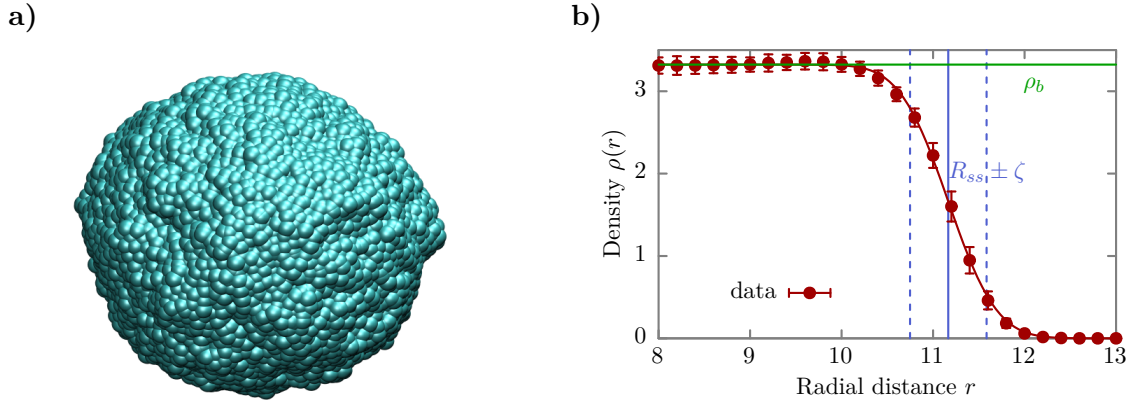


Figure 3.6: Snapshot of tissue spheroid in steady state and its radial density profile. **a)** Simulation snapshot of a tissue spheroid in steady state. Note that the actual shape deviates from a perfect spheroid. **b)** The averaged density profile ρ as a function of the radial distance to the center of mass r of a tissue spheroid in steady state. The solid red line represents a fit of an error function (see main text for details). The resulting parameters ρ_b , R_{ss} and ζ are shown. All error bars are SD.

inflection point of the density profile

$$\rho(r) = \frac{\rho_b}{2} \left[1 + \operatorname{erf} \left(\frac{R_{ss} - r}{\sqrt{2}\zeta} \right) \right], \quad (3.5)$$

where ρ_b is the bulk density and ζ is the interface width. Here, density has to be understood as an effective density, where the low values near the surface represent irregularities in the spheroid shape rather than an actual low local cell density. Using the above method results in a reproducible steady state radius R_{ss} .

3.1.3 Bulk growth rate dependence on pressure

As a next step, we want to study the bulk growth rate dependence k_b on imposed or externally applied mechanical stresses. For this purpose, we can either simulate tissues in a constant pressure ensemble (see section 2.1.7) or apply an external pressure through the addition of gas particles (see section 2.1.8). Both methods have their advantages and disadvantages. While the later is clearly much closer to actual experiments, it is computationally very expensive due to big system sizes and the additional gas particles

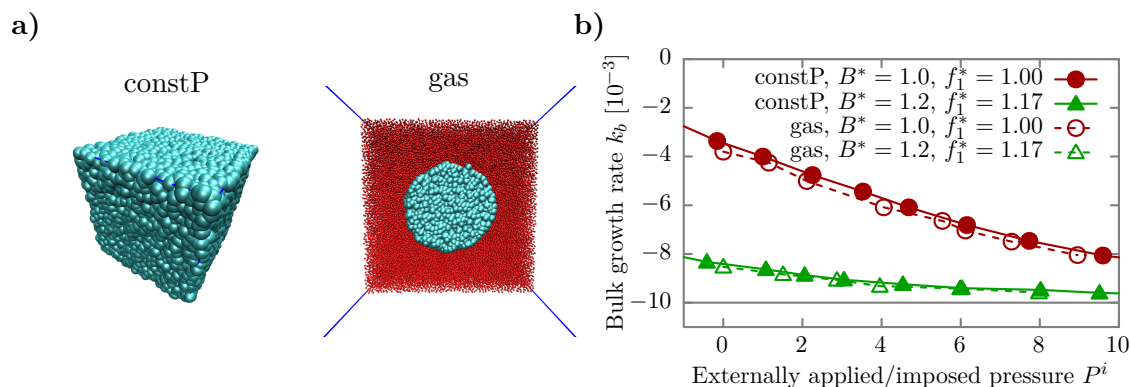


Figure 3.7: Comparison of constant pressure ensemble and gas particle method.

a) Simulation snapshots of constant pressure ensemble (constP) and gas particle method (gas). A more thorough description and larger version can be found in figure 2.6. **b)** Bulk growth rate k_b as a function of applied/imposed pressure P^i . Solid lines and closed symbols show constant pressure ensemble results, while dashed lines and open symbols result from gas particle method. Dotted gray line corresponds to the fixed apoptosis rate k_a . Redrawn from [Podewitz et al., 2015].

and can only exert compressional stresses onto the system. The former is obviously an artificial system but it has the merit of being computationally highly efficient, being applicable to virtually any system size, and most importantly, being able to simulate tissue behavior under tension, which, to our knowledge, no one has looked at experimentally so far. Although the constant pressure ensemble is our method of choice, we first want to verify that it gives consistent results, identical to the gas particle method. We picked two parameter sets to study with both techniques and compared the bulk growth rate k_b as a function of the imposed pressure P^i . Both methods give qualitatively and quantitatively the same growth rate dependence as shown in figure 3.7. Having demonstrated the equivalency, we will now focus on the constant pressure ensemble, due to its advantages mentioned above.

Starting from the standard parameter set, we measured the bulk growth rate dependence on pressure for varying growth and adhesion forces since these parameters systematically change the homeostatic pressure of the according tissue. All simulated parameter sets result in the same general behavior. Four exemplary data sets are shown in figure 3.8a. The observed similarity suggests that a proper rescaling should collapse all curves onto one. Indeed, considering the pressure difference between imposed P^i and homeostatic

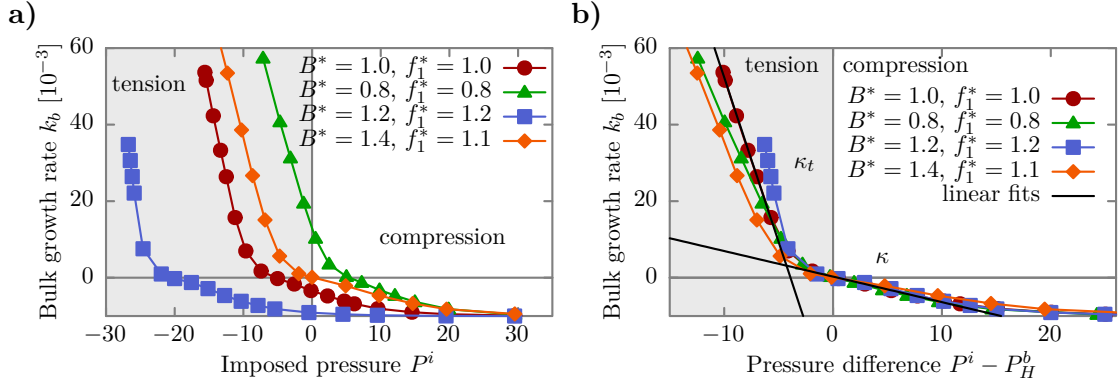


Figure 3.8: Bulk growth rate dependence on pressure for different growth forces and adhesion strengths. **a)** Bulk growth rate k_b as a function of the imposed pressure P^i for different growth force strengths B^* and adhesion strengths f_1^* . Only 4 exemplary data sets are shown since all sets display the same behavior. **b)** Same as in **a)** but as a function of the pressure difference between imposed and homeostatic pressure $P^i - P_H^b$. Redrawn from [Podewitz et al., 2015].

pressure P_H^b of the particular parameter set, reveals a general three regime picture (see figure 3.8b). In fact, a linear region with slope κ is observed that tends to bias towards effective compression as suggested by equation (1.2). Another linear regime with a different slope κ_t is seen in the domain of effective tension. For imposed pressures much larger than the homeostatic pressure, the bulk growth rate asymptotically approaches the constant apoptosis rate. The slopes κ are very similar, $\kappa = (-0.60 \pm 0.07) \cdot 10^{-3}$, while κ_t seems to change, $\kappa_t = (-8.0 \pm 1.9) \cdot 10^{-3}$, however, not statistically significant.

3.1.4 Negative homeostatic pressure in real tissues

So far, we have looked at the possibility of a negative homeostatic pressure and its dependence on different parameters only from a simulation point of view. To elucidate the question, whether a negative homeostatic pressure does exist in nature, we will now look at the published data [Delarue et al., 2014, Montel et al., 2011] of several different cell lines. One example experimental data set of the cell line CT26 is shown in figure 3.9 together with the simulation data of the standard parameter set. Note the roughly similar shapes.

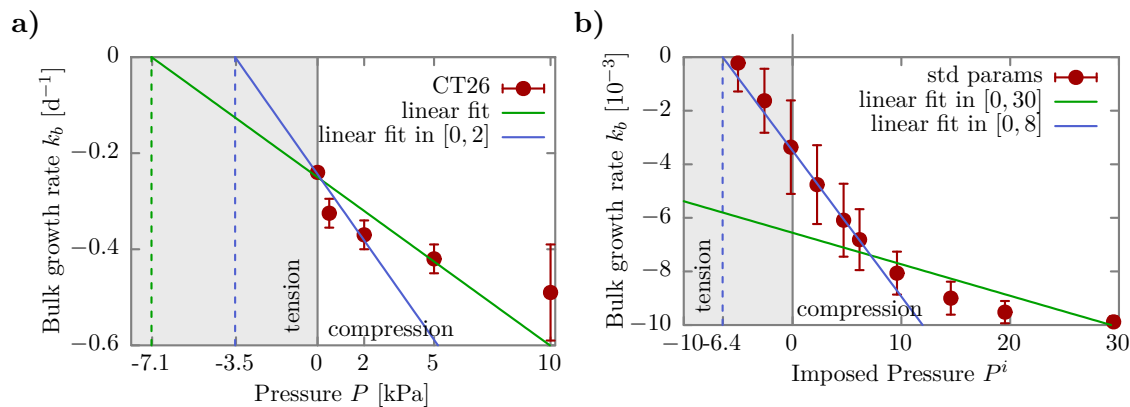


Figure 3.9: Bulk growth rate in experiments and simulations. a) Experimental data of the bulk growth rate k_b as a function of the applied pressure P for the CT26 cell line. Solid lines represent linear fits of all data (green) and in the interval $[0, 2]$ (blue). Error bars obtained from jackknife estimation. Data taken from [Montel et al., 2011]. b) Simulation data of the bulk growth rate k_b in simulations as a function of the imposed pressure P^i for the standard parameter set. Solid lines represent linear fits in the intervals $[0, 30]$ (green) and $[0, 8]$ (blue). The former estimation results in a homeostatic pressure of -60 ± 10 , while later results in -6.4 ± 0.3 . Error bars represent SD.

P_H^b from linear extrapolation

As a first test, we use equation (1.2), the linear expansion of the growth rate k_b around the homeostatic state, to estimate the homeostatic pressure for all five cell lines. Four out of five cell lines result in roughly the same order of magnitude of $P_H^b \sim -5$ kPa (see table 3.1). Figure 3.9, however, clearly shows that the dependence is not linear (either in

	$k_b(0 \text{ kPa}) [\text{d}^{-1}]$	$k_b(5/10 \text{ kPa}) [\text{d}^{-1}]$	$P_H^b [\text{kPa}]$
AB6	-0.02 ± 0.01	-0.04 ± 0.02	-5
BC52	-0.07 ± 0.01	-0.15 ± 0.01	-4.4
FHI	-0.59 ± 0.05	-1.08 ± 0.37	-6
CT26	-0.002 ± 0.0001	-0.13 ± 0.12	-7.1 ± 2.1
HT29	-0.24 ± 0.01	-0.42 ± 0.03	-0.16

Table 3.1: Experimental data of bulk growth rates under pressure and the linear extrapolated homeostatic pressure. Bulk growth rates k_b with and without externally applied pressure for five different cell lines. The k_b under pressure refers to $P = 10$ kPa in the case of HT29 and to $P = 5$ kPa for all others. Data taken from [De-larue et al., 2014, Montel et al., 2011].

t_{CT26}^{exp} [d]	t^{sim}	\hat{t} [d]	\hat{P} [kPa]
4.17	172.4	0.024	0.13

Table 3.2: Time and pressure scales for simulation data rescaling. The time scales are defined through the inverse bulk growth rate at zero pressure ($t_{CT26}^{exp} = 1/k_b^{CT26}(0)$ and $t^{sim} = 1/k_b^{sim}(0)$) and $\hat{t} \cdot t^{sim} = t_{CT26}^{exp}$.

the experiments nor in the simulations) and, furthermore, the outcome of the linear fits highly depend on the chosen interval, which can be seen in figure 3.9. We thus take the linear extrapolation as a lower boundary for the homeostatic pressure.

Rescaling units

In order to make a more quantitative comparison between simulations and experiments and to get a better estimation of the homeostatic pressure in the experiments, we first have to rescale the simulation data since their results are inherently without units (see section 2.1.6). An obvious choice for the time scale comes from the bulk growth rate at zero external pressure, which we know for experiments and simulations. To rescale the pressure, we would expect the homeostatic pressure to be a good choice but since it is unknown for the experimental data, we have to use another approach. Both, simulations and experiments seem to have a bulk growth rate dependence on pressure similar in shape (see figure 3.9). Therefore, we decided to fit our simulation data to the data of the CT26 cell line in order to get the best rescaling pressure \hat{P} . For each parameter set, we minimized the sum of squared residuals

$$\chi^2 = \sum_i \left[k_b^{CT26}(P_i) - k_b^{sim}(\hat{P} \cdot P_i) \right]^2. \quad (3.6)$$

We then varied the growth force strength B^* and the adhesion strength f_1^* . The resulting homeostatic pressures as a function of χ^2 are shown in figure 3.10a,b together with three exemplary fits of simulation data to CT26. A clear minimum can be seen that resides around a P_H^b of -1 to -2 kPa. However, we did not find one local minimum in the (B^*, f_1^*) parameter space but rather a valley of optimal combinations. That means for every given B^* , we can find a f_1^* with a low χ^2 and vice versa. Still, each of these optimal parameter sets result in roughly the same homeostatic pressure of -1 to -2 kPa (see figure 3.10c for a comprehensive comparison of χ^2 and P_H^b for different B^* and f_1^*). Picking the parameter

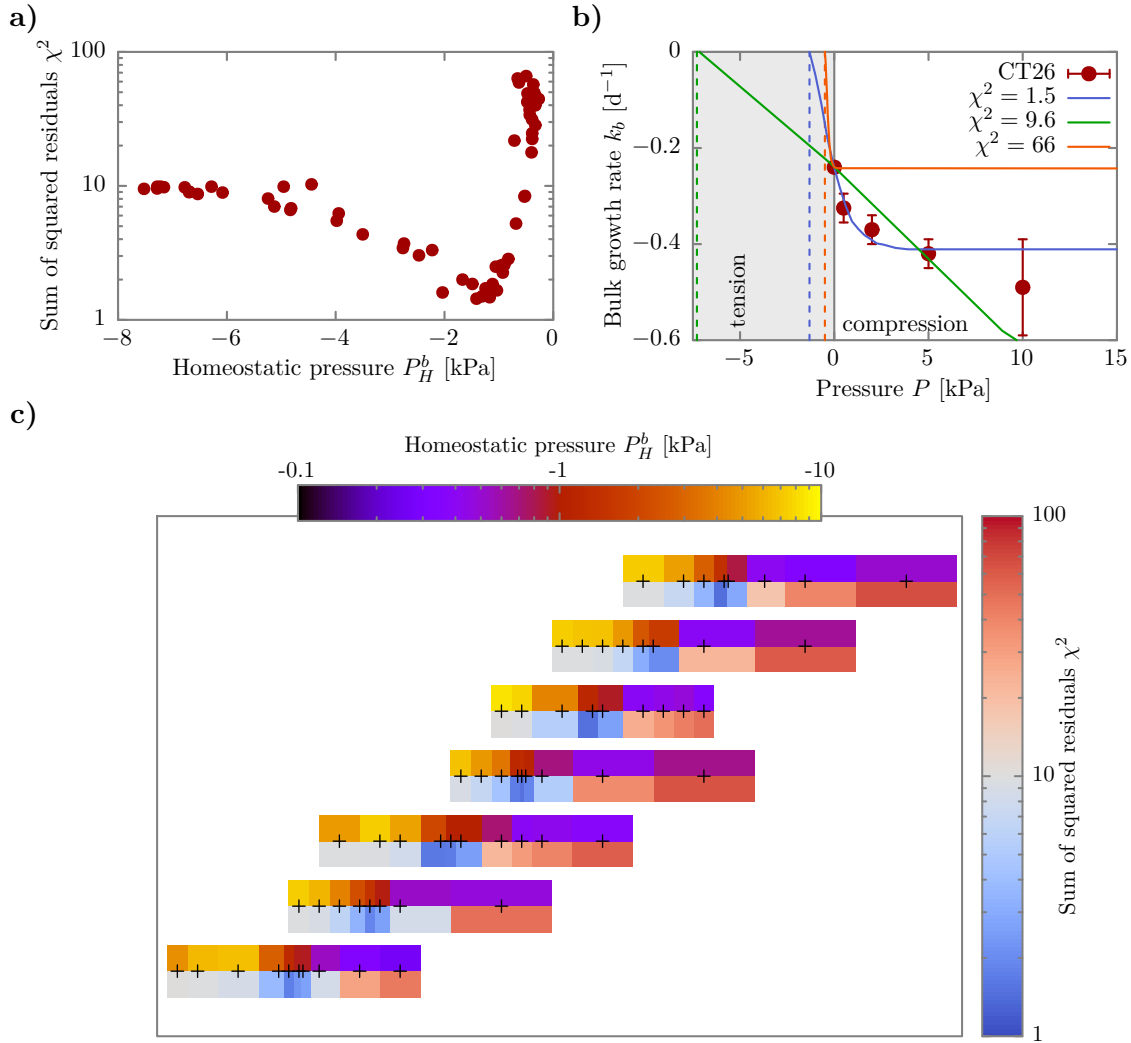


Figure 3.10: Results of simulation data fit to the data of CT26. a) The sum of squared residuals χ^2 as a function of the homeostatic pressure P_H^b . Note the logarithmic scale. b) Experimental data of CT26 with three simulation data sets rescaled according to their optimal \hat{P} . c) The sum of squared residuals χ^2 as a function of growth force B^* and adhesion strength f_1^* (heat map directly below black crosses with scale on the right) and the homeostatic pressure P_H^b as a function of the same parameters (heat map above black crosses with scale above plot). The black crosses mark the exact values for B^* and f_1^* used in the according simulations. Note that the low χ^2 (blue) always coincide with a P_H^b of -1 to -2 kPa (red/orange). Redrawn from [Podewitz et al., 2015].

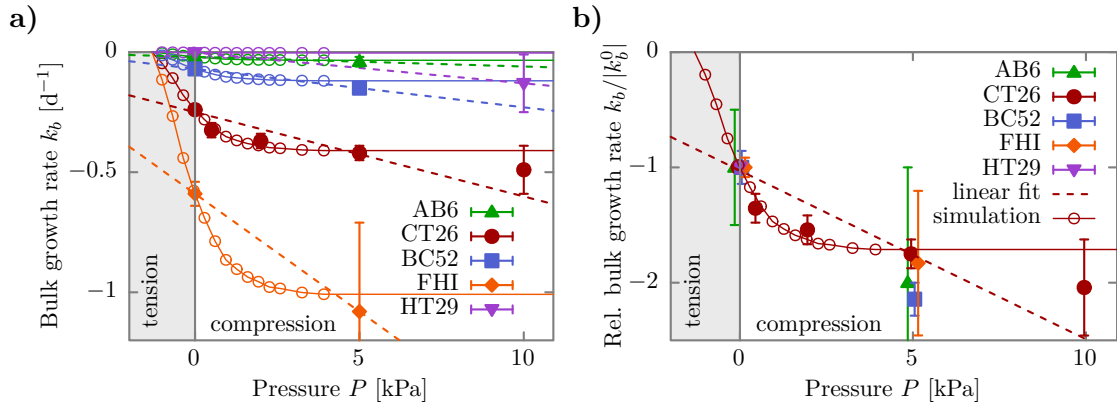


Figure 3.11: Bulk growth rate as a function of pressure for experiments and simulations. **a)** Bulk growth rate k_b for all five cell lines as a function of the applied pressure P (closed symbols). The simulation data of the best fit parameter set (open symbols and solid lines) is rescaled according to the bulk growth rate at zero pressure for each cell line. Dashed lines represent linear fits of the experimental data. **b)** Same as in **a)** but the bulk growth rate is rescaled by the modulus of the zero pressure bulk growth rate $|k_b^0|$. Solid line and open symbols correspond to best fit simulation data. Dashed line represents linear fit of CT26. Note, that the data point for HT29 under pressure is off scale (-65). Error bars obtained from jackknife estimation. Data taken from [Delarue et al., 2014, Montel et al., 2011]. Redrawn from [Podewitz et al., 2015].

set with the overall lowest sum of squared residuals $\chi^2 = 1.5$ ($B^* = 1.1$ and $f_1^* = 1.08$) yields a pressure rescaling factor $\hat{P} = 0.13$ kPa (see table 3.2).

Comparison of experimental data to best fit simulations

Using the rescaling units, derived in the section above, we now compare the experimental data of all five cell lines to the results of the best fit parameter set. Therefore, we change the time scale of the simulation data so that the bulk growth rates at zero pressure match. Interestingly, the rescaling of this one simulation parameter set leads to a good prediction of the bulk growth rates under pressure for three of the remaining four cell lines with HT29 being the sole exception (see figure 3.11a). This suggests that the experimental data follows some general behavior. Indeed, we observe a nice collapse of four out of five cell lines if we rescale the bulk growth rate k_b with the zero pressure bulk growth rate k_b^0 as shown in figure 3.11b. Again, HT29 is the only exception. We could theorize that the shape of $k_b(P)$ is determined by the homeostatic pressure, emphasizing its fundamental importance. This is supported by the results of the linear extrapolation of P_H^b , which

was roughly the same for all cell lines, except HT29. Later supposedly has a much larger homeostatic pressure, close to zero. However, the fit of the simulation data to CT26 suggests that this cell lines homeostatic pressure and, therefore, also the one of all other cell lines except HT29 is roughly -1 to -2 kPa.

3.1.5 Tensile membranes

So far, we have only studied real 3d systems of growing tissues. Since these spheroids can have very large steady state sizes, we want to investigate the possibility of using a quasi 1d representation as approximation. Such a quasi 1d set-up has periodic boundaries in x and y direction and open boundaries in z direction (see figure 3.12a), where a system size $L_x = L_y \ll L_z$ is chosen. Assuming that the growth rates k_b and δk_s are the same, independent of the dimensions, equation (2.41) and equation (2.46) relate both steady state sizes by

$$R_{ss} = 3R_{ss}^{1d}. \quad (3.7)$$

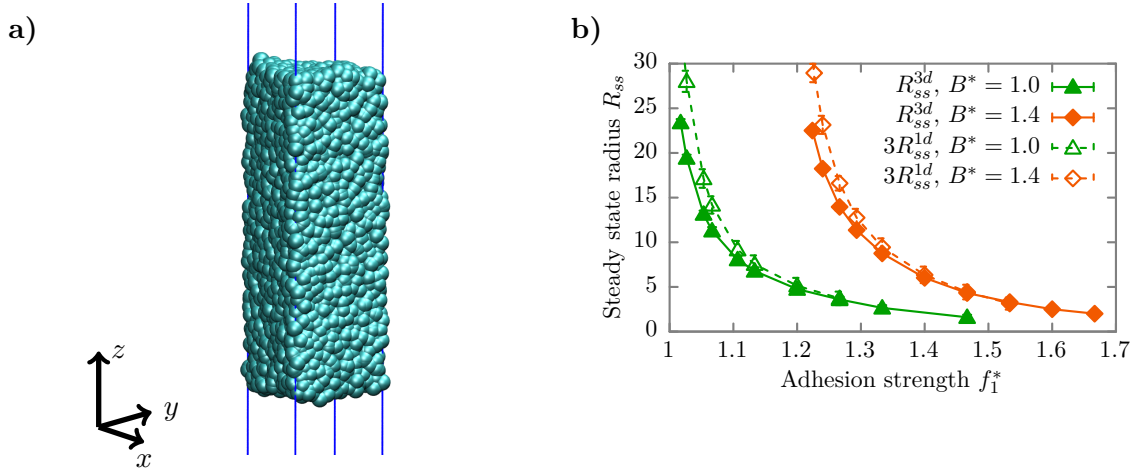


Figure 3.12: Steady state radius as a function of adhesion strength in 1d. a) Simulation snapshot of the quasi 1d set-up. b) Steady state radius R_{ss} as a function of the adhesion strength f_1^* for different growth force strengths B^* in 1d and 3d. The solid and dashed lines are simple guides for the eye, where solid lines and closed symbols correspond to 3d and open symbols with dashed lines correspond to 1d. Note the growing discrepancy for decreasing f_1^* . All error bars represent the interface width ζ .

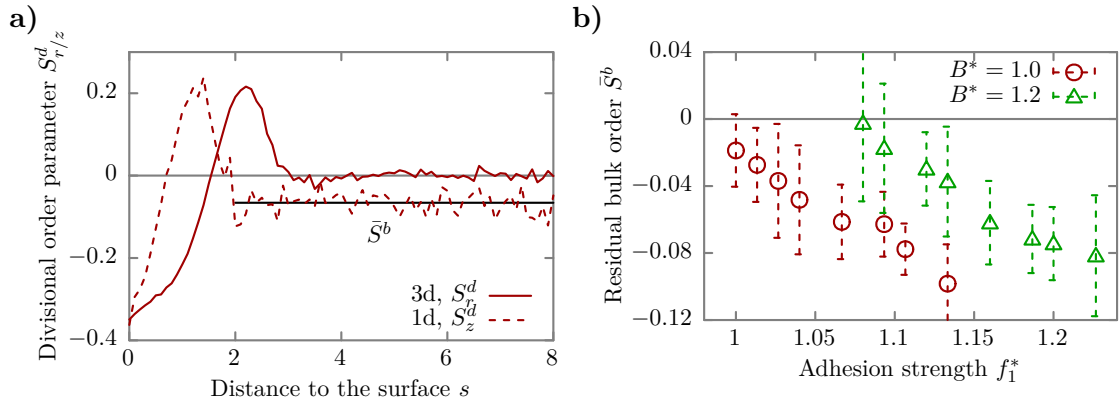


Figure 3.13: Residual bulk order. **a)** The order parameter of the cell division axis in 3d S_r^d and 1d S_z^d as a function of the distance to the surface s for $f_1^* = 1.07$. **b)** The residual bulk order \bar{S}^b as a function of the adhesion strength f_1^* . All error bars correspond to SD.

The results of such simulations, rescaled in the above manner, are shown in figure 3.12 and reveal a surprising discrepancy between 1d and 3d that increases with decreasing adhesion strength. In order to shed some light on the observed behavior, we looked at the cell division orientation in 1 and 3 dimensions as a function of the distance to the surface s . We calculated the order between the cell division axis \mathbf{d} and the radial unit vector \mathbf{e}_r for 3d and the order between \mathbf{d} and \mathbf{e}_z for 1d. The resulting order parameters (introduced in section 2.2.4) are called S_r^d and S_z^d for 3 and 1 dimensions, respectively. Both cases display the same behavior near the surface (see figure 3.13a), namely a transition between parallel and perpendicularly aligned divisions. However, the quasi 1d set-up shows divisions to be slightly aligned in the bulk, while the expected perfect anisotropy is observed in 3d. Having found an important difference between 1d and 3d simulations, we further investigated this residual bulk order \bar{S}^b as a function of varying adhesion strengths. We found the bulk order to rise with the adhesion as well as the growth force strength (see figure 3.13b). Considering our earlier results, a connection of this unexpected phenomenon to the homeostatic pressure suggests itself.

We now take a closer look at the periodic boundaries in the 1d set-up and how they might affect tissue growth. The method outlined in section 2.1.9, enables us to measure the full stress tensor as a function of space and time. We only consider systems in steady state and always silently apply adequate time averages to reduce the inherently strong fluctuations

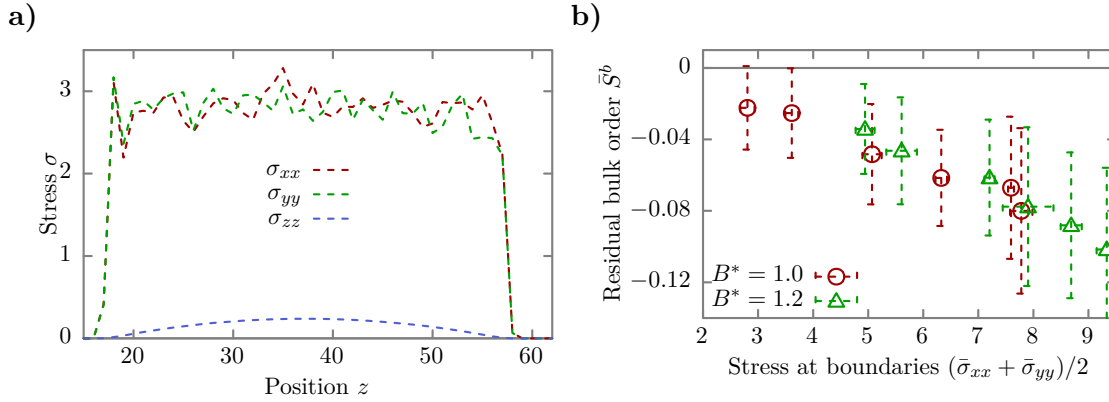


Figure 3.14: Stress and residual bulk order in the quasi 1d set-up. **a)** The stress $\sigma_{\alpha\alpha}$ as a function of position z . Both, σ_{xx} and σ_{yy} result in the same constant tension along z . Note the small non-zero contribution of σ_{zz} . **b)** The residual bulk order \bar{S}^b as a function of the average stress in x and y direction $(\bar{\sigma}_{xx} + \bar{\sigma}_{yy})/2$. In order to simulate different stresses at the boundaries, f_1^* is varied. All error bars correspond to SD.

of the stress tensor. While these strong fluctuations result in a SD much larger than the mean, long observation times yield a standard error of mean (SEM) that is practically zero. Therefore, no error bars are given whenever we consider the spatial distribution of stress. Still, the mean is reproducible and independent of the initial conditions for adequate time averages and, thus, clearly statistically significant.

Having measured the spatially resolved full stress tensor, we observe a constant tension σ_{xx} and σ_{yy} along z that drops to zero at the free surfaces (see figure 3.14a). This marks a fundamental difference of a real 1d system in comparison to the quasi 1d set-up. The negative homeostatic pressure of the used parameter sets create a constant tension across the periodic boundaries, thus, enhancing cell division in the according x - y plane. Residual bulk order should, therefore, grow with increasing stress. Indeed, we find a clear correlation between \bar{S}^b and $(\bar{\sigma}_{xx} + \bar{\sigma}_{yy})/2$ as seen in figure 3.14b, where $\bar{\sigma}_{xx}$ and $\bar{\sigma}_{yy}$ denote spatial averages over the bulk of the tissue. A better way to think of the quasi 1d simulation set-up is as a *tensile membrane*.

This tension leads to an increase in bulk division rate, which explains the discrepancy of the steady state radius between 3d and 1d as a higher bulk division rate results in a larger steady state radius. Remember that $R_{ss} \propto -1/k_b$ and k_b is negative.

So far, we have ignored the shape of σ_{zz} in figure 3.15a, which we now want to address.

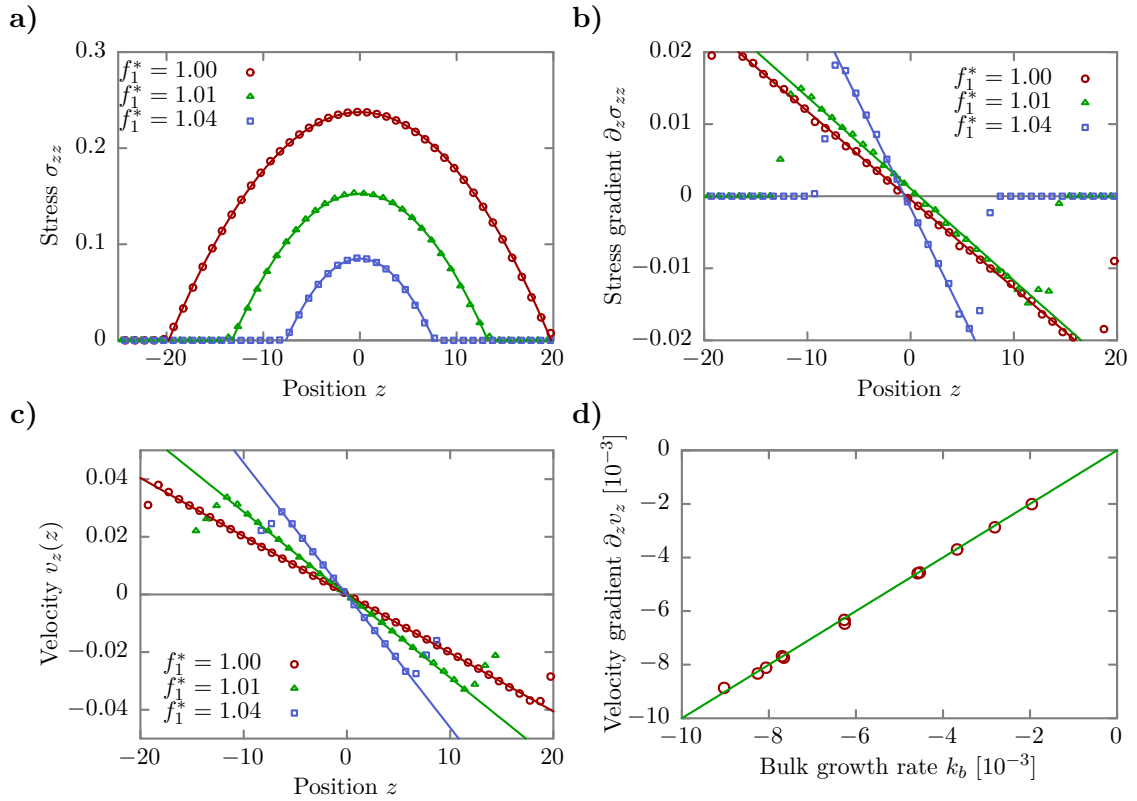


Figure 3.15: Stress and stress gradients in quasi 1d. **a)** The stress σ_{zz} as a function of position z shifted so that the minimum is at $z = 0$. Solid lines represent fits of $\sigma_{zz}(z) = a_0 z^2 + a_1$. **b)** The stress gradient $\partial_z \sigma_{zz}$ as a function of position z for the same parameters as in **a)**. Solid lines represent linear fits. **c)** The velocity profile v_z as a function of position z shifted by the same value as in **a)** and **b)**. Solid lines represent linear fits. **d)** Gradient of the velocity profile $\partial_z v_z$ as a function of the bulk growth rate k_b . The solid green line denotes the identity $\partial_z v_z = k_b$.

The observed profile is very smooth and resembles the form of a parabola. A direct fit of

$$\sigma_{zz}(z) = a_0(z - z_0)^2 + a_1 \quad (3.8)$$

reveals a perfect agreement as shown in figure 3.15a. To understand this behavior, we

have to consider momentum balance, which requires

$$\nabla \cdot \boldsymbol{\sigma} + \mathbf{f}^{ext} = \mathbf{v} [\partial_t \rho + \nabla \cdot (\rho \mathbf{v})] + \rho [\partial_t \mathbf{v} + (\mathbf{v} \cdot \nabla) \mathbf{v}] \quad (3.9)$$

$$\partial_z \sigma_{zz} + f_z^{ext} = 4\rho_b k_b v_z \quad (3.10)$$

with the stress σ_{zz} acting along z and the external force density f_z^{ext} . The only external force contribution in this kind of simulations comes from the background friction $\mathbf{F}^b = -\gamma_{bg} \mathbf{v}$ with $\gamma_{bg} = 0.1$. It follows that

$$\partial_z \sigma_{zz} = 2\rho_b \gamma_{bg} v_z(z) + 4\rho_b k_b v_z(z) = 2\rho_b v_z(z) \underbrace{(\gamma_{bg} + 2k_b)}_{=\gamma_{bg}^{eff}}, \quad (3.11)$$

where we substituted

$$f_z^{ext} = \frac{\sum_i F_i^b}{V} = \frac{2V \rho_b F^b}{V} \quad (3.12)$$

$$= -2\rho_b \gamma_{bg} v_z(z). \quad (3.13)$$

The factor of 2 is necessary because the background friction acts on each particle and there are 2 particles per cell. For a simple two rate growth model, the velocity profile is linear as shown in equation (2.49). Then, it follows that

$$\partial_z \sigma_{zz} = -2\rho_b \gamma_{bg}^{eff} k_b z \quad (3.14)$$

$$\sigma_{zz} = 2\rho_b \gamma_{bg}^{eff} k_b \int z dz \quad (3.15)$$

$$\sigma_{zz} = \rho_b \gamma_{bg}^{eff} k_b z^2 + A \quad (3.16)$$

and we can directly see, where the parabolic dependence of σ_{zz} on z comes from. To verify the validity of applying the two rate growth model, we measured the flow in our simulations and indeed observe a perfectly linear profile in the bulk (see figure 3.15c). Furthermore, the velocity gradient $\partial_z v_z$ matches the independently measured bulk growth rate k_b very well (see figure 3.15d). The background friction can then be estimated by a linear fit of $\partial_z \sigma_{zz}$ via equation (3.11), which results in $\bar{\gamma}_{bg} = (95.3 \pm 0.7) \cdot 10^{-3}$. This matches not exactly the input value of 0.1 but is reasonably close enough to paint a consistent picture.

While in 3d, the on average apoptotic core is balanced by a radial inflow of cells, this flow is different in 1d. There, cells flow only along one fixed axis, the z axis. Therefore, along x and y no cell flow balances cell death but instead the periodic boundaries create a constant pressure along x and y . For a negative P_H^b , this pressure is actually tensional and, thus, increases the division rate.

3.2 Interface dynamics of competing tissues

The outcome of a growth competition between two tissues in a finite compartment is determined by their homeostatic pressure as shown in section 1.4.1. The tissue with the higher homeostatic pressure always takes over the whole compartment. Recently, [Ranft et al. \[2014\]](#) have analyzed the population dynamics for the case of two incompressible tissues A and B by solving a generalized Fisher-Kolmogorov equation. They found traveling wave solutions, similar to those of the Fisher-Kolmogorov equation. In the later case, however, traveling waves can only emerge with non zero diffusion. Since we normally see little diffusion in our simulations, we want to explore in this section the possibility of tissue competition without diffusion ($D = 0$). Starting from a theoretical point of view, we first solve the dynamics for the one dimensional problem. Using the simulation set-ups outlined in section 2.1.12, we then study the interface dynamics in 2d and compare the results to the analytical solution in 1d. Furthermore, we analyze the scaling behavior of the emerging interface between the two competing tissues and determine their scaling exponents within our simulations.

3.2.1 Tissue competition without diffusion in 1d

To describe the competition between two tissues A and B, we define the cell number fraction

$$\varphi_A(\mathbf{x}, t) = \frac{n_A(\mathbf{x}, t)}{n_A(\mathbf{x}, t) + n_B(\mathbf{x}, t)}, \quad (3.17)$$

where $n_A(\mathbf{x}, t)$ refers to the number of A-type cells that occupy a small volume δV around \mathbf{x} at time t . The same quantities defined for tissue B result in

$$\varphi_B(\mathbf{x}, t) = \frac{n_B(\mathbf{x}, t)}{n_A(\mathbf{x}, t) + n_B(\mathbf{x}, t)} = 1 - \varphi_A(\mathbf{x}, t). \quad (3.18)$$

Assuming that the cells are incompressible and the cell densities are constant $\rho_A + \rho_B = \rho$, the cell number balance requires

$$\partial_t \varphi_{A/B} + \nabla \cdot \mathbf{J}_{A/B} = k^{A/B} \varphi_{A/B}, \quad (3.19)$$

where $k^{A/B}$ refer to the according growth rates of tissue A and B. The flow $\mathbf{J}_{A/B} = J_{A/B}^D + J_{A/B}^{ad}$ consists, in principle, of a diffusive part

$$\mathbf{J}_{A/B}^D = -D\nabla\varphi_{A/B} \quad (3.20)$$

with the diffusion coefficient D and a convective part

$$\mathbf{J}_{A/B}^{ad} = \mathbf{v}_{A/B}\varphi_{A/B} \quad (3.21)$$

with the velocity fields $\mathbf{v}_{A/B}$. Contrary to [Ranft et al. \[2014\]](#), we focus here on interface propagation without diffusion ($D = 0$) and, thus, we get

$$\partial_t\varphi_{A/B} + \varphi_{A/B}\nabla\cdot\mathbf{v}_{A/B} + \mathbf{v}_{A/B}\cdot\nabla\varphi_{A/B} = k^{A/B}\varphi_{A/B}. \quad (3.22)$$

The sum of both equations yields for $\varphi_B = 1 - \varphi_A$

$$\begin{aligned} \partial_t\varphi_A + \partial_t(1 - \varphi_A) + \varphi_A\nabla\cdot\mathbf{v}_A + (1 - \varphi_A)\nabla\cdot\mathbf{v}_B \\ + \mathbf{v}_A\cdot\nabla\varphi_A + \mathbf{v}_B\cdot\nabla(1 - \varphi_A) = k^A\varphi_A + k^B(1 - \varphi_A), \end{aligned} \quad (3.23)$$

which simplifies to

$$\nabla\cdot[\varphi_A(\mathbf{v}_A - \mathbf{v}_B)] + \nabla\cdot\mathbf{v}_B = k^A\varphi_A + k^B(1 - \varphi_A), \quad (3.24)$$

Assuming no relative flow between the tissues A and B ($\mathbf{v}_A = \mathbf{v}_B = \mathbf{v}$), this results in a generalized incompressibility condition

$$\nabla\cdot\mathbf{v} = k^A\varphi_A + k^B(1 - \varphi_A). \quad (3.25)$$

Combining equation (3.22) and equation (3.25), we can write the time evolution of the cell number fraction of A-type cells as

$$\partial_t\varphi_A + \mathbf{v}\cdot\nabla\varphi_A = (k^A - k^B)\varphi_A(1 - \varphi_A), \quad (3.26)$$

which is an advection-reaction type of equation and similar to a generalized version of the Fisher-Kolmogorov equation with zero diffusion. In 1d, it simplifies to

$$\partial_t \varphi_A + v \partial_x \varphi_A = (k^A - k^B) \varphi_A (1 - \varphi_A). \quad (3.27)$$

The transformation into a comoving reference frame by substituting $s = x - v_0 t$ results in

$$-v_0 \frac{d\varphi_A}{ds} + v \frac{d\varphi_A}{ds} = (k^A - k^B) \varphi_A (1 - \varphi_A) \quad (3.28)$$

$$\Rightarrow (v - v_0) \frac{d\varphi_A}{ds} = (k^A - k^B) \varphi_A (1 - \varphi_A). \quad (3.29)$$

This ordinary differential equation is solved by the following ansatz

$$\varphi_A(s) = \Theta(s) \quad (3.30)$$

if we assume

$$v(s = 0) = v_0. \quad (3.31)$$

$\Theta(s)$ refers to the Heaviside step function.

Stress profile

We already mentioned in the introduction that the division rates $k^{A/B}$ depend on the stress σ . Using the same linear expansion around the homeostatic state as before, the growth rates can be written as

$$k^{A/B} = -\kappa^{A/B} (\sigma_H^{A/B} - \sigma), \quad (3.32)$$

where $\kappa^{A/B}$ refer to the growth rate coefficients and $\sigma_H^{A/B}$ to the homeostatic stresses of the tissues A and B. We now want to solve for the stress profile $\sigma(s)$ using the results from above.

Due to the requirement of force balance, it follows that

$$\frac{d\sigma}{ds} = \xi v(s). \quad (3.33)$$

ξ refers to the background friction and is connected to γ_{bg} via

$$\xi = 2\rho\gamma_{bg}. \quad (3.34)$$

The factor of two is introduced here because ρ denotes the cell density but the background friction force is applied to all particles of a cell that is two. The velocity $v(s)$ is determined by the generalized incompressibility condition (equation (3.25)), which can be written in 1d for the comoving coordinate s

$$\frac{dv}{ds} = \varphi_A k^A + (1 - \varphi_A) k^B. \quad (3.35)$$

Combining equation (3.33) and equation (3.35), the stress profile can be written as

$$\frac{d^2\sigma}{ds^2} = \xi k^A \varphi_A + \xi k^B (1 - \varphi_A). \quad (3.36)$$

With the above solution for $\varphi(s)$ and the linear expansion of the growth rates around the homeostatic stresses, we get

$$\frac{d^2\sigma}{ds^2} = -\lambda_A^{-2} \Theta(s) (\sigma_H^A - \sigma) - \lambda_B^{-2} (1 - \Theta(s)) (\sigma_H^B - \sigma), \quad (3.37)$$

where

$$\lambda_{A/B}^2 = \frac{1}{\kappa^{A/B} \xi}. \quad (3.38)$$

For $s < 0$ it follows that

$$\frac{d^2\sigma}{ds^2} = -\lambda_B^{-2} (\sigma_H^B - \sigma) \quad (3.39)$$

$$\Rightarrow \sigma(s) = \sigma_H^B + A e^{-s/\lambda_B} + B e^{s/\lambda_B}. \quad (3.40)$$

Far away from the interface, the stress has to relax back to the homeostatic stresses of the tissues A and B. Thus, $\lim_{s \rightarrow -\infty} \sigma(s) = \sigma_H^B$ and A is zero. Similarly for $s > 0$ it follows

that

$$\frac{d^2\sigma}{ds^2} = -\lambda_A^{-2}(\sigma_H^A - \sigma) \quad (3.41)$$

$$\Rightarrow \sigma(s) = \sigma_H^A + A'e^{-s/\lambda_A} + B'e^{s/\lambda_A}. \quad (3.42)$$

As mentioned above, $\lim_{s \rightarrow \infty} \sigma(s) = \sigma_H^A$ and, thus, B' is zero. The continuity of σ and $d\sigma/ds$ at $s = 0$ requires

$$\sigma_H^B + B = \sigma_H^A + A' \quad (3.43)$$

and

$$\frac{B}{\lambda_A} = -\frac{A'}{\lambda_B} \quad (3.44)$$

so that

$$B = \frac{\sigma_H^A - \sigma_H^B}{1 + \frac{\lambda_A}{\lambda_B}} \quad (3.45)$$

$$A' = -\frac{\sigma_H^A - \sigma_H^B}{1 + \frac{\lambda_B}{\lambda_A}}. \quad (3.46)$$

Thus, the stress profile across the interface is described by

$$\sigma(s) = \begin{cases} \sigma_H^B + \frac{\sigma_H^A - \sigma_H^B}{1 + \frac{\lambda_A}{\lambda_B}} \exp\left(\frac{s}{\lambda_B}\right) & \text{for } s \leq 0 \\ \sigma_H^A + \frac{\sigma_H^B - \sigma_H^A}{1 + \frac{\lambda_B}{\lambda_A}} \exp\left(-\frac{s}{\lambda_A}\right) & \text{for } s > 0. \end{cases} \quad (3.47)$$

The stress across the interface varies exponentially from one homeostatic stress to the other although the interface itself is infinitesimally thin.

Interface velocity

Recalling equation (3.33), we can now calculate the interface velocity $v(0) = v_0$ with the analytical expression for the stress profile

$$v_0 = \frac{1}{\xi} \left. \frac{d\sigma}{ds} \right|_{s=0} = \frac{\sigma_H^A - \sigma_H^B}{\xi(\lambda_A + \lambda_B)}. \quad (3.48)$$

For $\kappa^A = \kappa^B = \kappa$, this simplifies to

$$v_0 = \frac{\sqrt{\kappa}}{2\sqrt{\xi}} (\sigma_H^A - \sigma_H^B). \quad (3.49)$$

The solution of the rather simple case of tissue competition in 1d without diffusion yields some interesting results. The volume fraction of each tissue can be described by a Heaviside step function in a comoving coordinate system. Contrary to a naive guess, we do get a moving interface with a velocity v_0 that grows linearly with the difference between the homeostatic stresses of the two competing tissues but only with $\sqrt{\kappa}$, the growth coefficient, and $1/\sqrt{\xi}$, the background friction.

In contrast to the example in section 1.4.1, here, the tissue with the higher homeostatic pressure does not impose its homeostatic pressure onto the whole system, which would lead to an exponential take-over. Instead, the background friction defines a characteristic length scale ($\lambda_{A/B}$) that results in a finite interface width between the two tissues, where the stress varies exponentially from one homeostatic stress to the other. Because of its finite width, the replacement of the “weaker” tissue takes place at a constant rate and, thus, leads to a constant interface velocity v_0 .

3.2.2 Interface position and width

We now want to define the position and the width of the interface between competing tissues in 2d simulations. Using the same naming convention as above, the cell number fraction $\varphi_{A/B}$ is described by

$$\varphi_{A/B} = \frac{n_{A/B}}{n_A + n_B} = \frac{n_{A/B}}{N}. \quad (3.50)$$

Here, $n_{A/B}$ refers to the number of cells of type A/B in a small strip of size $L\Delta x$ with $N = n_A + n_B$ being the total number of cells (see figure 3.16). Assuming an overall

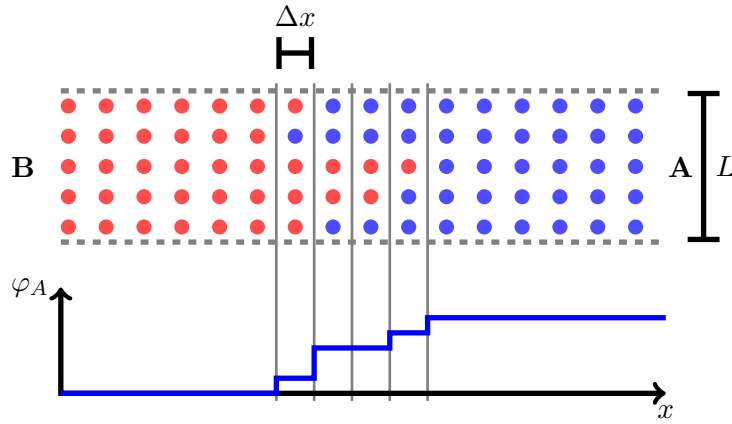


Figure 3.16: Sketch of the number fraction function φ . Small dots represent individual cells, where red correspond to tissue B and blue to tissue A.

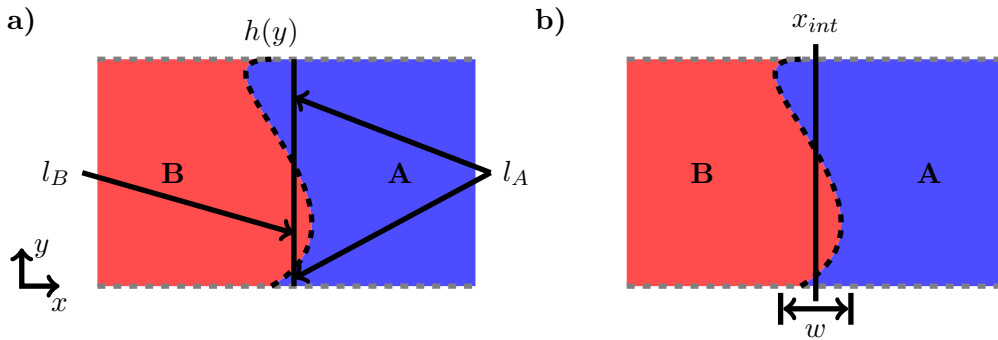


Figure 3.17: Sketch of the interface between two competing tissues A and B. a) The interface $h(y)$ between both tissues is depicted as a dashed black curve. For any given x , the occupation function φ is calculated from the line segments $l_{A/B}$ of a line that lie only in A or B. b) The according interface position x_{int} and interface width w are shown.

constant cell density ρ , the equation above can be written as

$$\varphi_A = \frac{n_A \rho^{-1}}{N \rho^{-1}} = \frac{l_A \Delta x}{L \Delta x} = \frac{l_A}{L} \tag{3.51}$$

with the channel width L in y direction. Considering now a cut along y for a given x , l_A then represents the length of the line that is occupied by A (see figure 3.17). Defining the

interface curve between A and B as $h(y)$, we can substitute l_A in equation (3.51) and get

$$\varphi_A(x) = \frac{1}{L_x} \int_0^{L_x} \Theta[h(y) - x] dx \quad (3.52)$$

$$\partial_x \varphi_A = \frac{1}{L_x} \int_0^{L_x} \partial_x \Theta[h(y) - x] dx \quad (3.53)$$

$$-\partial_x \varphi_A = \frac{1}{L_x} \int_0^{L_x} \delta[h(y) - x] dx \quad (3.54)$$

$$= p[h(y) = x] \quad (3.55)$$

with the probability density function $p[h(y) = x]$ for the interface height $h(y)$. The interface position, thus, reads

$$x_{int} = \langle x \rangle = \int_0^{L_x} xp(x) dx \quad (3.56)$$

$$= \int_0^{L_x} (-\partial_x \varphi_A) dx \quad (3.57)$$

$$= [-\varphi_A x]_0^{L_x} - \int_0^{L_x} (-\varphi_A) dx \quad (3.58)$$

$$= \int_0^{L_x} \varphi_A dx, \quad (3.59)$$

where we used the fact that $\varphi_A(L_x) = 0$. The second moment becomes

$$\langle x^2 \rangle = \int_0^{L_x} x^2 (-\partial_x \varphi_A) dx \quad (3.60)$$

$$= - \left[\varphi_A x^2 \right]_0^{L_x} + \int_0^{L_x} 2x \varphi_A dx \quad (3.61)$$

$$= 2 \int_0^{L_x} x \varphi_A dx \quad (3.62)$$

and we define the interface width w as

$$w = \sqrt{\langle x^2 \rangle - \langle x \rangle^2} = \sqrt{2 \int_0^{L_x} x \varphi_A dx - \left(\int_0^{L_x} \varphi_A dx \right)^2}. \quad (3.63)$$

3.2.3 Interface properties in theory and simulations

Treadmilling set-up

We implemented a set-up called *treadmilling* that uses a comoving simulation box to efficiently simulate tissue competitions. However, before we can use this method, we have to verify that it gives consistent results. Therefore, we compared this simulation technique to the fixed boundaries approach (see section 2.1.12 for detailed descriptions).

Both methods lead within less than 5% to the same size independent interface velocity v_0 (see figure 3.18a). The stress σ_{xx} across the interface averaged over $N \geq 8$ realizations does not show any systematic deviation between both methods (see figure 3.18b). For the remainder of this section, we only utilize the treadmilling set-up.

Tissue characterization

As before, we define standard parameter sets for the tissues A and B with the values presented in table A.1. The only differences are a lower cell adhesion of $f_1 = 5$, a higher background friction of $\gamma_{bg} = 10$ and for tissue B only, a higher growth force $B_B = 60$ and intracell friction $\gamma_c^B = 120$. In order to compare the simulation results with the analytical solution derived above, we first have to characterize the two involved tissues in terms of

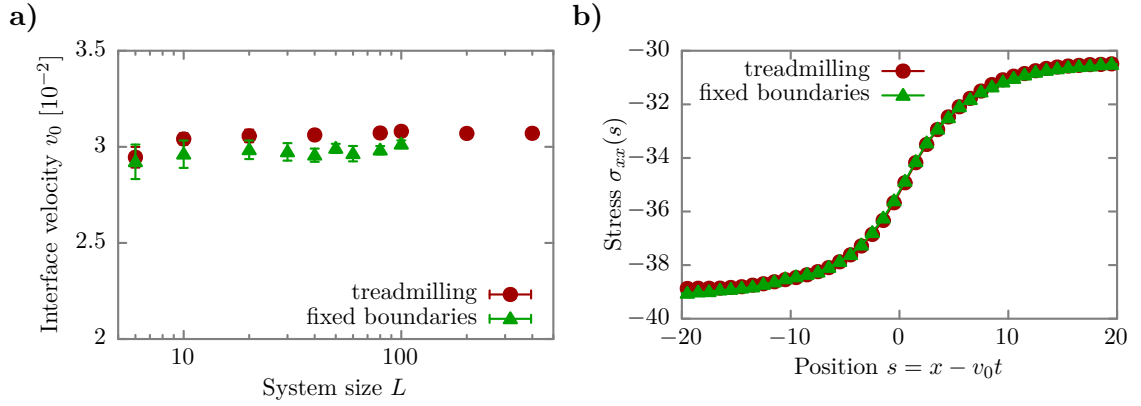


Figure 3.18: Comparison of treadmilling and fixed boundaries set-up. a) The interface velocity v_0 as a function of the system size L for treadmilling ($L_x = 140$) and fixed boundaries ($L_x = 160$) simulations for a homeostatic stress difference of $\Delta\sigma = 9$. Averages over $N \geq 8$ realizations per system size. Error bars represent SD. b) Stress σ_{xx} as a function of position s . Averages as in a) with $L = 10$.

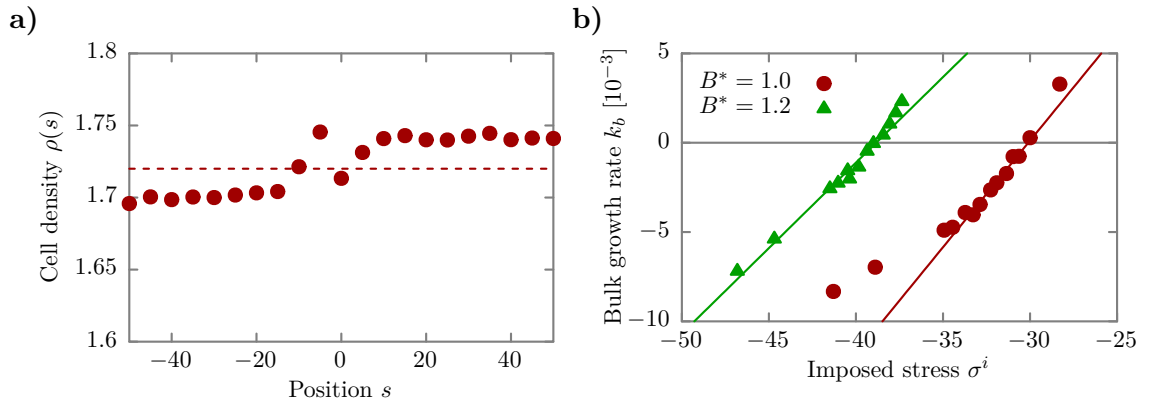


Figure 3.19: Tissue characterization. a) Overall cell density ρ as a function of position s averaged over $N = 8$ simulations. Dashed line corresponds to spatial average. Note that the difference in densities amounts to less than 3%. b) Bulk growth rate k_b as a function of the imposed stress σ^i . Solid lines represent linear fits around $k_b = 0$.

κ^A [10^{-3}]	κ^B [10^{-3}]	σ_H^A fit	σ_H^B fit	σ_H^A constP	σ_H^B constP
1.19 ± 0.07	0.96 ± 0.05	-30.1 ± 0.2	-38.8 ± 0.2	-30.4 ± 1.6	-39.2 ± 2.0

Table 3.3: Measured tissue properties. Growth rate coefficients $\kappa^{A/B}$ and homeostatic stresses $\sigma_H^{A/B}$ from linear fit of data (fit) and directly measured $\sigma_H^{A/B}$ (constP). The fit errors were determined by gnuplot. They represent a measure of the deviations from the linear fit and have to be taken with care. The errors of constP correspond to SD.

density ρ , growth force coefficients $\kappa^{A/B}$, and homeostatic stresses $\sigma_H^{A/B}$.

One of the main assumptions in the above derivation was a constant density of both tissues. In the simulations, we can easily measure the cell density as a function of position s (see figure 3.19a). Although a small variation can be seen, the difference amounts to less than 3%, which validates the assumption of equal densities.

We used the same methods as in section 3.1 to measure the homeostatic stress $\sigma_H^{A/B}$ and the bulk growth rate k_b as a function of the imposed stress σ^i . The growth rate coefficients $\kappa^{A/B}$ were extracted from a linear fit of $k_B(\sigma)$ around the homeostatic stress (see figure 3.19b). The homeostatic stresses derived from the linear extrapolation are consistent with the ones measured directly (see table 3.3). We observe that tissue B has a smaller growth rate coefficient κ . To explain this behavior, we have to recapitulate how we achieve the change in bulk homeostatic stress. In this case, we varied the growth force strength B^* and intracell friction γ_c , which leads to a smaller bulk homeostatic stress but also changes κ . It can be intuitively understood as a higher growth force makes the bulk growth rate less dependent on an external stress, thus, resulting in the smaller κ .

Using equation (3.34), ξ can be calculated from the background friction γ_{bg} and the average cell density $\bar{\rho}$. With $\gamma_{bg} = 10$ and $\bar{\rho} = 1.72$, $\xi = 2\bar{\rho}\gamma_{bg} = 34.42$. The factor 2 has to be added because the background friction acts on each particle and $\bar{\rho}$ represents the cell density. Thus, all free parameters of the analytical solution in 1d have been determined.

Interface velocity

We observe that the interface velocity v_0 scales linearly with the stress difference $\Delta\sigma = \sigma_H^A - \sigma_H^B$ for $\Delta\sigma < 30$ (see figure 3.20). Using equation (3.48) and the parameters determined above, we can estimate the slope of $v_0(\Delta\sigma) = \alpha\Delta\sigma$ to be $\alpha_{est} = 2.8 \cdot 10^{-3}$. A direct fit for $\Delta\sigma < 30$ reveals a reasonably good agreement with $\alpha_{fit} = 3.1 \cdot 10^{-3}$. However, larger differences in the homeostatic stresses display clear deviations from the linear trend,

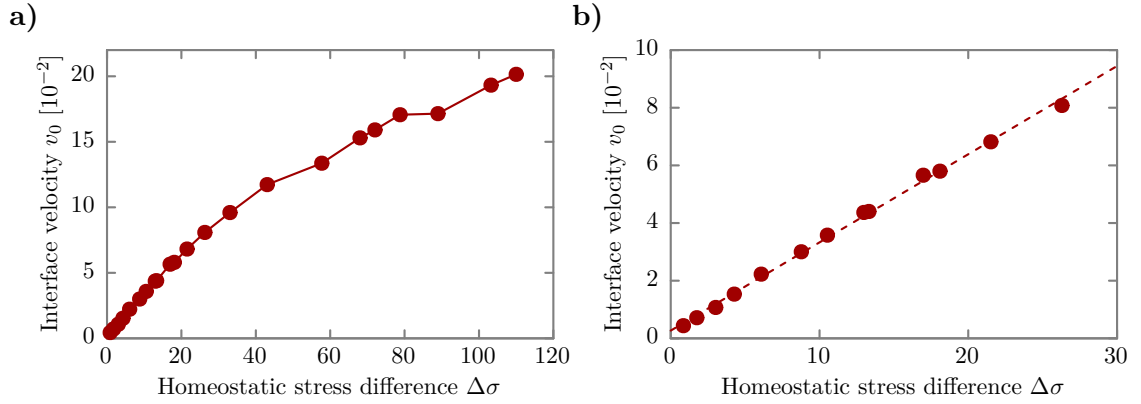


Figure 3.20: Interface velocity as a function of stress difference. **a)** The interface velocity v_0 as a function of the homeostatic stress difference $\Delta\sigma = \sigma_H^A - \sigma_H^B$ for a system size of $L = 10$. The solid line is a guide for the eye. **b)** Same as in **a)** but for a smaller range of $\Delta\sigma$. Dashed line represents a linear fit.

which reflects the nonlinearity in $k(\sigma)$.

Stress across interface

As a next step, we look at the stress across the interface and compare it to the 1d analytical solution. Consistently, the stress profiles $\sigma_{xx}(s)$ show a smooth transition from one bulk homeostatic stress to the other for different homeostatic stress differences $\Delta\sigma$ (see figure 3.21a). The anisotropy that is the stress difference of the stress parallel σ_{yy} and perpendicular σ_{xx} to the interface amplifies with increasing stress gradient (see figure 3.21b).

Using the measured tissue parameters, we can also compare the analytical solution of the stress profile in 1d to the actually measured stresses in the simulations. We observe a very good agreement between both profiles (see figure 3.22a). We can also verify the estimation of ξ by comparing $\sigma_{xx}(s)$ to the integrated velocity profile $\sigma_H^A + \xi \int v(x) dx$. Again, both curves coincide very well (see figure 3.22b).

3.2.4 Interface tension

As already noted in figure 3.21b, the stress is not isotropic across the interface. This leads to a surface or interface tension as defined in equation (2.71) (see section 2.2.5). No systematic dependence on the system size L is found for $L \geq 10$ (see figure 3.23a).

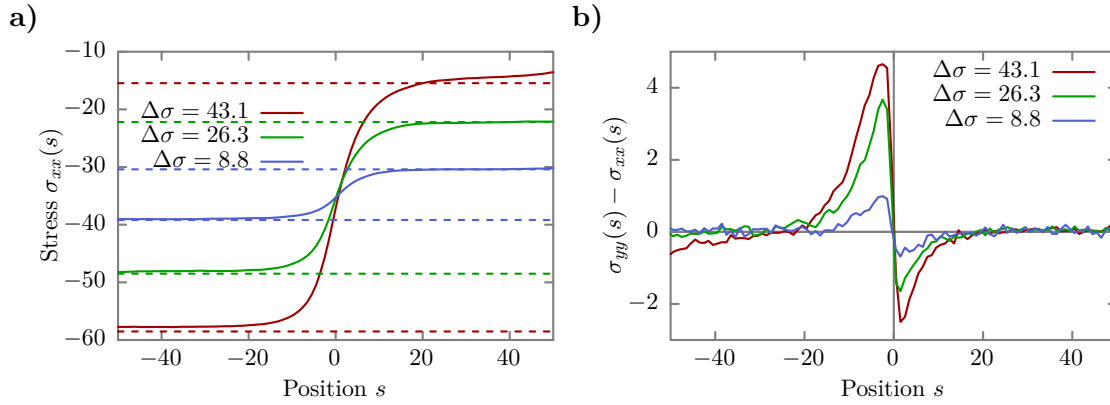


Figure 3.21: Spatial distribution of stress and stress anisotropy. a) Stress σ_{xx} as a function of s for different stress gradients $\Delta\sigma$. b) Stress anisotropy that is the difference between stresses parallel σ_{yy} and perpendicular σ_{xx} to the interface as a function of s for different stress gradients $\Delta\sigma$.

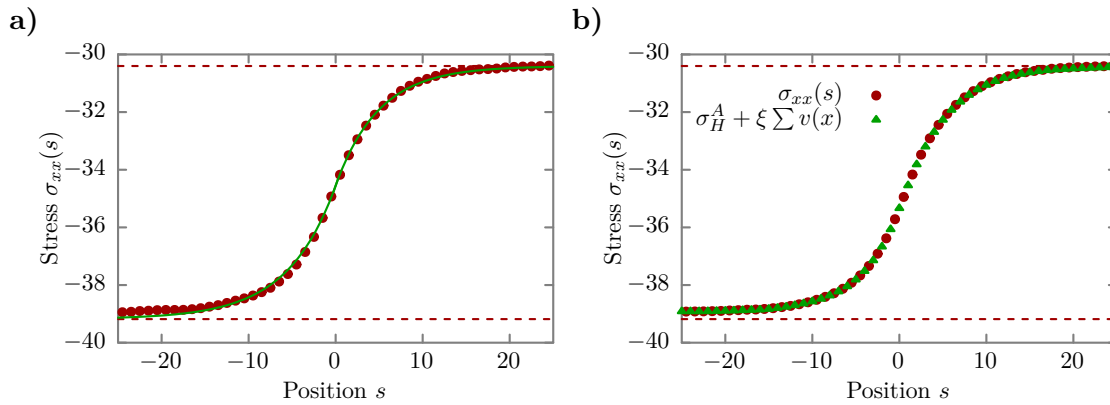


Figure 3.22: Comparison of 1d analytical solution and 2d simulation results. a) Stress σ_{xx} as a function of position s averaged over $N = 8$ simulations. Solid green line represent analytical solution. b) Stress profile $\sigma_{xx}(s)$ as in a) (red points) and the integrated velocity profile $\sigma_H^A + \xi \int v_x(s) dx$ (green triangles) averaged over $N = 8$ simulations.

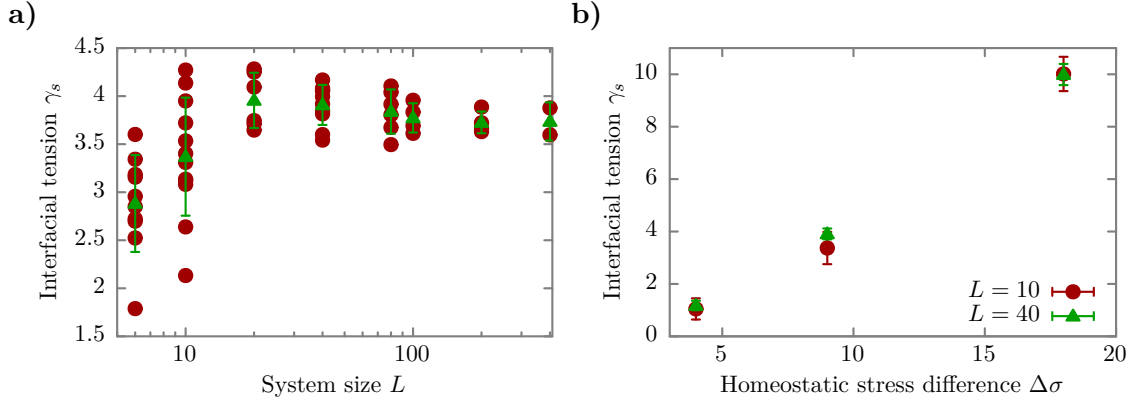


Figure 3.23: Interfacial tension. a) Interfacial tension γ_s as a function of the system size L for a homeostatic stress difference $\Delta\sigma = 9$. Closed red dots represent individual simulation results, while the green triangles denote mean plus minus SD of one system size. b) Interfacial tension γ_s as a function of the homeostatic stress difference $\Delta\sigma$ for two system sizes.

However, the interface tension increases significantly with a growing homeostatic stress difference $\Delta\sigma$ (see figure 3.23b).

3.2.5 Scaling behavior

Defining the interface width w according to equation (3.63), we can follow its evolution over time (see figure 3.24a). The initial interface width development $w(t)$ is well reproduced by a power law of the form

$$w(t) = At^\beta \quad (3.64)$$

(see figure 3.24b). We determined the growth exponents β for three different homeostatic stress differences $\Delta\sigma$ (see table 3.4). It seems to grow with increasing $\Delta\sigma$, however, this has to be taken with care. We varied the system size between $L = 6$ and $L = 400$ in the case of $\Delta\sigma = 9$, thus, covering nearly three orders of magnitude and between $L = 10$ and $L = 100$ in the case of $\Delta\sigma = 4$ and $\Delta\sigma = 18$. No systematic variation of β with L is found (see figure 3.24b). However, finite size effects for $L < 10$ lead to a systematic deviation.

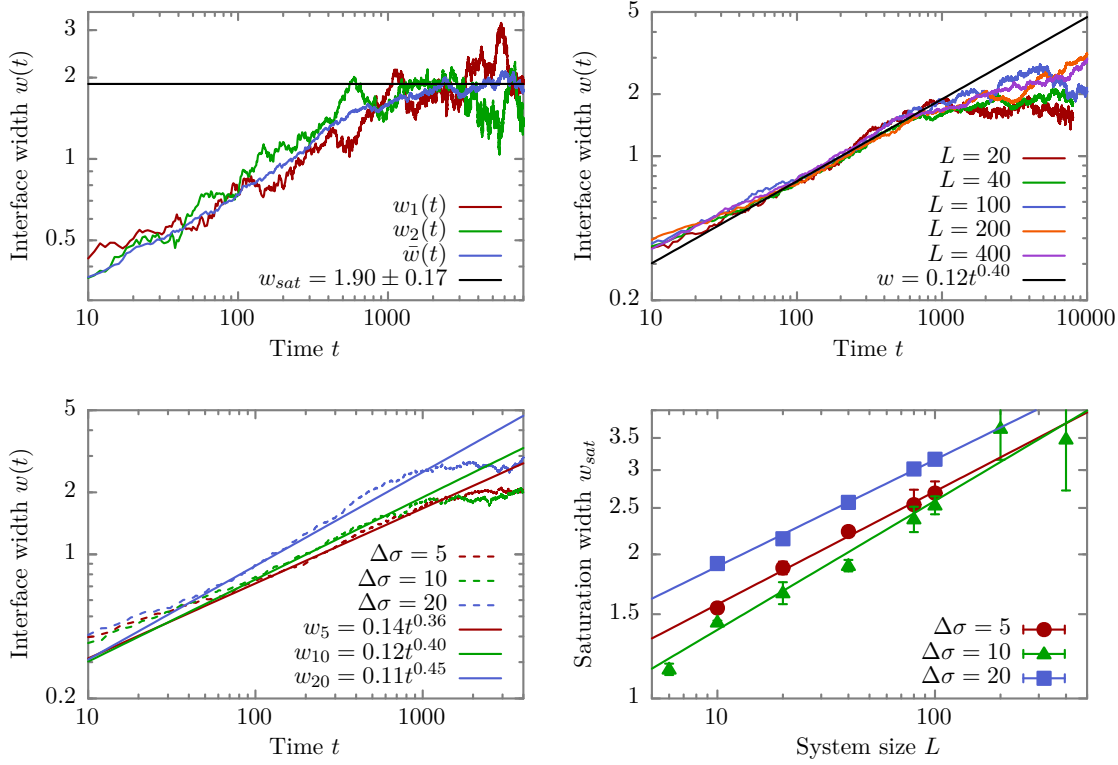


Figure 3.24: Interface width and saturation width as a function of time, system size and homeostatic stress difference. **a)** The interface width w as a function of time t . $w_1(t)$ and $w_2(t)$ show two individual realizations and $\bar{w}(t)$ the average over 10 independent simulations with $L = 40$ and $\Delta\sigma = 10$. The saturation width w_{sat} for $t \geq 2000$ is shown as black solid line. **b)** Same as in **a)** but as averages over several realizations for different system sizes L . Dashed black line corresponds to fit of early time evolution $w(t) = At^\beta$. **c)** Same as in **b)** but for one system size $L = 80$ and different homeostatic stress differences $\Delta\sigma$. Each dashed line is an average over $N \geq 6$ realizations. Solid lines represent fits of $w(t) = At^\beta$ averaged over all system sizes L for each homeostatic stress difference $\Delta\sigma$. Note the different growth exponents β . **d)** The saturation width w_{sat} for different homeostatic stress differences $\Delta\sigma$ as a function of the system size L . Solid lines represent linear fits of double logarithmic data. Error bars correspond to SEM.

$\Delta\sigma$	growth exponent β	roughness exponent α
5	0.36 ± 0.04	0.24 ± 0.01
10	0.40 ± 0.03	0.27 ± 0.03
20	0.45 ± 0.02	0.25 ± 0.01

Table 3.4: Results of the scaling analysis. Results of the fits of the early interface width development $w(t) = At^\beta$ and the saturation width as a function of the system size $w_{sat}(L) = BL^\alpha$. Coefficients and errors determined by according gnuplot fits.

We also analyzed the scaling behavior of the saturation width w_{sat} by fitting

$$w_{sat}(L) = BL^\alpha \tag{3.65}$$

to our data. No systematic variation of the roughness exponent α with the homeostatic stress difference $\Delta\sigma$ could be determined (see figure 3.24d and table 3.4). We found an average roughness exponent of $\bar{\alpha} \approx 0.25 \pm 0.01$. However, it has to be noted that the crossover time between power law growth and saturation regime increases with the homeostatic stress differences $\Delta\sigma$ and decreasing system size. Thus, for large systems and small $\Delta\sigma$, the measured saturation width may have much larger errors than estimated from the SEM.

As mentioned in the introduction, the two exponents α and β are commonly used to classify the interface growth process into different so called universality classes. One well known example is the Kardar–Parisi–Zhang (KPZ) universality class, which yields a growth exponent of $\beta_{KPZ}^{2d} = 1/3$ and a roughness exponent of $\alpha_{KPZ}^{2d} = 1/2$. It has been suggested that growing tissues fall into this class [Block et al., 2007]. While the growth exponent measured in our simulations roughly fits, the roughness exponent is much smaller in the simulations. More closely related to tissue growth, Vicsek et al. [1990] have measured the roughness exponent of initially flat interfaces of growing bacterial colonies. However, they found an even larger exponent of $\alpha \approx 0.78$. Thus, it has yet to be decided which general microscopic processes dominate the dynamics of competing tissues.

3.3 Division axes alignment in motile tissues

In this section, we want to study how cell division is influenced by directed cell movement in migrating cell sheets. We compare the results of our simulations, extended by the motility mechanism introduced in section 2.1.2, to experiments of Madin-Darby canine kidney (MDCK) cell sheets that invade narrow micro-channels. We greatly acknowledge Prof. Dr. Joachim Oskar Rädler, Dr. Anna-Kristina Marel and Matthias Zorn for conducting the experiments and providing us with the data. Most of the results presented here have already been published in [Marel et al., 2014].

3.3.1 Experimental and simulation Set-ups

Experiments

The experimental proceedings are described in full detail in [Marel et al., 2014, 2013]. In short, microstructures were created with the cell-repellent polymer poly(ethylene glycol)-dimethacrylate (PEG-DMA) from a negative replica polydimethylsiloxane (PDMS) mold that was put onto standard cell culture dishes (see figure 3.25). Cells were then seeded

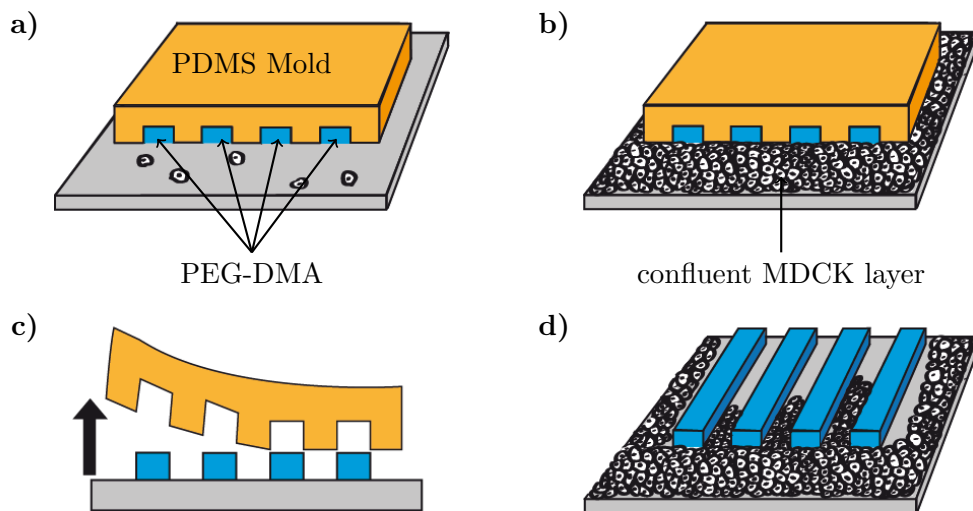


Figure 3.25: Sketch of the experimental procedure. a) Initially, PEG-DMA structures are covered with PDMS mold. b) Cells are seeded around the structure and grown to confluency. c) PDMS mold is peeled off and d) the cells start to invade the narrow channels. Redrawn from [Marel et al., 2014].

around the structures and grown until confluency. The removal of the PDMS stamp opened up the microstructures, in this case long narrow channels, and the cells started to invade the open space. During the course of an experiment, cell migration was tracked with time-lapse microscopy (brightfield and fluorescence, see figure 3.26a) at a framerate of 0.1 min^{-1} . Doubly transfected MDCK cells with a fluorescently labeled cell nucleus were used. Cell division events were determined visually from the fluorescent images and both daughter cells were marked, thus defining the position and the axis of each division. The fluorescent images were also used to determine the position of all cells in every frame. In order to differentiate effects stemming from the confinement as opposed to effects caused by global flow, experiments were conducted with *resting* cell sheets. In those experiments, cells were uniformly seeded over the whole microstructure *after* the removal of the PDMS stamp (see figure 3.28a). The velocity fields for both set-ups (*invading* and *resting* cell sheets) were determined by particle image velocimetry (PIV).

Simulations

In order to keep the invading cell sheet simulations as close as possible to the actual experiments, we implemented a complex chamber geometry that is depicted in figure 3.26b. It consists of a reservoir chamber at the bottom, which is connected to a narrow channel. The PEG-DMA channel structures are modeled with RBCs. Cells are seeded randomly over the reservoir with a constant density of $\rho = 2 \cdot 10^{-3} \mu\text{m}^{-2}$.

In the case of resting cell sheets, we used a simple rectangular box (again with RBCs), which was seeded randomly with the same constant cell density as before (see figure 3.28a).

3.3.2 Rescaling simulations

Simulation results are inherently without units (see section 2.1.6). In order to compare the simulations to experimental data, we have to define a length \hat{l} and a time scale \hat{t} , which convert simulation lengths/times (l^{sim}/t^{sim}) to experimental lengths/times (l^{exp}/t^{exp}) via

$$l^{exp} = \hat{l}^{sim} \quad (3.66)$$

$$t^{exp} = \hat{t}^{sim} \quad (3.67)$$

We decided to use the invasion speed v_f and the cell density ρ_b in the bulk of invading cell sheets. Being independent of the used channel width L_y in the experiments as well as the

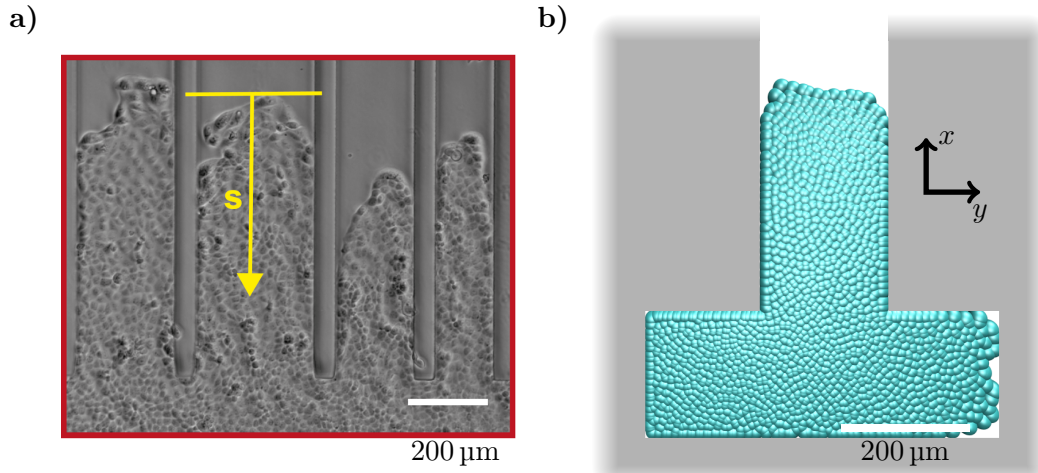


Figure 3.26: Set-up of experiments and simulations for invading cell sheets.

Set-up of **a)** experiments and **b)** simulations for invading cell sheets. The PEG-DMA confinement is modeled in the simulations by hard walls with RBCs. Redrawn from [Marel et al., 2014].

ρ^{exp} [$10^{-3}\mu\text{m}^{-2}$]	ρ^{sim}	v_f^{exp} [$\mu\text{m h}^{-1}$]	v_f^{sim}	\hat{l} [μm]	\hat{t} [h]
1.4	2.8	24	0.066	44.72	0.12

Table 3.5: Results of length and time scale comparison. Length and time scale used to relate the simulation data to experimental data.

simulations (see figure 3.27a), the invasion speed or front velocity determines the ratio

$$\frac{\hat{l}}{\hat{t}} = \frac{v_f^{exp}}{v_f^{sim}}. \quad (3.68)$$

Defining the bulk in the experiments at around $400\mu\text{m}$ behind the front, we matched this density to the simulations to get the rescaling length

$$\hat{l} = \sqrt{\frac{\rho_b^{sim}}{\rho_b^{exp}}}. \quad (3.69)$$

See figure 3.27 and table 3.5 for the extracted length and time scale.

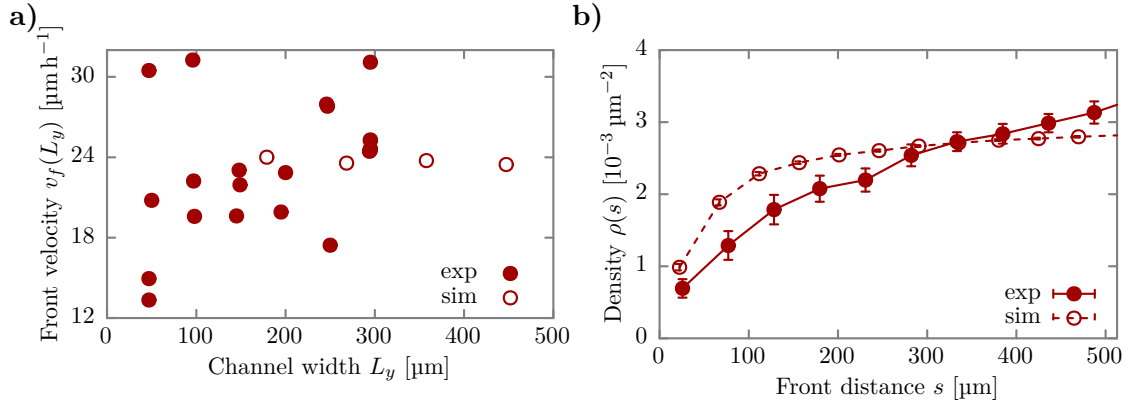


Figure 3.27: Front velocity and density profile in experiments and simulations. a) Front velocity v_f as a function of channel width L_y . b) Density ρ as a function of the distance to the front s . Error bars represent SEM. Taken from [Marel et al., 2014].

3.3.3 Resting cell sheets

In order to differentiate effects stemming from the boundaries, we first analyzed the experimental and simulation data of resting cell sheets.

Divisional order

The experiments of resting cell sheets show no preferred direction of the division axes roughly two to three cell diameters away from the wall (see figure 3.28b). However, the order parameter increases significantly towards the channel wall, showing nearly perfect alignment directly at the wall. This increase is best understood by entropical reasons. The site of a cell division is calculated as the midpoint of the connection between the two daughter cells. In the following, we will refer to this length of the connecting vector as the cell size l . A division that takes place at a distance $\delta y < l/2$ has only a certain range of orientations available because the daughter cells cannot penetrate the wall (see figure 3.28c). Using elementary geometry, the available minimal division angle θ_{min} between the wall and the division axis can be expressed as a function of δy and l :

$$\theta_{min}(\delta y, l) = \arcsin\left(\frac{2(\delta y - y_0)}{l}\right). \quad (3.70)$$

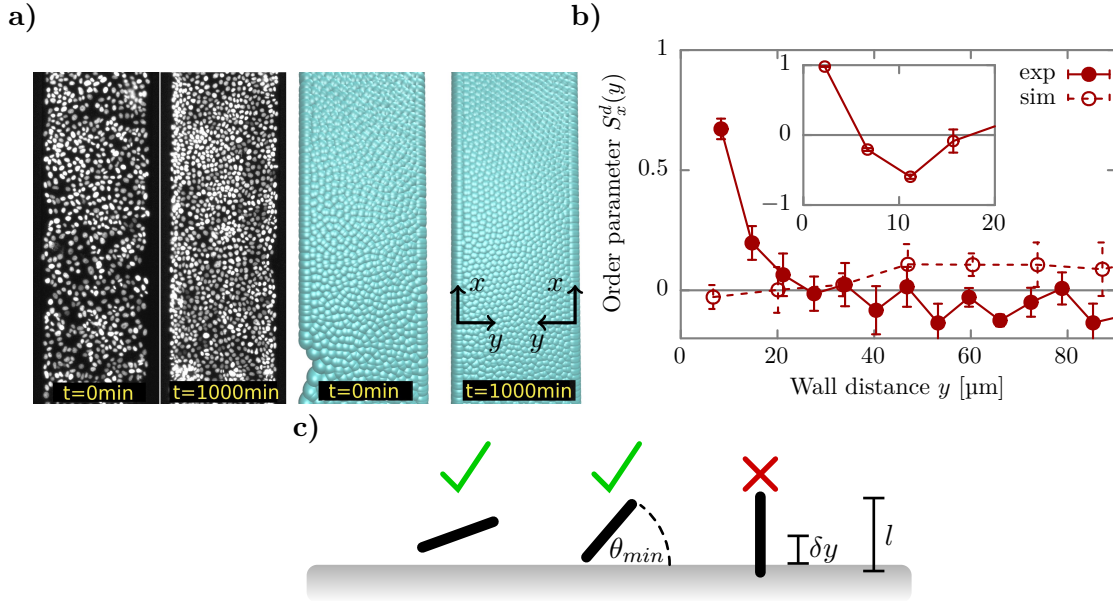


Figure 3.28: The order of cell division axes in resting cell sheets. **a)** Snapshots of resting cell sheets at early and late times in experiments (left) and simulations (right). Cells were initially seeded uniformly with a density of $2.6 \cdot 10^{-3} \mu\text{m}^{-2}$ at $t = 0 \text{ min}$ and reach a density of $4.4 \cdot 10^{-3} \mu\text{m}^{-2}$ at $t = 1000 \text{ min}$ in both cases. The channel width is $300 \mu\text{m}$ in case of the experiments and $270 \mu\text{m}$ in case of the simulations. **b)** Order parameter S_x^d as a function of the distance from the wall. Inset shows simulation data directly at the wall with a finer binning. **c)** Three cell division axes with length l at the same distance δy from the wall but with different angles θ . Redrawn from [Marel et al., 2014].

We introduced an offset y_0 , which accounts for the minimal distance between the center of the cell nucleus of a daughter cell and the actual wall. The order parameter at a distance δy can then be calculated as follows

$$S_x^d(\delta y) = 2\langle \cos^2 \theta \rangle - 1 \quad (3.71)$$

$$= 2 \int_0^{\pi/2} p(\theta) \cos^2 \theta d\theta - 1 \quad (3.72)$$

$$= \frac{\theta_{min}}{\pi} + \frac{\theta_{min}}{\pi} \cos \theta_{min} + \left(1 - \frac{2\theta_{min}}{\pi}\right) \cos^2 \theta_{min} \quad (3.73)$$

Starting from a uniform division angle distribution $p(\theta) = 2/\pi$, we assume that all cell divisions with $\theta > \theta_{min}$ for a given δy are rotated to θ_{min} , which results in the following

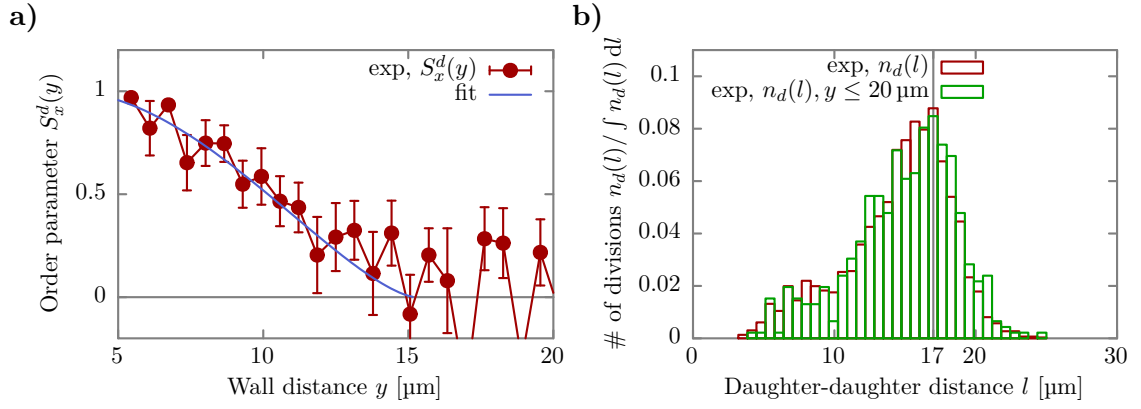


Figure 3.29: The wall-induced order of cell division axes and the daughter-daughter distance in resting cell sheets. **a)** Order parameter S_x^d as a function of the distance to the wall in a small interval of roughly 1 cell length. Solid line represents fit of equation (3.73). Error bars correspond to SEM. **b)** Distribution of daughter-daughter distances l for all divisions (red) and those closer than $20 \mu\text{m}$ to the wall (green). Both distributions peak around $\bar{l} \approx 17 \mu\text{m}$ (dashed line).

distribution:

$$p(\theta) = \begin{cases} \frac{2}{\pi} & \text{for } 0 \leq \theta < \theta_{min} \\ 1 - \frac{2}{\pi} & \text{for } \theta = \theta_{min} \\ 0 & \text{else} \end{cases} \quad (3.74)$$

A fit of equation (3.73) to the experimental data (see figure 3.29a) yields a good agreement with $y_0 = (3.1 \pm 0.9) \mu\text{m}$ and $l = (24 \pm 3) \mu\text{m}$. The daughter-daughter distance distribution (see figure 3.29b) peaks around $\bar{l} \approx 17 \mu\text{m}$, which coincides well with the former fit as $l - 2y_0 = 24 \mu\text{m} - 2 \cdot 3 \mu\text{m} = 18 \mu\text{m} \approx \bar{l}$.

Using equation (3.73), one can also calculate the average order $\langle S_x^d \rangle$ as a function of the

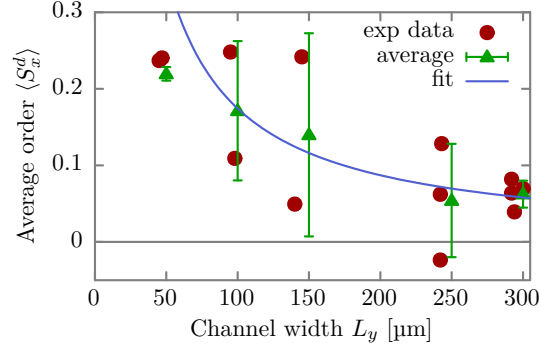


Figure 3.30: The average order $\langle S_x^d \rangle$ as a function of the channel width L_y . The green triangles are averages plus/minus SD of individual channels with roughly the same width. Solid blue line represents a fit of a/L_y for $L_y > 50 \mu\text{m}$.

channel width L_y

$$\langle S_x^d \rangle(L_y) = \frac{1}{L_y} \int_0^{L_y} S_x^d(y) dy \quad (3.75)$$

$$= \frac{2}{L_y} \int_0^{l/2+y_0} S_x^d(y) dy \quad (3.76)$$

$$= \frac{\text{const}}{L_y}. \quad (3.77)$$

Although the constant prefactor varies a lot between different experiments, the average for channels of the same size shows the expected $1/L_y$ behavior in accordance with the previous considerations (see figure 3.30). It is important to note that the above derivation is only valid for $L_y \geq l + 2y_0$, which is not true for the channel size of $50 \mu\text{m}$. Otherwise, the data seems to agree nicely with the expected behavior, i.e. $L_y \langle S_x^d \rangle$ is roughly constant for all channels $L_y > 50 \mu\text{m}$.

This wall induced order, however, is not seen to such extent in the simulations. While directly at the wall the divisions are highly aligned (see figure 3.28 inset), a layer of perpendicular cell divisions right next to it is observed. We suspect that this is an artifact caused by the highly simplified representation of cells as two point particles. In the bulk, however, cell divisions are roughly isotropic on average in accordance with the experimental

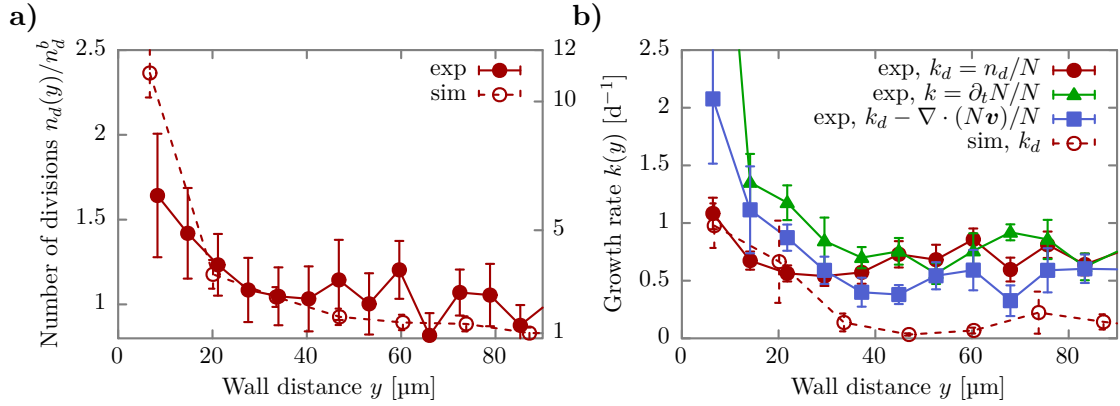


Figure 3.31: Number of divisions and division rate as a function of wall distance. **a)** Number of divisions n_d normalized by the constant number of divisions in bulk n_d^b as a function of the distance to the wall y . Experimental data is scaled according to the left axis, while simulation data is scaled according to the right axis. Note the difference in scales of at least a factor of 5. **b)** Division and growth rate k as a function of the distance to the wall y . See text for the explanation of the different curves. Error bars represent SEM.

results.

Cell division rate

More interestingly, the experimental data as well as the simulation data shows a significant increase in the number of divisions n_d near the wall (see figure 3.31a). In the experiments, the number increases by roughly a factor of 1.5, while the simulations demonstrate at least a tenfold increase. Looking instead at the division rate $k_d = n_d/N$, defined as the number of divisions n_d over the number of cells N , the experimental data still shows a peak at the wall (see figure 3.31b, red curve). In the absence of net flow, the division rate should equal the growth rate k , which we define as $k = \partial_t N/N$ the change in the number of cells $\partial_t N$ over the total number of cells N (figure 3.31b, green curve). Although displaying roughly the same constant behavior in the bulk, there is a strong deviation directly at the wall, where the change in cell number cannot stem from the number of divisions only. Considering the full continuity equation for this system (equation (2.34)), the difference in k and k_d should be compensated by the divergence of the flow. Indeed, if we subtract $\nabla \cdot (N\mathbf{v})/N$ from k_d , the resulting profile does agree better with k .

The simulations show a similar increase in division rate towards the wall. However,

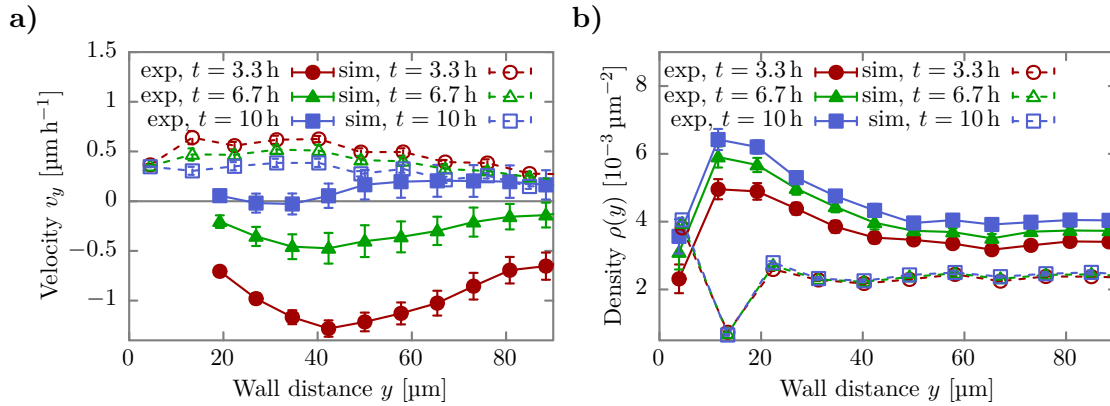


Figure 3.32: Flow and density profile as a function of wall distance at different times. **a)** Average velocity v_y perpendicular to the channel wall as a function of the wall distance y at different times t . **b)** Average density ρ as a function of the wall distance y at different times t .

no significant flow contribution can be observed as in the experiments. Although not necessarily true for the experiments, in the simulations, we can conclude that from a mechanics point of view division near the wall or, more general, near non sticky interfaces is favored (see section 1.4.2).

Flow profiles

As already mentioned, we discovered a non negligible flow of cells in the experiments. The averaged velocity profiles at different times t clearly show a consistently negative velocity, pointing towards the wall as depicted in figure 3.32a. Even more, we see a gradient in v_y , further enhancing this effect. Over time, the velocity profile as well as the gradient diminishes.

Our simulation model as it is can not reproduce the observed flow and velocity profiles but instead shows a slight gradient driving cells from the wall to the middle of the channel (see figure 3.32a).

Cell density

To follow up on the possibility of a density gradient causing the net flow of cells towards the walls, we looked at the averaged density profiles at different times t (see figure 3.32b). The experiments clearly display a density gradient. However, it would drive a flow of

cells from the walls towards the middle and not vice versa. The density towards the walls grows roughly by a factor of 1.5. In contrast to the velocity profile, the peak does not vanish for later times. Thus, some mechanism has to be at work that leads to an active migration of cells towards the walls. One possible explanation of this phenomenon could be that cells in the vicinity of a border receive signals from the cells directly at the border and align their motility direction accordingly. There is also another purely physical mechanism at work here that could contribute to the observed behavior. It has been shown recently that simple self-propelled spheres accumulate near walls due to the competition between propulsion and rotational diffusion [Elgeti & Gompper, 2013]. Although, in the experimental system the role of crowding is not clear, the effect is general to all systems with self-propelled particles.

The density profile in the simulations looks roughly flat. Near the walls, however, a layering effect is observed that indicates, where the model could need extension.

3.3.4 Invading cell sheets

Now that we characterized how the boundaries affect cell division orientation, we want to study invading cell sheets.

Divisional order

We calculated the orientation of cell divisions from the experimental data and analyzed its correlation with the direction of migration, the x -axis. The experiments show a roughly constant order of 0.3 in the bulk that drops to -0.3 towards the front (see figure 3.33a). Interestingly, there seems to be an overall perpendicular alignment of divisions directly at the front, which could stem from a surface tension. If we discard the division events near the wall in our simulations, we can reproduce most of the observed profile. Directly at the front, though, we see no preferred alignment perpendicular to the migration direction.

We also looked at the alignment of the eigenvector $\boldsymbol{\lambda}$ of the greatest eigenvalue λ_1 of the velocity gradient tensor $E_{\alpha\beta}$ with the migration direction at the sites of division and as an overall average (see figure 3.33b). Experiments and simulations both display no preferred direction of $\boldsymbol{\lambda}$ in the bulk but differ directly at the front. Note, however, that the first point of the experimental data has to be taken with care as the PIV analysis is less accurate near boundaries.

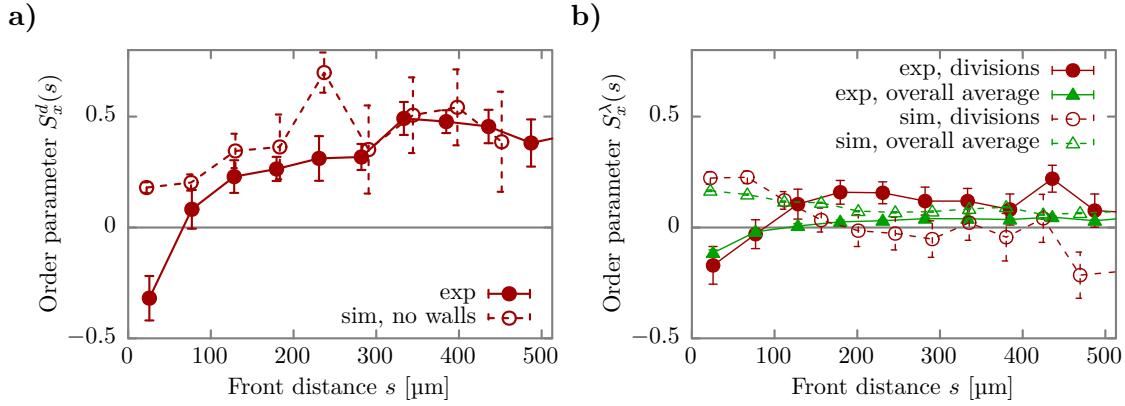


Figure 3.33: The order of the division axis and the order of the main axis of the velocity gradient tensor in invading cell sheets. a) Orientation of division axis with respect to the x -axis S_x^d as a function of the front distance s . “sim, no walls” displays the order in the simulations if particles closer than $42 \mu\text{m}$ to the walls are excluded from the evaluation. b) Orientation of the eigenvector λ of the greatest eigenvalue of the velocity gradient tensor S_x^λ with respect to the x axis as a function of the front distance s at division sites and as an average over all positions. Taken from [Marel et al., 2014].

Cell division rate

Similar to the case of the resting cell sheets, an increase in divisions can be seen at the front of invading cell sheets (see figure 3.34). Although not very pronounced, the experimental data shows a distinct peak in division rate directly at the front, while being roughly constant in the bulk. The simulations display a similar effect but much stronger.

Flow profiles

The experimental flow profiles in x and y direction as a function of the front distance s agree well with the simulations (see figure 3.35b). Both show a maximum velocity v_x at the front and a decrease towards the bulk due to growth. In the simulations, however, the velocity v_x drops much slower. Note that PIV is less accurate near interfaces, which could account for the velocity maximum being not exactly at the leading edge.

During migration, a velocity profile across the channel $v_x(y)$ emerges in the experiments that is neither parabolic, nor a simple plug flow (see figure 3.35c). Instead, it is roughly constant beyond $40 \mu\text{m}$ from the channel wall and drops to approximately $1/3$ of its bulk value directly at the channel wall. Note the overall decrease in velocity as the distance to

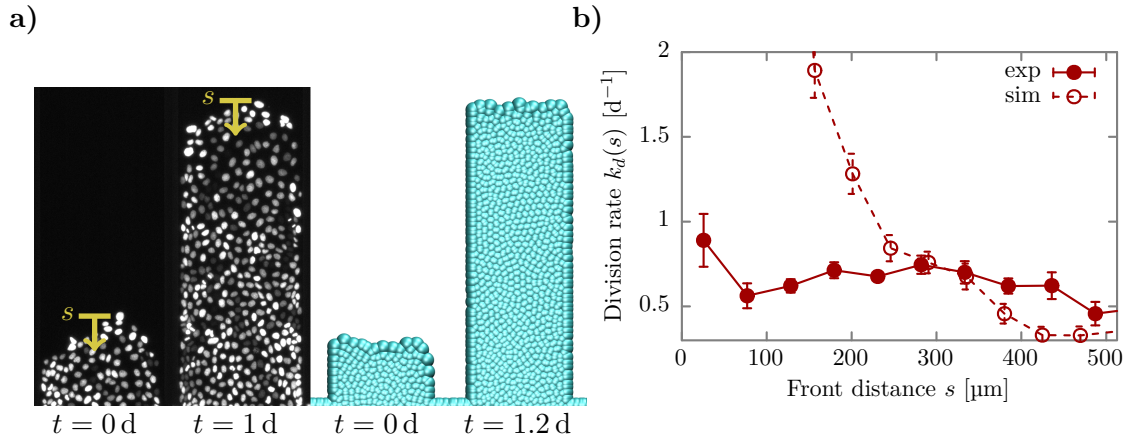


Figure 3.34: Division rate as a function of the distance to the front. a) Snapshots of invading cell sheets in experiments (left) and simulations (right) at different times t . Channels are $300 \mu\text{m}$ wide in both cases. b) Division rate k_d as a function of the distance to the front s .

the front increases, in full agreement with the aforementioned $v_x(s)$ profile. The simulations show a perfect plug flow as would be expected from the employed RBCs. Introducing another model parameter into the simulations, namely the slip length, we are able to reproduce the experimentally observed velocity profile. However, this does not change any other result qualitatively, which is why we decided to keep the RBCs for simplicity. Here, the overall velocity also decreases with the distance to the front.

In the experiments, we observe a flow gradient in y direction that reduces with the distance to the front s and drives a flow of cells from the center towards the channel walls (see figure 3.35d). This counterintuitive behavior is similar to the case of resting cell sheets. Contrary, the simulations show a flow gradient in opposite direction, driving a flow of cells from the walls towards the center of the channel. Similar to the experiments, this gradient also diminishes with the distance to the front.

Cell density

The density ρ in experiments as well as simulations display a monotonical increase with the distance to the front s . This increase is largest near the leading edge (see figure 3.36a). Again, looking at the experimental density profile in y direction for different s (see figure 3.36b), reveals the same density gradient already observed in the resting cell sheets.

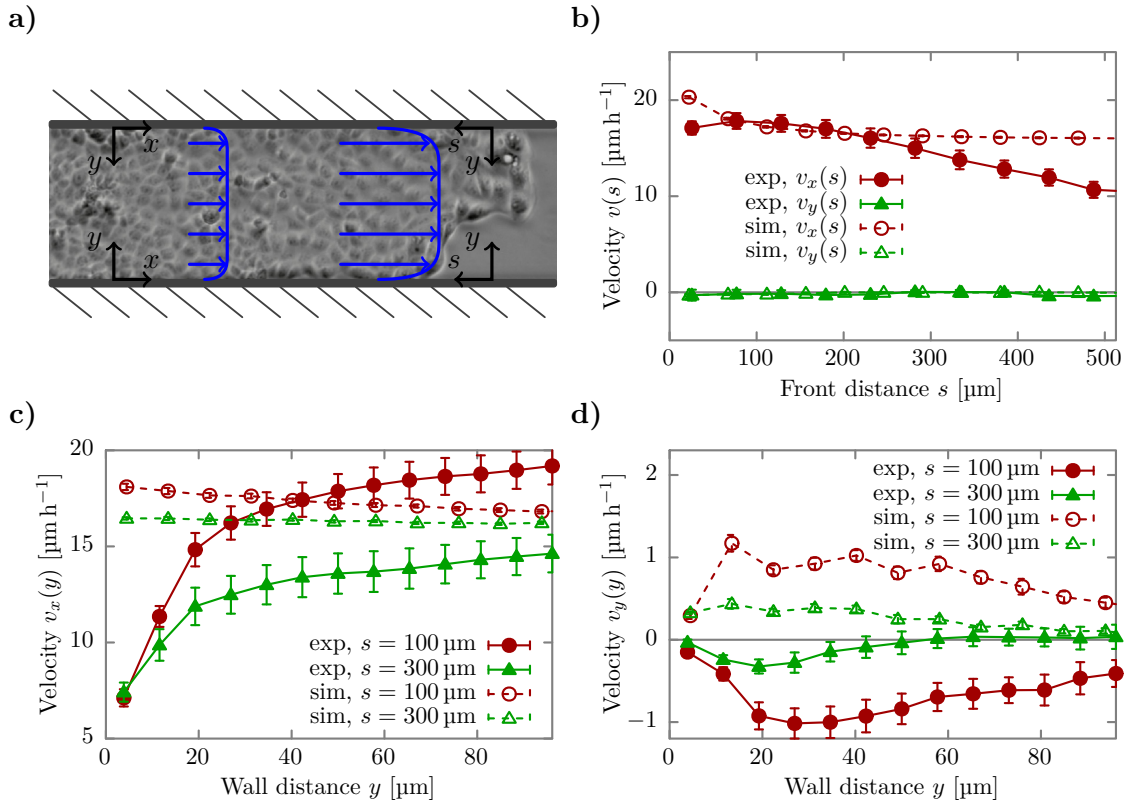


Figure 3.35: Velocity profiles perpendicular and parallel to the main migration direction. **a)** Sketch of the velocity profiles at different distances to the front for an invading cell sheet. **b)** Velocity $v_{x/y}$ as a function of front distance s . **c)** Velocity v_x in x direction as a function of wall distance y for different distances s to the leading edge. **d)** Same as in **c)** but velocity component in y direction v_y . All error bars represent SEM. Taken from [Marel et al., 2014].

The accumulation of cells near the wall grows with the distance to the leading edge. This phenomenon is not reproduced by the simulations as already mentioned earlier.

3.3.5 Cell division orientation dependence on local properties

So far, we only considered the order of the cell division axis \mathbf{d} with respect to global properties, like the main migration direction \mathbf{x} or the distance to the front s . There is, however, no known mechanism that would enable cells to sense these global properties. Therefore, we want to explore the correlations of \mathbf{d} with *local* properties.

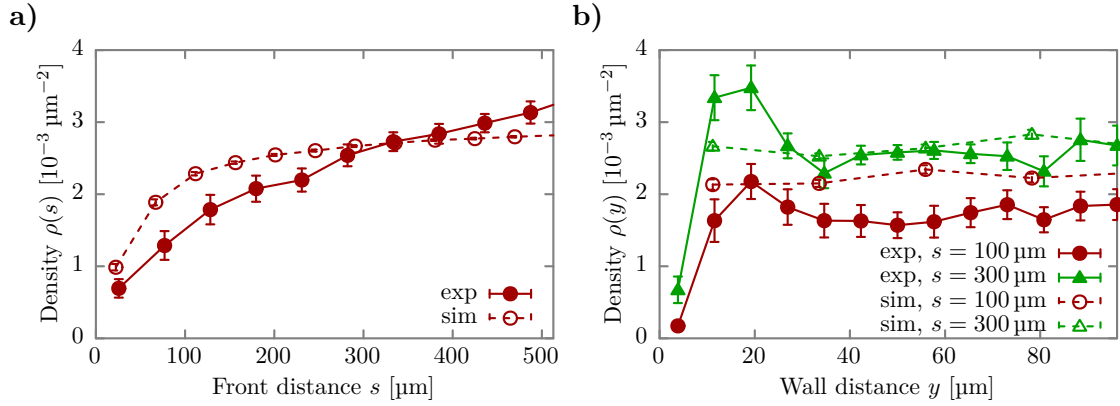


Figure 3.36: Density profiles perpendicular and parallel to the main migration direction. a) Density ρ as a function of the front distance s . b) Density ρ as a function of the wall distance y for different distances s to the leading edge. All error bars represent SEM. Taken from [Marel et al., 2014].

Dependence on velocity gradient

Expanding cell sheets of motile cells are known to be under tension [Serra-Picamal et al., 2012, Tambe et al., 2011, Trepap et al., 2009]. Hence, the question arises, whether this local tension directs cell division. Since we do not have access to the mechanical stresses in the experiments, we cannot directly address this question. However, we already noted in section 2.2.6 how the velocity field relates to the stress in Newtonian fluids and in most complex fluids as well. Thus, we calculated the strain rate tensor $E_{\alpha\beta}$ from the velocity fields. Its diagonalization yields the two eigenvalues $\lambda_{1/2}$, where $\lambda_1 \geq \lambda_2$ by convention, and the eigenvector $\boldsymbol{\lambda}$ corresponding to the larger eigenvalue λ_1 and $\bar{\boldsymbol{\lambda}}$ corresponding to the smaller eigenvalue λ_2 . We assume $\boldsymbol{\lambda}$ to be also the main axis of stress. Furthermore, we calculated the dipole strength $p = \lambda_1 - \lambda_2$ of the flow field. A value close to zero is indicative of an isotropic stress state, where the stress along both axes are equal in strength, while $p > 0$ resembles the situation of a force dipole.

The order parameter $S_{\boldsymbol{\lambda}}^d$ between the division axis \boldsymbol{d} and the main axis of the diagonalized strain rate tensor $\boldsymbol{\lambda}$ increases linearly with the dipole strength p for migrating as well as resting cell sheets in the experiments (shown in figure 3.37a). Although both display considerable order for large p of 0.5 and 0.3, respectively, the slope is smaller in the case of the confluent plated cells.

The simulations show an even higher order of up to 0.8 for invading as well as resting

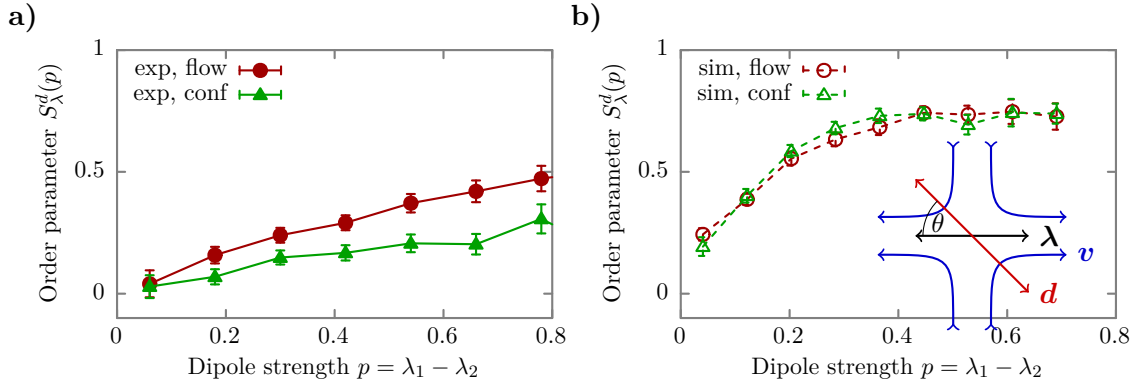


Figure 3.37: Dependence of the division orientation on the dipole strength. **a)** Order parameter S_{λ}^d of the division axis d and the main axis λ of the strain rate tensor as a function of the dipole strength p for invading (flow) and resting (conf) cell sheets in experiments. Small values characterize isotropic stress along both main axes, while large p correspond to an asymmetric stress state. **b)** Same as in **a)** for the simulations. The inset shows a sketch of the division axis d and the main axis of the strain rate tensor λ for the drawn velocity field v . All error bars represent SEM. Taken from [Marel et al., 2014].

cell sheets (see figure 3.37b). Thus, the slope is much steeper and the initial linear regime quickly saturates for larger p . Since our simulations use a mechanistic model, cells will on average always expand in the direction of least resistance, which means in the direction of the least compression or highest tension.

The unisotropic cell growth along a specific axis d creates an elongational flow field. This flow field is characterized by the difference in velocity gradients parallel ($\partial_{\parallel}v_{\parallel}$) and perpendicular ($\partial_{\perp}v_{\perp}$) to the division axis d . On average, we find $\langle \partial_{\parallel}v_{\parallel} - \partial_{\perp}v_{\perp} \rangle = (0.15 \pm 0.03) \text{ h}^{-1}$ for the invading cell sheets and $\langle \partial_{\parallel}v_{\parallel} - \partial_{\perp}v_{\perp} \rangle = (0.07 \pm 0.02) \text{ h}^{-1}$ for the confluent plated cells in the experiments (errors are SEM). The simulation results match even quantitatively. Invasion shows $\langle \partial_{\parallel}v_{\parallel} - \partial_{\perp}v_{\perp} \rangle = (0.17 \pm 0.05) \text{ h}^{-1}$ and resting cell sheets have $\langle \partial_{\parallel}v_{\parallel} - \partial_{\perp}v_{\perp} \rangle = (0.07 \pm 0.02) \text{ h}^{-1}$.

Dependence on local velocity

Due to the friction with the underlying substrate, Galilean invariance is broken. This can, in principle, lead to an alignment of the cells by the local velocity. However, while the division axis alignment S_x^d increases with the distance to the front (see figure 3.33a), the velocity decreases (see figure 3.35b), contradicting the assumption that velocity instead of

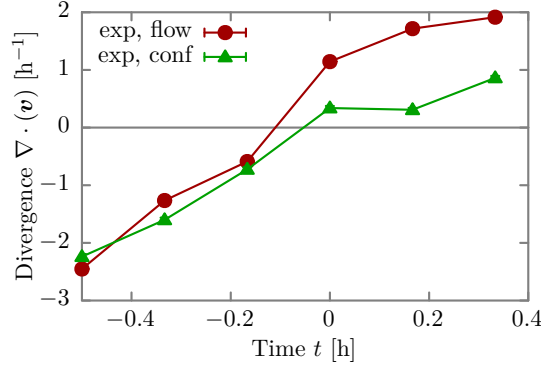


Figure 3.38: The time evolution of the divergence of the velocity field at division sites. $t = 0$ corresponds to the first frame, where both daughter cells were observed.

velocity gradients guide cell division. Indeed, the overall average order between the local velocity \mathbf{v} and the division axis \mathbf{d} (0.17 ± 0.02 for the flow experiments and 0.1 ± 0.02 for the confluent experiments) is much smaller than the average order between $\boldsymbol{\lambda}$ and \mathbf{d} (0.28 ± 0.02 and 0.15 ± 0.01 , respectively). However, fluctuations are high with standard deviations of typically 0.7.

Divergence of velocity field

The growth of the cells should be reflected in the overall divergence of the velocity field. However, looking at the time evolution of the divergence at division sites shows a negative divergence before and a positive divergence after the cell division (see figure 3.38). It is consistent with cells rounding up shortly before division and successively respreading into the tissue [Lundgren & Roos, 1976, Porter et al., 1973, Sanger, 1980]. This, on the other hand, indicates that the measured flow fields at division sites are strongly influenced by the cell round-up process.

3.3.6 Stress measurements in simulations

Although not experimentally available, we are able to determine the stress in our simulations. Surprisingly, the tissue in the simulations are not under tension in the current set-up as we expected but under pressure (see figure 3.39a). Note that we used the same parameter set that leads to a global state of tension for simulations of unconfined tissues.

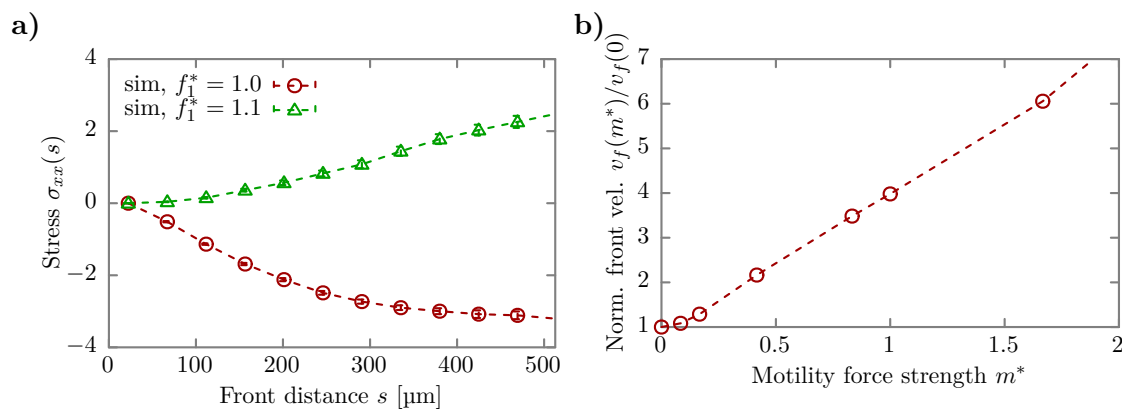


Figure 3.39: Stress as a function of the distance to the front and front velocity as a function of motility force in advancing cell sheets. **a)** Stress σ_{xx} as a function of front distance s . Note that the stress is in simulation units. As per definition, negative values correspond to pressure and positive to tension. **b)** Front velocity v_f as a function of the motility force strength $m^* = |\mathbf{F}^{m^*}|$, normalized by the front velocity at $m^* = 0$ (i.e. a tissue that expands exclusively due to cell division). All error bars represent SEM.

3.3.7 Parameter variation

In order to remedy the observed discrepancies between simulations and experiments we varied the adhesion strength f_1^* , the growth force B^* , the volume exclusion prefactor f_0^* , and the intra- and intercell friction coefficients $\gamma_{c/t}$. While a tensional state can be established in our set-up by a slight increase in adhesion strength f_1^* (see figure 3.39a), the increased adhesion leads to a partial collapse of the tissue (similar to what is mentioned in [Pathmanathan et al., 2009]), where cell-cell interactions are extended to include next-nearest neighbors. This results in a strong suppression of proliferation in the bulk of the tissue, making the analysis of cell division orientation difficult. One could argue that migration in our simulations with the standard parameters in the used set-up is caused exclusively by the pressure build-up due to growth instead of a collective motility alignment phenomenon. Nevertheless, the front velocity v_f significantly increases with the motility force strength m^* (for the standard parameters by a factor of 4) as shown in figure 3.39b. This emphasizes the importance of the motility in the simulations of expanding tissues.

As for the discrepancies at the boundaries, a thorough parameter search inside the model, varying f_1^* , f_0^* , B^* , γ_c , and γ_t has been conducted. However, we did not find a parameter set that captures all the missing aspects. Furthermore, the results remained qualitatively

the same, which is why we compared the experiments to the already established parameter set, defined in [\[Basan et al., 2013\]](#).

4 Conclusions

4.1 Negative homeostatic pressure

We have used 3d simulations to study tissue growth with and without external mechanical stresses. In particular, we were interested in growth with a negative homeostatic pressure and its dependence on different model parameters such as the growth force strength, adhesion strength, apoptosis rate and compressibility. We have shown that growth with a negative homeostatic pressure is self-sustaining. It leads to a steady state under tension, where the on average apoptotic core is balanced by a constant influx of cells from the proliferating surface. We used the experimental data of several different cell lines to show that their homeostatic pressure is likely to be negative. A simple linear extrapolation of the bulk growth rate to zero led to an estimated homeostatic pressure of the order of minus a few kilo pascal. This, however, has to be taken with care as the experimental data of the cell line CT26 clearly deviates from a linear behavior.

We measured the bulk growth rates for many different imposed stresses (compressional as well as tensional) in our simulations and discovered a general three-regime picture by looking at the bulk growth rate as a function of the difference between the imposed and the homeostatic pressure. Around the homeostatic pressure, a linear region is found that, in principle, validates the linear expansion. However, this domain does not necessarily extend into the compressional regime for negative homeostatic pressures. For high compression the bulk growth rate asymptotically approaches the stress independent apoptosis rate, while for high tension another linear regime is seen with a different slope than before. We then fitted the simulation data to the data of CT26 by varying the growth force B^* and adhesion strength f_1^* . This resulted in a valley of optimal combinations of B^* and f_1^* , which, however, all led to roughly the same homeostatic pressure of -1 to -2 kPa. Even more, the chosen optimal set of parameters was able to predict the bulk growth rates at elevated pressure of three of the remaining four cell lines by simply rescaling the simulations according to the bulk growth rate at zero pressure. Thus, the rescaling of the

experimental data with the bulk growth rate at zero pressure led to a collapse of four out of five curves, suggesting a certain universality.

Furthermore, we measured in the simulations the dependence of the homeostatic pressure on the growth force, adhesion strength, apoptosis rate and compressibility. We found that the homeostatic pressure grows with increasing growth forces, increasing compressibility and decreasing adhesion strength. It is well known that as cancer evolves, the expression of the cell-cell adhesion protein E-cadherin is lowered in the tumor cells [Weinberg, 2007]. We have shown that a reduction in adhesion leads to a higher homeostatic pressure, which would be favorable for the progression of a tumor. In addition, the observed increase in homeostatic pressure for higher compressibilities may explain, why many cancer cells across very different origins have been found to be softer (in suspension) [Cross et al., 2007, Fritsch et al., 2010, Guck et al., 2005, Jonas et al., 2011, Lekka et al., 1999, Remmerbach et al., 2009, Runge et al., 2014]. We noticed only a surprisingly small change of around 20 % of the homeostatic pressure for apoptosis rates spanning nearly two orders of magnitude.

Furthermore, the negative homeostatic pressure offers a novel and simple explanation of how tensile homeostasis is maintained. It has been shown that many epithelia are under tension in vivo [Butcher et al., 2009, Heisenberg & Bellaïche, 2013, Martin & Goldstein, 2014, Trepats et al., 2009, Wozniak & Chen, 2009]. After inflicting a model wound by laser ablation, these tissues display recoil velocities, clearly proving the state of tension. Intuitively one could think a tensile homeostasis is unstable. A simple cut relaxes stress, which elevates the pressure and, thus, apoptosis is favored. However, this results in a free surface at which cell division is increased, stabilizing the tensile state. In the simulations, we performed a virtual laser cut in 3d and the aforementioned behavior is observed. It is important to note that the increased cell division at the free surface created by the laser cut is an automatic result of the simulations and has not been incorporated into the model explicitly.

Still, the question remains to what could be the evolutionary advantage of a tensile homeostatic state. The balance of surface growth and bulk death naturally leads to a finite size. This mechanism could, thus, be used for size control. Furthermore, from a mechanics point of view, a tensile tissue connected to a stiff skeleton seems more capable of sustaining its shape and integrity under constantly changing external forces.

In addition, we compared the steady state radii of full tissue spheroids with the results of a quasi 1d set-up. The quasi 1d set-up approximates a full tissue spheroid by simulating only a small cuboidal box with high aspect ratio, where we have open boundaries along

the long axis (z) and periodic boundaries in x and y direction. A more detailed analysis revealed a tension build-up due to the periodic boundaries, which leads to increased, partially aligned cell divisions in the x - y -plane. Thus, we observed a consistently larger steady state size in the quasi 1d set-up as compared to the equivalent 3d spheroid. The stress at the boundaries is related to the homeostatic pressure, which means it is tensile for a negative homeostatic pressure. Therefore, such systems do not resemble the 1d representation of a tissue spheroid but instead describe a new state: *tensile membranes*. In this state, the tissue forms a relatively thin sheet that is maintained by the in-plane tension due to the homeostatic pressure acting across the periodic boundaries. Note, however, that tensile membranes are only possible for a negative homeostatic pressure.

It will be interesting to see, whether our extrapolation of the homeostatic pressures for the analyzed cell lines can be confirmed by direct experimental measurements and whether our predictions for the bulk growth rate behavior for tissues under tension are correct. Thus far, the simulation model has proven to reproduce the available experimental data in the context of the homeostatic pressure theory very well. It is, therefore, conceivable that it can be used to test new ideas for experiments in this context and analyze their results.

4.2 Interface dynamics of competing tissues

We investigated the interface dynamics of two competing tissues with different homeostatic pressures. In the context of the homeostatic pressure theory, this difference leads to a take-over of the tissue with the higher homeostatic pressure. First of all, we showed by analytical calculations that the dynamics in one dimension yield an interface, propagating at a constant velocity. This interface velocity depends linearly on the difference in the homeostatic pressures of the tissues.

We used the same simulation model as before confined to two dimensions and with a slightly different parameter set. In order to efficiently study tissue competitions, we proposed a new set-up called treadmilling by introducing a comoving simulation box and compared it to conventional simulations. We measured the interface position, width and stress profiles for different homeostatic stress differences, which matched perfectly the 1d analytical prediction. Also the constant front velocity was well reproduced in the simulations.

We observed that the stress is not isotropic across the interface, meaning the stress parallel does not match the stress perpendicular to the interface. This yields a surface tension per its definition. We found the surface tension to grow for increasing homeostatic stress differences.

Finally, we characterized the scaling behavior of the interface width $w = \sqrt{\langle h^2 \rangle - \langle h \rangle^2}$, where h describes the interface. For early times t , we identified a power law growth $w \sim t^\beta$, which saturates with a system size L dependent width $w_{sat} \sim L^\alpha$. We found a growth exponent $\beta \approx 0.4$ and a roughness exponent $\alpha \approx 0.25$. It was suggested by experiments that the scaling exponents of growing tissues should fall into the MBE universality class [Brú et al., 2003]. However, numerical studies could not reproduce this behavior and instead suggested the KPZ universality class. While our measured growth exponent roughly fits KPZ and MBE ($\beta_{KPZ}^{2d} = 1/3$, $\beta_{MBE}^{2d} = 3/8$), our roughness exponent is significantly smaller ($\alpha_{KPZ}^{2d} = 1/2$, $\alpha_{MBE}^{2d} = 3/2$). Experiments of growing bacterial colonies Vicsek et al. [1990] measured even another roughness exponent of $\alpha \approx 0.78$.

The question remains to what universality class the tissue competition belongs and what microscopic phenomena dominate its dynamics. It will be interesting to see whether the scaling exponents vary systematically with the homeostatic pressure difference. In a next step, the simulations could also be used to study the interface dynamics in three dimensions. This would be more closely related to actual tumor growth.

4.3 Division axes alignment in motile tissues

The emerging flow in collectively migrating cell sheets affects the orientation of the cell division axis. In the experiments, expanding MDCK cell sheets were confined in microstructured PEG-DMA channels and cell divisions, density and front position were tracked. The flow field was determined by PIV analysis. We correlated flow fields, divisional orientation and cell density to extract quantitative features of tissue migration and compared the experimental findings to those of simulations.

We observed a constant invasion speed of the cell sheets in experiments and simulations as well as a remarkable similarity in the density profile as a function of the distance to the leading edge with a roughly constant density in the bulk that drops towards the leading edge. Thus, those quantities were chosen to relate simulations and experiments. We found a strong alignment of the orientation of the cell division axis with the direction of the observed flow.

In order to differentiate phenomena caused by the cell flow from boundary effects of the channel walls, we analyzed resting cell sheets within the same PEG-DMA microchannels. Except for a small layer of roughly one to two cell diameters near the wall, division was measured to be isotropic, supporting our suggestion that the emergent flow in migrating monolayers was the main influence on the direction of cell division.

The experiments of resting cell sheets revealed another interesting and unexpected behavior. We observed an active flow of cells toward the walls, which creates and sustains a density gradient with higher densities near the wall. Over time, this flow diminishes but the density gradient remains intact. The same behavior could be verified in the experiments of invading cell sheets. However, it remains to be seen whether this is a generic feature, which is found in other tissues or experiments as well.

Analyzing local quantities showed that the orientation of the cell division axis correlates best with local flow gradients, as opposed to the channel axis or velocity direction. In fact, we found the average order between the division axis and the main axis of the strain rate tensor to be twice as large as the average order between the division axis and the local velocity direction. This is consistent with stresses orienting cell division, and the stress being proportional to the flow gradient. However, we also evaluated the velocity gradient shortly before and after cell divisions and the observed behavior shows signs of the well known round-up and respread process of dividing cells. A more rigorous analysis is needed, where individual cells are traced over time until division, to identify the dominant process.

We extended the simulations with a previously published motility algorithm and compared them to the experimental results. A striking set of features are captured well. In particular, they displayed a similar decrease in cell density towards the leading edge, comparable emergent flow profiles, a weak correlation of the main axis of the strain rate tensor with the x -axis as well as a strong correlation with the division axis and strong correlations between the main axis of the strain rate tensor and the division axis. However, comparing quantities near boundaries (channel walls or the leading edge of the invasion front) revealed strong deviations and indicate points, where the model needs to be extended. Especially the flow towards the walls and the emerging density gradient perpendicular to the channel could not be captured in the simulations. While the flow may be incorporated by some extension to the motility algorithm, we are convinced that the problems at the boundaries can only be solved by a more realistic representation of a cell to better account for its inner structure. However, it is noteworthy that the used model was not intended to study this kind of experiments. Thus, it is surprising how well the bulk phenomena are reproduced.

The orientation of cell division axes in flow fields could be of significant relevance for growing tissues in wound healing and development. It seems natural that an expanding tissue will orient individual cell divisions in the direction of expansion in order to reduce the principal stress. It remains to be seen if in-vivo experiments show similar oriented cell divisions in cellular flows.

Bibliography

- Estimated Incidence, Mortality and Prevalence Worldwide in 2012, International Agency for Research on Cancer [online]. (2014). http://globocan.iarc.fr/Pages/fact_sheets_cancer.aspx. (Cited on page 2)
- Admal, N. C. & Tadmor, E. B. (2010). A Unified Interpretation of Stress in Molecular Systems. *Journal of Elasticity*, 100(1-2), 63–143, doi:10.1007/s10659-010-9249-6. <http://link.springer.com/10.1007/s10659-010-9249-6>. (Cited on page 30)
- Alberts, B. (2008). *Molecular biology of the cell*. New York: Garland Science. (Cited on pages 5 and 20)
- Allen, M. P. (1987). *Computer simulation of liquids*. Oxford [England] : New York: Clarendon Press ; Oxford University Press. (Cited on pages 24 and 28)
- Angelini, T. E., Hannezo, E., Trepac, X., Fredberg, J. J., & Weitz, D. A. (2010). Cell Migration Driven by Cooperative Substrate Deformation Patterns. *Physical Review Letters*, 104(16), doi:10.1103/PhysRevLett.104.168104. <http://link.aps.org/doi/10.1103/PhysRevLett.104.168104>. (Cited on page 5)
- Angelini, T. E., Hannezo, E., Trepac, X., Marquez, M., Fredberg, J. J., & Weitz, D. A. (2011). Glass-like dynamics of collective cell migration. *Proceedings of the National Academy of Sciences*, 108(12), 4714–4719, doi:10.1073/pnas.1010059108. <http://www.pnas.org/cgi/doi/10.1073/pnas.1010059108>. (Cited on page 5)
- Artur, C., Adrian, N., & Victor, S. (2011). Lattice Boltzmann simulations of the time evolution of living multicellular systems. *Biorheology*, 48(3-4), 185–197, doi:10.3233/BIR-2011-0595. <http://www.medra.org/servlet/aliasResolver?alias=iospress&genre=article&iissn=0006-355X&volume=48&issue=3&spage=185>. (Cited on page 13)
- Barabási, A.-L. & Stanley, H. E. (1995). *Fractal concepts in surface growth*. New York, NY, USA: Press Syndicate of the University of Cambridge. (Cited on page 8)

- Basan, M., Elgeti, J., Hannezo, E., Rappel, W.-J., & Levine, H. (2013). Alignment of cellular motility forces with tissue flow as a mechanism for efficient wound healing. *Proceedings of the National Academy of Sciences*, 110(7), 2452–2459, doi:10.1073/pnas.1219937110. <http://www.pnas.org/cgi/doi/10.1073/pnas.1219937110>. (Cited on pages 6, 21, 22, and 100)
- Basan, M., Prost, J., Joanny, J.-F., & Elgeti, J. (2011). Dissipative particle dynamics simulations for biological tissues: rheology and competition. *Physical Biology*, 8(2), 026014, doi:10.1088/1478-3975/8/2/026014. <http://stacks.iop.org/1478-3975/8/i=2/a=026014>. (Cited on pages 15, 16, and 17)
- Basan, M., Risler, T., Joanny, J.-F., Sastre-Garau, X., & Prost, J. (2009). Homeostatic competition drives tumor growth and metastasis nucleation. *HFSP Journal*, 3(4), 265–272, doi:10.2976/1.3086732. <http://www.tandfonline.com/doi/abs/10.2976/1.3086732>. (Cited on pages 6 and 7)
- Block, M., Schöll, E., & Drasdo, D. (2007). Classifying the Expansion Kinetics and Critical Surface Dynamics of Growing Cell Populations. *Physical Review Letters*, 99(24), doi:10.1103/PhysRevLett.99.248101. <http://link.aps.org/doi/10.1103/PhysRevLett.99.248101>. (Cited on pages 9, 13, and 82)
- Bray, F., Jemal, A., Grey, N., Ferlay, J., & Forman, D. (2012). Global cancer transitions according to the Human Development Index (2008–2030): a population-based study. *The Lancet Oncology*, 13(8), 790–801, doi:10.1016/S1470-2045(12)70211-5. <http://linkinghub.elsevier.com/retrieve/pii/S1470204512702115>. (Cited on page 2)
- Brú, A., Albertos, S., Luis Subiza, J., García-Asenjo, J. L., & Brú, I. (2003). The Universal Dynamics of Tumor Growth. *Biophysical Journal*, 85(5), 2948–2961, doi:10.1016/S0006-3495(03)74715-8. <http://linkinghub.elsevier.com/retrieve/pii/S0006349503747158>. (Cited on pages 9 and 104)
- Butcher, D. T., Alliston, T., & Weaver, V. M. (2009). A tense situation: forcing tumour progression. *Nat Rev Cancer*, 9(2), 108–122, doi:10.1038/nrc2544. <http://dx.doi.org/10.1038/nrc2544>. (Cited on page 102)
- Byrne, H. & Chaplain, M. (1995). Growth of nonnecrotic tumors in the presence and absence of inhibitors. *Mathematical Biosciences*, 130(2), 151–181,

- doi:10.1016/0025-5564(94)00117-3. <http://linkinghub.elsevier.com/retrieve/pii/0025556494001173>. (Cited on page 6)
- Cross, S. E., Jin, Y.-S., Rao, J., & Gimzewski, J. K. (2007). Nanomechanical analysis of cells from cancer patients. *Nature Nanotechnology*, 2(12), 780–783, doi:10.1038/nnano.2007.388. <http://www.nature.com/doi/10.1038/nnano.2007.388>. (Cited on page 102)
- Dallon, J. C. & Othmer, H. G. (2004). How cellular movement determines the collective force generated by the Dictyostelium discoideum slug. *Journal of Theoretical Biology*, 231(2), 203–222, doi:10.1016/j.jtbi.2004.06.015. <http://linkinghub.elsevier.com/retrieve/pii/S0022519304002887>. (Cited on page 14)
- Delarue, M., et al. (2013). Mechanical Control of Cell flow in Multicellular Spheroids. *Physical Review Letters*, 110(13), doi:10.1103/PhysRevLett.110.138103. <http://link.aps.org/doi/10.1103/PhysRevLett.110.138103>. (Cited on page 11)
- Delarue, M., Montel, F., Vignjevic, D., Prost, J., Joanny, J.-F., & Cappello, G. (2014). Compressive Stress Inhibits Proliferation in Tumor Spheroids through a Volume Limitation. *Biophysical Journal*, 107(8), 1821–1828, doi:10.1016/j.bpj.2014.08.031. <http://linkinghub.elsevier.com/retrieve/pii/S0006349514009369>. (Cited on pages 11, 56, 57, and 60)
- Dembo, M. & Wang, Y.-L. (1999). Stresses at the Cell-to-Substrate Interface during Locomotion of Fibroblasts. *Biophysical Journal*, 76(4), 2307–2316, doi:10.1016/S0006-3495(99)77386-8. <http://linkinghub.elsevier.com/retrieve/pii/S0006349599773868>. (Cited on page 5)
- Drasdo, D., Kree, R., & McCaskill, J. (1995). Monte Carlo approach to tissue-cell populations. *Physical Review E*, 52(6), 6635–6657, doi:10.1103/PhysRevE.52.6635. <http://link.aps.org/doi/10.1103/PhysRevE.52.6635>. (Cited on page 13)
- du Roure, O., Saez, A., Buguin, A., Austin, R. H., Chavrier, P., Silberzan, P., & Ladoux, B. (2005). Force mapping in epithelial cell migration. *Proceedings of the National Academy of Sciences*, 102(7), 2390–2395, doi:10.1073/pnas.0408482102. <http://www.pnas.org/cgi/doi/10.1073/pnas.0408482102>. (Cited on page 5)

- Elgeti, J. & Gompper, G. (2013). Wall accumulation of self-propelled spheres. *EPL (Europhysics Letters)*, 101(4), 48003, doi:10.1209/0295-5075/101/48003. <http://iopscience.iop.org/0295-5075/101/4/48003/>. (Cited on page 92)
- Español, P. & Warren, P. (1995). Statistical Mechanics of Dissipative Particle Dynamics. *EPL (Europhysics Letters)*, 30(4), 191–196, doi:10.1209/0295-5075/30/4/001. <http://stacks.iop.org/0295-5075/30/i=4/a=001>. (Cited on page 19)
- Findlay, G. (1928). ULTRA-VIOLET LIGHT AND SKIN CANCER. *The Lancet*, 212(5491), 1070–1073, doi:10.1016/S0140-6736(00)84845-X. <http://linkinghub.elsevier.com/retrieve/pii/S014067360084845X>. (Cited on page 3)
- Fritsch, A., Höckel, M., Kiessling, T., Nnetu, K. D., Wetzels, F., Zink, M., & Käse, J. A. (2010). Are biomechanical changes necessary for tumour progression? *Nature Physics*, 6(10), 730–732, doi:10.1038/nphys1800. <http://www.nature.com/doifinder/10.1038/nphys1800>. (Cited on page 102)
- Galassi, M. (2009). *GNU Scientific Library Reference Manual*. Network Theory Ltd, 3rd ed edition. <http://www.gnu.org/software/gsl/>. (Cited on page 45)
- Galle, J., Loeffler, M., & Drasdo, D. (2005). Modeling the Effect of Deregulated Proliferation and Apoptosis on the Growth Dynamics of Epithelial Cell Populations In Vitro. *Biophysical Journal*, 88(1), 62–75, doi:10.1529/biophysj.104.041459. <http://linkinghub.elsevier.com/retrieve/pii/S0006349505730873>. (Cited on page 14)
- Gardner, M. (1970). Mathematical games: The fantastic combinations of John Conway’s new solitaire game “life”. *Scientific American*, 223(4), 120–123. (Cited on page 12)
- Gavrieli, Y. (1992). Identification of programmed cell death in situ via specific labeling of nuclear DNA fragmentation. *The Journal of Cell Biology*, 119(3), 493–501, doi:10.1083/jcb.119.3.493. <http://www.jcb.org/cgi/doi/10.1083/jcb.119.3.493>. (Cited on page 49)
- Gelbart, M. A., He, B., Martin, A. C., Thiberge, S. Y., Wieschaus, E. F., & Kaschube, M. (2012). Volume conservation principle involved in cell lengthening and nucleus movement during tissue morphogenesis. *Proceedings of the National Academy of Sciences*, 109(47), 19298–19303, doi:10.1073/pnas.1205258109. <http://www.pnas.org/cgi/doi/10.1073/pnas.1205258109>. (Cited on page 20)

- Gonzalez-Rodriguez, D., Bonnemay, L., Elgeti, J., Dufour, S., Cuvelier, D., & Brochard-Wyart, F. (2013). Detachment and fracture of cellular aggregates. *Soft Matter*, 9(7), 2282–2290, doi:10.1039/c2sm26648b. <http://xlink.rsc.org/?DOI=c2sm26648b>. (Cited on page 49)
- Gov, N. S. (2007). Collective cell migration patterns: Follow the leader. *Proceedings of the National Academy of Sciences*, 104(41), 15970–15971, doi:10.1073/pnas.0708037104. <http://www.pnas.org/content/104/41/15970.short>. (Cited on page 5)
- Guck, J., et al. (2005). Optical Deformability as an Inherent Cell Marker for Testing Malignant Transformation and Metastatic Competence. *Biophysical Journal*, 88(5), 3689–3698, doi:10.1529/biophysj.104.045476. <http://linkinghub.elsevier.com/retrieve/pii/S0006349505734172>. (Cited on page 102)
- Hannezo, E., Prost, J., & Joanny, J.-F. (2011). Instabilities of Monolayered Epithelia: Shape and Structure of Villi and Crypts. *Physical Review Letters*, 107(7), doi:10.1103/PhysRevLett.107.078104. <http://link.aps.org/doi/10.1103/PhysRevLett.107.078104>. (Cited on page 5)
- Haymanj. Secondary tumor deposits in the liver from a primary cancer of the pancreas, Wikimedia Commons [online]. (2015) [cit. 04-Jan-2015]. http://commons.wikimedia.org/wiki/File:Secondary_tumor_deposits_in_the_liver_from_a_primary_cancer_of_the_pancreas.jpg. (Cited on page 2)
- Heisenberg, C.-P. & Bellaïche, Y. (2013). Forces in Tissue Morphogenesis and Patterning. *Cell*, 153(5), 948–962, doi:10.1016/j.cell.2013.05.008. <http://linkinghub.elsevier.com/retrieve/pii/S0092867413005734>. (Cited on page 102)
- Hoehme, S., et al. (2010). Prediction and validation of cell alignment along microvessels as order principle to restore tissue architecture in liver regeneration. *Proceedings of the National Academy of Sciences*, 107(23), 10371–10376, doi:10.1073/pnas.0909374107. <http://www.pnas.org/cgi/doi/10.1073/pnas.0909374107>. (Cited on page 15)
- Hoehme, S. & Drasdo, D. (2010). A cell-based simulation software for multi-cellular systems. *Bioinformatics*, 26(20), 2641–2642, doi:10.1093/bioinformatics/btq437. <http://bioinformatics.oxfordjournals.org/cgi/doi/10.1093/bioinformatics/btq437>. (Cited on page 14)

- Hoogerbrugge, P. J. & Koelman, J. M. V. A. (1992). Simulating Microscopic Hydrodynamic Phenomena with Dissipative Particle Dynamics. *Europhysics Letters (EPL)*, 19(3), 155–160, doi:10.1209/0295-5075/19/3/001. <http://stacks.iop.org/0295-5075/19/i=3/a=001?key=crossref.197c567e055a029b59860f932faf76d1>. (Cited on page 19)
- Hurd, J. Metastasis Illustration, Wikimedia Commons [online]. (2015) [cit. 04-Jan-2015]. http://commons.wikimedia.org/wiki/File:Metastasis_illustration.jpg. (Cited on page 2)
- Ingber, D. E., Madri, J. A., & Jamieson, J. D. (1981). Role of basal lamina in neoplastic disorganization of tissue architecture. *Proceedings of the National Academy of Sciences*, 78(6), 3901–3905. <http://www.pnas.org/content/78/6/3901.abstract>. (Cited on page 3)
- Jacinto, A., Woolner, S., & Martin, P. (2002). Dynamic Analysis of Dorsal Closure in Drosophila From Genetics to Cell Biology. *Developmental Cell*, 3(1), 9–19, doi:10.1016/S1534-5807(02)00208-3. <http://linkinghub.elsevier.com/retrieve/pii/S1534580702002083>. (Cited on page 4)
- Jonas, O., Mierke, C. T., & Käs, J. A. (2011). Invasive cancer cell lines exhibit biomechanical properties that are distinct from their noninvasive counterparts. *Soft Matter*, 7(24), 11488, doi:10.1039/c1sm05532a. <http://xlink.rsc.org/?DOI=c1sm05532a>. (Cited on page 102)
- Kalluri, R. & Weinberg, R. A. (2009). The basics of epithelial-mesenchymal transition. *The Journal of Clinical Investigation*, 119(6), 1420–1428, doi:10.1172/JCI39104. <http://www.jci.org/articles/view/39104>. (Cited on page 5)
- Kennaway, E. L. & Hieger, I. (1930). CARCINOGENIC SUBSTANCES AND THEIR FLUORESCENCE SPECTRA. *British Medical Journal*, 1(3622), 1044–1046. <http://www.ncbi.nlm.nih.gov/pmc/articles/PMC2313469/>. (Cited on page 3)
- Kiehart, D. P., Galbraith, C. G., Edwards, K. A., Rickoll, W. L., & Montague, R. A. (2000). Multiple Forces Contribute to Cell Sheet Morphogenesis for Dorsal Closure in Drosophila. *The Journal of Cell Biology*, 149(2), 471–490, doi:10.1083/jcb.149.2.471. <http://jcb.rupress.org/content/149/2/471.abstract>. (Cited on page 4)

- Landau, L. D. & Lifshitz, E. M. (1986). *Theory of elasticity*. Number 7 in Course of Theoretical Physics. Oxford England Burlington, MA: Butterworth-Heinemann. (Cited on page 6)
- Landau, L. D. & Lifshitz, E. M. (1987). *Fluid mechanics*. Number 6 in Course of Theoretical Physics. Oxford, England New York: Pergamon Press, 3 edition. (Cited on pages 6 and 43)
- Lekka, M., Laidler, P., Gil, D., Lekki, J., Stachura, Z., & Hryniewicz, A. Z. (1999). Elasticity of normal and cancerous human bladder cells studied by scanning force microscopy. *European Biophysics Journal*, 28(4), 312–316, doi:10.1007/s002490050213. <http://link.springer.com/10.1007/s002490050213>. (Cited on pages 49 and 102)
- Lundgren, E. & Roos, G. (1976). Cell Surface Changes in HeLa Cells as an Indication of Cell Cycle Events. *Cancer Research*, 36(11 Part 1), 4044–4051. http://cancerres.aacrjournals.org/content/36/11_Part_1/4044.abstract. (Cited on page 98)
- Marel, A.-K., Podewitz, N., Zorn, M., Rädler, J. O., & Elgeti, J. (2014). Alignment of cell division axes in directed epithelial cell migration. *New Journal of Physics*, 16(11), 115005, doi:10.1088/1367-2630/16/11/115005. <http://iopscience.iop.org/1367-2630/16/11/115005/>. (Cited on pages 41, 83, 85, 86, 87, 93, 95, 96, and 97)
- Marel, A.-K., Rappl, S., Piera Alberola, A., & Rädler, J. O. (2013). Arraying Cell Cultures Using PEG-DMA Micromolding in Standard Culture Dishes. *Macromolecular Bioscience*, 13(5), 595–602, doi:10.1002/mabi.201200400. <http://doi.wiley.com/10.1002/mabi.201200400>. (Cited on page 83)
- Martin, A. C. & Goldstein, B. (2014). Apical constriction: themes and variations on a cellular mechanism driving morphogenesis. *Development*, 141(10), 1987–1998, doi:10.1242/dev.102228. <http://dev.biologists.org/cgi/doi/10.1242/dev.102228>. (Cited on page 102)
- Milán, M., Campuzano, S., & García-Bellido, A. (1996). Cell cycling and patterned cell proliferation in the Drosophila wing during metamorphosis. *Proceedings of the National Academy of Sciences*, 93(21), 11687–11692. <http://www.pnas.org/content/93/21/11687.abstract>. (Cited on page 4)

- Minc, N., Boudaoud, A., & Chang, F. (2009). Mechanical Forces of Fission Yeast Growth. *Current Biology*, 19(13), 1096–1101, doi:10.1016/j.cub.2009.05.031. <http://linkinghub.elsevier.com/retrieve/pii/S0960982209011324>. (Cited on page 49)
- Montel, F., et al. (2011). Stress Clamp Experiments on Multicellular Tumor Spheroids. *Physical Review Letters*, 107(18), doi:10.1103/PhysRevLett.107.188102. <http://link.aps.org/doi/10.1103/PhysRevLett.107.188102>. (Cited on pages 9, 10, 11, 17, 20, 29, 56, 57, and 60)
- Montel, F., Delarue, M., Elgeti, J., Vignjevic, D., Cappello, G., & Prost, J. (2012). Isotropic stress reduces cell proliferation in tumor spheroids. *New Journal of Physics*, 14(5), 055008, doi:10.1088/1367-2630/14/5/055008. <http://stacks.iop.org/1367-2630/14/i=5/a=055008>. (Cited on pages 17, 20, and 47)
- Muller, H. J. (1928). The Production of Mutations by X-Rays. *Proceedings of the National Academy of Sciences of the United States of America*, 14(9), 714–726. <http://www.ncbi.nlm.nih.gov/pmc/articles/PMC1085688/>. (Cited on page 3)
- Navascues, G. (1979). Liquid surfaces: theory of surface tension. *Reports on Progress in Physics*, 42(7), 1131–1186, doi:10.1088/0034-4885/42/7/002. <http://stacks.iop.org/0034-4885/42/i=7/a=002?key=crossref.a525be67a31c4c615c239d29373ef777>. (Cited on page 42)
- Nelson, C. M., Jean, R. P., Tan, J. L., Liu, W. F., Sniadecki, N. J., Spector, A. A., & Chen, C. S. (2005). Emergent patterns of growth controlled by multicellular form and mechanics. *Proceedings of the National Academy of Sciences of the United States of America*, 102(33), 11594–11599, doi:10.1073/pnas.0502575102. <http://www.pnas.org/content/102/33/11594.abstract>. (Cited on page 3)
- Nikunen, P., Karttunen, M., & Vattulainen, I. (2003). How would you integrate the equations of motion in dissipative particle dynamics simulations? *Computer Physics Communications*, 153(3), 407–423, doi:10.1016/S0010-4655(03)00202-9. <http://linkinghub.elsevier.com/retrieve/pii/S0010465503002029>. (Cited on page 23)
- Padding, J. & Louis, A. (2006). Hydrodynamic interactions and Brownian forces in colloidal suspensions: Coarse-graining over time and length scales. *Physical Review E*, 74(3),

- doi:10.1103/PhysRevE.74.031402. <http://link.aps.org/doi/10.1103/PhysRevE.74.031402>. (Cited on page 28)
- Pagonabarraga, I., Hagen, M. H. J., & Frenkel, D. (1998). Self-consistent dissipative particle dynamics algorithm. *Europhysics Letters (EPL)*, 42(4), 377–382, doi:10.1209/epl/i1998-00258-6. <http://stacks.iop.org/0295-5075/42/i=4/a=377?key=crossref.dbafd6c1471a1370f9007df9df6bcecf>. (Cited on page 23)
- Patel, A. A., Gawlinski, E. T., Lemieux, S. K., & Gatenby, R. A. (2001). A Cellular Automaton Model of Early Tumor Growth and Invasion: The Effects of Native Tissue Vascularity and Increased Anaerobic Tumor Metabolism. *Journal of Theoretical Biology*, 213(3), 315–331, doi:10.1006/jtbi.2001.2385. <http://linkinghub.elsevier.com/retrieve/pii/S0022519301923859>. (Cited on page 12)
- Pathmanathan, P., et al. (2009). A computational study of discrete mechanical tissue models. *Physical Biology*, 6(3), 036001, doi:10.1088/1478-3975/6/3/036001. <http://stacks.iop.org/1478-3975/6/i=3/a=036001?key=crossref.ace5b0ae1a7265adf0c50cbbc89f1c9a>. (Cited on pages 14 and 99)
- Peirce, S. M., Van Gieson, E. J., & Skalak, T. C. (2004). Multicellular simulation predicts microvascular patterning and in silico tissue assembly. *The FASEB Journal*, doi:10.1096/fj.03-0933fje. <http://www.fasebj.org/cgi/doi/10.1096/fj.03-0933fje>. (Cited on page 12)
- Podewitz, N., Delarue, M., & Elgeti, J. (2015). Tissue homeostasis: A tensile state. *EPL (Europhysics Letters)*, 109(5), 58005, doi:10.1209/0295-5075/109/58005. <http://iopscience.iop.org/0295-5075/109/5/58005>. (Cited on pages 47, 48, 49, 50, 52, 53, 55, 56, 59, and 60)
- Porter, K., Prescott, D., & Frye, J. (1973). CHANGES IN SURFACE MORPHOLOGY OF CHINESE HAMSTER OVARY CELLS DURING THE CELL CYCLE. *The Journal of Cell Biology*, 57(3), 815–836, doi:10.1083/jcb.57.3.815. <http://jcb.rupress.org/content/57/3/815.abstract>. (Cited on page 98)
- Poujade, M., et al. (2007). Collective migration of an epithelial monolayer in response to a model wound. *Proceedings of the National Academy of Sciences*, 104(41), 15988–15993, doi:10.1073/pnas.0705062104. <http://www.pnas.org/cgi/doi/10.1073/pnas.0705062104>. (Cited on page 5)

- Preston-Martin, S., Pike, M. C., Ross, R. K., Jones, P. A., & Henderson, B. E. (1990). Increased Cell Division as a Cause of Human Cancer. *Cancer Research*, 50(23), 7415–7421. <http://cancerres.aacrjournals.org/content/50/23/7415.abstract>. (Cited on page 3)
- Radszuweit, M., Block, M., Hengstler, J., Schöll, E., & Drasdo, D. (2009). Comparing the growth kinetics of cell populations in two and three dimensions. *Physical Review E*, 79(5), doi:10.1103/PhysRevE.79.051907. <http://link.aps.org/doi/10.1103/PhysRevE.79.051907>. (Cited on page 13)
- Ranft, J., Aliee, M., Prost, J., Jülicher, F., & Joanny, J.-F. (2014). Mechanically driven interface propagation in biological tissues. *New Journal of Physics*, 16(3), 035002, doi:10.1088/1367-2630/16/3/035002. <http://stacks.iop.org/1367-2630/16/i=3/a=035002?key=crossref.911ca10f618ca2b647a44e02e7f4515d>. (Cited on pages 8, 67, and 68)
- Ranft, J., Basan, M., Elgeti, J., Joanny, J.-F., Prost, J., & Jülicher, F. (2010). Fluidization of tissues by cell division and apoptosis. *Proceedings of the National Academy of Sciences*, 107(49), 20863–20868, doi:10.1073/pnas.1011086107. <http://www.pnas.org/cgi/doi/10.1073/pnas.1011086107>. (Cited on pages 16 and 18)
- Remmerbach, T. W., Wottawah, F., Dietrich, J., Lincoln, B., Wittekind, C., & Guck, J. (2009). Oral Cancer Diagnosis by Mechanical Phenotyping. *Cancer Research*, 69(5), 1728–1732, doi:10.1158/0008-5472.CAN-08-4073. <http://cancerres.aacrjournals.org/cgi/doi/10.1158/0008-5472.CAN-08-4073>. (Cited on page 102)
- Rous, P. (1910). A TRANSMISSIBLE AVIAN NEOPLASM. (SARCOMA OF THE COMMON FOWL.). *The Journal of Experimental Medicine*, 12(5), 696–705. <http://www.ncbi.nlm.nih.gov/pmc/articles/PMC2124810/>. (Cited on page 2)
- Rous, P. (1911). A SARCOMA OF THE FOWL TRANSMISSIBLE BY AN AGENT SEPARABLE FROM THE TUMOR CELLS. *The Journal of Experimental Medicine*, 13(4), 397–411. <http://www.ncbi.nlm.nih.gov/pmc/articles/PMC2124874/>. (Cited on page 2)
- Runge, J., Reichert, T., Fritsch, A., Käs, J., Bertolini, J., & Remmerbach, T. (2014). Evaluation of single-cell biomechanics as potential marker for oral squamous cell

- carcinomas: a pilot study. *Oral Diseases*, 20(3), e120–e127, doi:10.1111/odi.12171. <http://doi.wiley.com/10.1111/odi.12171>. (Cited on page 102)
- Sandersius, S. A. & Newman, T. J. (2008). Modeling cell rheology with the Subcellular Element Model. *Physical Biology*, 5(1), 015002, doi:10.1088/1478-3975/5/1/015002. <http://stacks.iop.org/1478-3975/5/i=1/a=015002?key=crossref.4919710ed4bec8ffc692196fa2cc8f51>. (Cited on page 14)
- Sanger, J. (1980). Surface and shape changes during cell division. *Cell and Tissue Research*, 209(2), doi:10.1007/BF00237624. <http://link.springer.com/10.1007/BF00237624>. (Cited on page 98)
- Sawyer, J. M., Harrell, J. R., Shemer, G., Sullivan-Brown, J., Roh-Johnson, M., & Goldstein, B. (2010). Apical constriction: A cell shape change that can drive morphogenesis. *Developmental Biology*, 341(1), 5–19, doi:10.1016/j.ydbio.2009.09.009. <http://linkinghub.elsevier.com/retrieve/pii/S0012160609011786>. (Cited on page 4)
- Schaller, G. & Meyer-Hermann, M. (2005). Multicellular tumor spheroid in an off-lattice Voronoi-Delaunay cell model. *Physical Review E*, 71(5), doi:10.1103/PhysRevE.71.051910. <http://link.aps.org/doi/10.1103/PhysRevE.71.051910>. (Cited on page 14)
- Serra-Picamal, X., et al. (2012). Mechanical waves during tissue expansion. *Nature Physics*, 8(8), 628–634, doi:10.1038/nphys2355. <http://www.nature.com/doi/10.1038/nphys2355>. (Cited on page 96)
- Shope, R. E. (1933). INFECTIOUS PAPILLOMATOSIS OF RABBITS: WITH A NOTE ON THE HISTOPATHOLOGY. *Journal of Experimental Medicine*, 58(5), 607–624, doi:10.1084/jem.58.5.607. <http://www.jem.org/cgi/doi/10.1084/jem.58.5.607>. (Cited on page 2)
- Shraiman, B. I. (2005). Mechanical feedback as a possible regulator of tissue growth. *Proceedings of the National Academy of Sciences of the United States of America*, 102(9), 3318–3323, doi:10.1073/pnas.0404782102. <http://www.pnas.org/content/102/9/3318.abstract>. (Cited on page 4)
- Shyer, A. E., et al. (2013). Villification: How the Gut Gets Its Villi. *Science*, 342(6155), 212–218, doi:10.1126/science.1238842. <http://www.sciencemag.org/cgi/doi/10.1126/science.1238842>. (Cited on page 5)

- Tambe, D. T., et al. (2011). Collective cell guidance by cooperative intercellular forces. *Nature Materials*, 10(6), 469–475, doi:10.1038/nmat3025. <http://www.nature.com/doifinder/10.1038/nmat3025>. (Cited on page 96)
- Thiery, J. P. (2002). Epithelial-mesenchymal transitions in tumour progression. *Nat Rev Cancer*, 2(6), 442–454, doi:10.1038/nrc822. <http://dx.doi.org/10.1038/nrc822>. (Cited on page 5)
- Trepat, X., Wasserman, M. R., Angelini, T. E., Millet, E., Weitz, D. A., Butler, J. P., & Fredberg, J. J. (2009). Physical forces during collective cell migration. *Nature Physics*, 5(6), 426–430, doi:10.1038/nphys1269. <http://www.nature.com/doifinder/10.1038/nphys1269>. (Cited on pages 5, 96, and 102)
- Tsai, D. H. (1979). The virial theorem and stress calculation in molecular dynamics. *The Journal of Chemical Physics*, 70(3), 1375, doi:10.1063/1.437577. <http://scitation.aip.org/content/aip/journal/jcp/70/3/10.1063/1.437577>. (Cited on page 30)
- Vaughan, R. B. & Trinkaus, J. P. (1966). Movements of Epithelial Cell Sheets In Vitro. *Journal of Cell Science*, 1(4), 407–413. <http://jcs.biologists.org/content/1/4/407.abstract>. (Cited on page 6)
- Verlet, L. (1967). Computer "Experiments" on Classical Fluids. I. Thermodynamical Properties of Lennard-Jones Molecules. *Physical Review*, 159(1), 98–103, doi:10.1103/PhysRev.159.98. <http://link.aps.org/doi/10.1103/PhysRev.159.98>. (Cited on page 24)
- Vicsek, T., Cserző, M., & Horváth, V. K. (1990). Self-affine growth of bacterial colonies. *Physica A: Statistical Mechanics and its Applications*, 167(2), 315–321, doi:10.1016/0378-4371(90)90116-A. <http://linkinghub.elsevier.com/retrieve/pii/037843719090116A>. (Cited on pages 9, 82, and 104)
- Vicsek, T., Czirók, A., Ben-Jacob, E., Cohen, I., & Shochet, O. (1995). Novel Type of Phase Transition in a System of Self-Driven Particles. *Physical Review Letters*, 75(6), 1226–1229, doi:10.1103/PhysRevLett.75.1226. <http://link.aps.org/doi/10.1103/PhysRevLett.75.1226>. (Cited on page 21)
- Weinberg, R. (2007). *The biology of cancer*. New York: Garland Science. (Cited on pages 3 and 102)

- Wozniak, M. A. & Chen, C. S. (2009). Mechanotransduction in development: a growing role for contractility. *Nat Rev Mol Cell Biol*, 10(1), 34–43, doi:10.1038/nrm2592. <http://dx.doi.org/10.1038/nrm2592>. (Cited on page 102)
- Yamagiwa, K. & Ichikawa, K. (1918). Experimental Study of the Pathogenesis of Carcinoma. *The Journal of Cancer Research*, 3(1), 1–29, doi:10.1158/jcr.1918.1. <http://cancerres.aacrjournals.org/content/jcanres/3/1/1.abstract>. (Cited on page 3)

List of Figures

1.1	Tumors and metastatic spreading.	2
1.2	Dorsal closure in <i>Drosophila</i>	4
1.3	Sketch of tissue growth in a confined volume.	7
1.4	Growth of tissue spheroids under pressure.	10
1.5	Sketch of the two rate growth model.	10
1.6	Conway's game of life.	12
1.7	Simulation snapshot of a growing tissue spheroid.	15
2.1	Simulation snapshots of a growing spheroid.	18
2.2	Sketch of low and high cell density in a cell sheet.	20
2.3	Sketch of the motility model.	22
2.4	Parallelization scalability.	25
2.5	Sketch of different boundary conditions used in the simulations.	27
2.6	Simulation snapshots of different methods to impose stress.	28
2.7	Fixed boundaries tissue competition simulation set-up.	33
2.8	Treadmilling simulation set-up.	34
2.9	Tissue competition.	38
2.10	Visualization of the order parameter in 2d.	41
2.11	Velocity field of steady state planar elongational flow.	44
3.1	Visualization of a negative homeostatic pressure.	48
3.2	Virtual 3d laser cut experiment.	49
3.3	Homeostatic pressure dependence on growth force and adhesion strength.	50
3.4	Homeostatic pressure dependence on different model parameters.	52
3.5	Steady state radius as a function of adhesion strength and inverse homeostatic pressure.	53
3.6	Snapshot of tissue spheroid in steady state and its radial density profile.	54

3.7	Comparison of constant pressure ensemble and gas particle method.	55
3.8	Bulk growth rate dependence on pressure for different growth forces and adhesion strengths.	56
3.9	Bulk growth rate in experiments and simulations.	57
3.10	Results of simulation data fit to the data of CT26.	59
3.11	Bulk growth rate as a function of pressure for experiments and simulations.	60
3.12	Steady state radius as a function of adhesion strength in 1d.	61
3.13	Residual bulk order.	62
3.14	Stress and residual bulk order in the quasi 1d set-up.	63
3.15	Stress and stress gradients in quasi 1d.	64
3.16	Sketch of the number fraction function φ	73
3.17	Sketch of the interface between two competing tissues A and B.	73
3.18	Comparison of treadmilling and fixed boundaries set-up.	76
3.19	Tissue characterization.	76
3.20	Interface velocity as a function of stress difference.	78
3.21	Spatial distribution of stress and stress anisotropy.	79
3.22	Comparison of 1d analytical solution and 2d simulation results.	79
3.23	Interfacial tension.	80
3.24	Interface width and saturation width as a function of time, system size and homeostatic stress difference.	81
3.25	Sketch of the experimental procedure.	83
3.26	Set-up of experiments and simulations for invading cell sheets.	85
3.27	Front velocity and density profile in experiments and simulations.	86
3.28	The order of cell division axes in resting cell sheets.	87
3.29	The wall-induced order of cell division axes and the daughter-daughter distance in resting cell sheets.	88
3.30	The average order $\langle S_x^d \rangle$ as a function of the channel width L_y	89
3.31	Number of divisions and division rate as a function of wall distance.	90
3.32	Flow and density profile as a function of wall distance at different times.	91
3.33	The order of the division axis and the order of the main axis of the velocity gradient tensor in invading cell sheets.	93
3.34	Division rate as a function of the distance to the front.	94
3.35	Velocity profiles perpendicular and parallel to the main migration direction.	95
3.36	Density profiles perpendicular and parallel to the main migration direction.	96

3.37	Dependence of the division orientation on the dipole strength.	97
3.38	The time evolution of the divergence of the velocity field at division sites.	98
3.39	Stress as a function of the distance to the front and front velocity as a function of motility force in advancing cell sheets.	99

List of Tables

2.1	Fitting results of Amdahl's law.	26
3.1	Experimental data of bulk growth rates under pressure and the linear extrapolated homeostatic pressure.	57
3.2	Time and pressure scales for simulation data rescaling.	58
3.3	Measured tissue properties.	77
3.4	Results of the scaling analysis.	82
3.5	Results of length and time scale comparison.	85
A.1	Standard parameter set for 3d simulations.	129
A.2	Standard parameter set for motility simulations.	130

Acknowledgments

First of all, I would like to thank my supervisor Dr. Jens Elgeti for the ideas behind the projects that constitute this thesis, his constant guidance, and all the valuable discussions. Furthermore, I would like to thank my doctoral advisor Prof. Dr. Gerhard Gompper for giving me the opportunity to do my Ph.D. at his institute. In addition, I would also like to thank Prof. Dr. Johannes Berg for being the second revisor of my thesis as well as Prof. Dr. Berenike Maier for chairing my defense. Moreover, I greatly acknowledge all my collaboration partners Prof. Dr. Joachim Oskar Rädler, Dr. Anna-Kristina Marel, Matthias Zorn, and Morgan Delarue, Ph.D., for the experimental data as well as fruitful discussions and many good suggestions. I am grateful to all the people of my institute, the ICS-2, but especially to our secretary Helga Paffen, the BioSoft coordinator Dr. Thorsten Auth and Elmar Westphal, who helped me at the early stages of the simulation source code development. I also appreciate to be a member of the International Helmholtz Research School of Biophysics and Soft Matter.

I have dedicated this thesis to my parents Kersten and Regina Podewitz, whom always supported and believed in me and encouraged me to follow my own path in life. Furthermore, I would like to thank my grandparents, my uncle and my aunts for their support. I am especially grateful to my big sister Maren because she has in many aspects paved the way for me and often motivated me to achieve more. In addition, I would like to thank my girl-friend Karolin Beilner for her patience and support, in particular during the last few months. In case I should have forgotten to mention someone, I hereby sincerely apologize and thank him or her as well.

Appendix

Standard parameter set in 3d simulations

Time step	Δt	10^{-3}
Pair interaction range	R_{pp}	1
Cellular expansion pressure constant	r_0	1
Range of dissipative forces	r_t	1
Distance threshold for cell division	r_{ct}	0.8
Growth force strength	B	50
Mass	m	1
Intracell friction coefficient	γ_c	100
Intercell friction coefficient	γ_t	50
Background friction	γ_{bg}	0.1
Apoptosis rate	k_a	10^{-2}
Noise intensity	$k_B T$	0.1
Repulsive cell-cell potential coefficient	f_0	2.39566
Attractive cell-cell potential coefficient	f_1	7.5
Gas particle repulsive cell-cell potential coefficient	f_0^{gas}	0.1
Verlet list cut-off radius	R_v	1.3
Isothermal compressibility	β_T	1
Relaxation time constant	t_P	1

Table A.1: Standard parameter set for 3d simulations.

Standard parameter set in motility simulations

Time step	Δt	10^{-3}
Pair interaction range	R_{pp}	1
Cellular expansion pressure constant	r_0	1
Range of dissipative forces	r_t	1
Distance threshold for cell division	r_{ct}	0.4
Growth force strength	B	5
Mass	m	1
Intracell friction coefficient	γ_c	50
Intercell friction coefficient	γ_t	50
Background friction	γ_{bg}	10
Apoptosis rate	k_a	0
Noise intensity	$k_B T$	$75 \cdot 10^{-6}$
Repulsive cell-cell potential coefficient	f_0	2.4
Attractive cell-cell potential coefficient	f_1	1.0
Verlet list cut-off radius	R_v	1.3
Rate at which cells turn motile	k_{mot}	0.4
Rate at which aligned cells turn non-motile	k^+	0.1
Rate at which unaligned cells turn non-motile	k^-	1.0
Motility force strength	m	1.2
Imposed division rate	k_{div}	0.1
Velocity relaxation time	τ_{rel}	$0.5/k_{div}$

Table A.2: Standard parameter set for motility simulations.

Erklärung der Selbstständigkeit

Ich versichere, dass ich die von mir vorgelegte Dissertation selbständig angefertigt, die benutzten Quellen und Hilfsmittel vollständig angegeben und die Stellen der Arbeit – einschließlich Tabellen, Karten und Abbildungen –, die anderen Werken im Wortlaut oder dem Sinn nach entnommen sind, in jedem Einzelfall als Entlehnung kenntlich gemacht habe; dass diese Dissertation noch keiner anderen Fakultät oder Universität zur Prüfung vorgelegen hat; dass sie – abgesehen von unten angegebenen Teilpublikationen – noch nicht veröffentlicht worden ist, sowie, dass ich eine solche Veröffentlichung vor Abschluss des Promotionsverfahrens nicht vornehmen werde. Die Bestimmungen der Promotionsordnung sind mir bekannt. Die von mir vorgelegte Dissertation ist von Prof. Dr. Gerhard Gompper betreut worden.

- [1] Marel, A.-K., Podewitz, N., Zorn, M., Rädler, J. O., & Elgeti, J. (2014). Alignment of cell division axes in directed epithelial cell migration. *New Journal of Physics*, 16(11), 115005, doi:10.1088/1367-2630/16/11/115005. <http://iopscience.iop.org/1367-2630/16/11/115005/>.
- [2] Podewitz, N., Delarue, M., & Elgeti, J. (2015). Tissue homeostasis: A tensile state. *EPL (Europhysics Letters)*, 109(5), 58005, doi:10.1209/0295-5075/109/58005. <http://iopscience.iop.org/0295-5075/109/5/58005>.

Lebenslauf

Name:	Podewitz
Vorname:	Nils
Geburtsdatum:	05.05.1985
Geburtsort:	Buchholz in der Nordheide
Staatsangehörigkeit:	deutsch
Seit April 2012	Promotionsstudent der Physik an der Universität zu Köln
Seit Januar 2012	Doktorand im Fach Physik Forschungszentrum Jülich GmbH
2005 – 2011	Studium der Physik Georg-August-Universität Göttingen
2011	Abschluss: Diplom der Physik Thema: „Forces in cellular growth and division“
1997 – 2004	Gymnasium Albert-Einstein Gymnasium, Buchholz in der Nordheide Abschluss: Abitur
1991 – 1997	Grundschule und Orientierungsstufe Jesteburg